

ND-A143 642

LARGE STRUCTURE IN THE FAR WAKES OF TWO-DIMENSIONAL  
BLUFF BODIES(U) CALIFORNIA INST OF TECH PASADENA  
GRADUATE AERONAUTICAL LABS J H CINDALA 1984

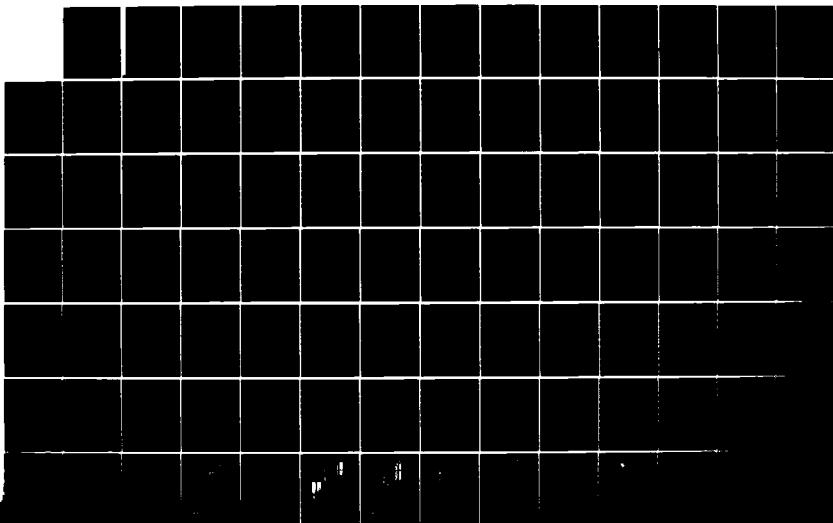
1/2

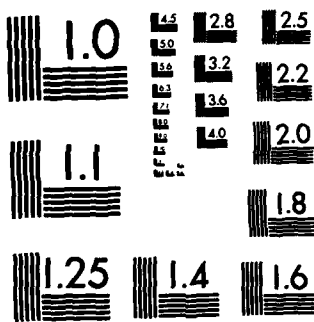
UNCLASSIFIED

NO0014-76-C-0260

F/G 20/4

NL





MICROCOPY RESOLUTION TEST CHART  
NATIONAL BUREAU OF STANDARDS-1963-A

(12)

# GRADUATE AERONAUTICAL LABORATORIES CALIFORNIA INSTITUTE OF TECHNOLOGY

AD-A143 642

Large Structure in the Far Wakes  
of Two-Dimensional Bluff Bodies

John Michael Cimbala

1984

DTIC

JUL 30 1984

Firestone Flight Sciences Laboratory

Guggenheim Aeronautical Laboratory

Karman Laboratory of Fluid Mechanics and Jet Propulsion

DTIC FILE COPY

Pasadena

84 06 22 061

**LARGE STRUCTURE IN THE FAR WAKES  
OF TWO-DIMENSIONAL BLUFF BODIES**

by  
**John Michael Cimbala**

**Report on work performed under contract No. N00014-76-C-0260  
for the  
Office of Naval Research, U. S. Navy.**

*This report was also submitted as a thesis in partial fulfillment  
of the requirements for the degree of Doctor of Philosophy*

**California Institute of Technology  
Pasadena, California**

**1984  
(submitted 27 April 1984)**

© 1984

John Michael Cimbala

All Rights Reserved



Administrative form with a grid and handwritten notes.

Administrative form with a grid and handwritten notes.
Att. on file
11

## ACKNOWLEDGMENTS

This research was conducted under the supervision of Professor Anatol Roshko whom I wish to thank for his consistent advice, guidance, and motivation. I only hope that some of his incredible knowledge of, and intuitive feel for fluid mechanics has rubbed off on me. I am also grateful to Professor Hassan Nagib of the Illinois Institute of Technology with whom I worked very closely during the initial stages of this research, and who introduced Caltech to the smoke-wire technique. His continuing enthusiasm and interest in my work since then has also been a source of inspiration. In addition, I would like to thank Professor Toshi Kubota for providing the inviscid stability calculations.

My wife Suzy truly deserves her Ph.T. degree (Putting Husband Through) for being so patient with me; the encouragement she has given me has surely been a blessing.

Many others at Caltech have helped me overcome obstacles. To each who took time out from his/her own research to spend time training and/or helping me, I extend a hearty "thank you."

Financial support for this work was provided by the Office of Naval Research, contract No. N00014-76-C-0260, for which I am very grateful. I also acknowledge the personal financial support I have received from Caltech, as well as from the A.R.C.S. Foundation and the Los Angeles Area Chamber of Commerce.

Finally, I thank Mrs. Kathy Eriksen for typing this thesis and for helping me with scheduling reminders, etc.

# ABSTRACT

Smoke-wire flow visualization and hot-wire anemometry have been used to study near and far wakes of two-dimensional bluff bodies. For the case of a circular cylinder at  $70 < Re < 2000$ , a very rapid (exponential) decay of velocity fluctuations at the Karman vortex street frequency is observed. Beyond this region of decay, larger-scale (lower wave-number) structure can be seen. In the far wake (beyond one hundred diameters) a broad band of frequencies is selectively amplified and then damped, the center of the band shifting to lower frequencies as downstream distance is increased.

The far-wake structure does not depend directly on the scale or frequency of the original Karman vortices; the growth of this structure is due to hydrodynamic instability of the developing mean wake profile; it is not caused by amalgamation of the Karman vortices. Under certain conditions amalgamation can take place, but is purely incidental, and is not the driving mechanism responsible for the growth of larger-scale structure. Similar large structure is observed downstream of porous flat plates ( $Re \approx 6000$ ), which do not initially shed Karman-type vortices into the wake.

Hot-wire measurements show that two-dimensional locally-parallel inviscid linear stability theory is adequate to explain the growth of downstream structure. Namely, measured prominent frequencies in the cylinder wake are in close agreement with those predicted by the theory, when streamwise growth of wake width is taken into account.

Finally, three-dimensionality in the far wake of a circular cylinder is briefly discussed.

## TABLE OF CONTENTS

Chapter	Title	Page
	ACKNOWLEDGMENTS	iii
	ABSTRACT	iv
	TABLE OF CONTENTS	v
	LIST OF SYMBOLS	viii
	LIST OF FIGURES	xi
1	INTRODUCTION	1
	1.1 Historical Overview	1
	1.2 Objective	7
2	EXPERIMENTAL FACILITY AND INSTRUMENTATION	8
	2.1 Facility	8
	2.2 Models	8
	2.3 Smoke-Wire Flow-Visualization Technique	9
	2.4 Instrumentation	10
3	THE ART OF FLOW VISUALIZATION	13
	3.1 Integration Effect of Streaklines	13
	3.2 Numerical Simulation of Streaklines	17
4	FLOW VISUALIZATION RESULTS	18
	4.1 Decay of the Karman Vortex Street	18
	4.2 The Secondary Vortex "Street"	19
	4.3 Porous Flat Plate Wakes	21
5	HOT-WIRE MEASUREMENTS	23



	5.1 Exponential Decay of the Karman Vortex Street	23
	5.2 Downstream Structure	25
	5.3 The Group Phenomenon	28
	5.4 Comparison With Linear Stability Theory	29
	5.5 A Look at $\gamma$ -Dependence	36
	5.6 Simultaneous Smoke-Wire and Cross-Wire Records	37
	5.7 Porous Flat Plate Wake Surveys	38
6	THREE-DIMENSIONAL EFFECTS	41
	6.1 Unforced Three-Dimensionality	41
	6.2 Forcing Attempts	44
7	DISCUSSION AND CONCLUSIONS	45
	7.1 Interpretation of Streakline Patterns	45
	7.2 Decay of the Karman Vortex Street	45
	7.3 Downstream Structure	46
	7.4 Three-Dimensionality	49
	APPENDICES	50
A	NUMERICAL STREAKLINES	50
	A.1 Procedure	50
	A.2 Viscously-Decaying Vortex Street	50
B	CROSS-WIRE WAKE SURVEYS	54
	B.1 Cross-Wire Calibration Procedure	54
	B.2 Wake Surveys	54
	B.3 Analysis of the Data	58

C	INVISCID LINEAR STABILITY CALCULATIONS	60
	REFERENCES	63
	FIGURES	68

# LIST OF SYMBOLS

Symbol	Description
$A$	amplitude of fluctuations, arbitrary scale
$A_0$	initial perturbation amplitude
$a$	wavelength of vortex street (distance between successive vortices of the same sign)
$b$	lateral separation of vortices in a vortex street
$d$	model diameter, or hot-wire diameter
$D$	mass diffusivity
$f$	passage frequency of fluctuations
$f_k$	frequency of the Karman vortex street
$f_m$	frequency with maximum growth-rate
$f_n$	neutral frequency in stability calculations
$f_p$	most prominent measured frequency
$f_1$	frequency of the Karman vortex street
$f_2$	frequency of the secondary vortex street
$g$	spatial growth rate of linear stability theory
$L$	length of cylinder or wire
$n_g$	average number of cycles within a group
$r$	distance from a vortex center
$Re$	Reynolds number, $\frac{U_\infty d}{\nu}$
$St$	Strouhal number
$t$	time
$t_t$	time threshold when searching for a group
$U$	mean velocity in $x$ -direction

$\bar{U}$	average velocity in a shear layer
$U_c$	convection velocity
$U_i$	induced velocity
$U_o$	mean centerline velocity in $x$ -direction
$U_\infty$	freestream velocity
$U^*$	normalized mean velocity, $U^* = \frac{U - U_\infty}{U_o - U_\infty}$
$u$	instantaneous velocity in $x$ -direction, $u = U + u'$
$u_t$	velocity threshold when searching for a group
$u_\theta$	circumferential velocity
$u_{-45^\circ}$	velocity normal to the $-45^\circ$ wire
$u_{+45^\circ}$	velocity normal to the $+45^\circ$ wire
$u'$	fluctuating velocity in $x$ -direction
$u'_{rms}$	rms velocity fluctuation in the $x$ -direction
$V$	mean velocity in $y$ -direction
$v$	instantaneous velocity in $y$ -direction, $v = V + v'$
$v'$	fluctuating velocity in $y$ -direction
$W_o$	normalized mean centerline velocity defect
$w$	width of a streakline
$x$	coordinate parallel to freestream and normal to model axis
$x^*$	non-dimensional downstream distance, $x^* = x/\delta(x)$
$\underline{x}$	vector position (x,y)
$y$	coordinate normal to freestream and normal to model axis
$y_o$	$y$ -location of wake centerline
$z$	coordinate normal to freestream and parallel to model axis
$\alpha$	complex wave number in stability calculations
$\beta$	normalized frequency, $\beta = \frac{2\pi f \delta}{U_\infty}$
$\beta_p$	most prominent non-dimensional frequency

$\delta$	wake half-width thickness
$\Gamma$	circulation of a vortex
$\nu$	kinematic viscosity
$\theta$	wake momentum thickness
$\theta_{SL}$	shear layer integral thickness
$\sigma$	solidity of a porous plate (% of the total area which is solid as opposed to open)
$\varphi$	y-dependent component of perturbation stream function
$\psi$	perturbation stream function

## LIST OF FIGURES

- Figure 2.1      Wind tunnel facility, side view (not to scale).
- Figure 2.2      Digital data acquisition system.
- Figure 3.1      Circular cylinder wake at  $Re = 90$ ; smoke-wire at  $x/d =$  a) 4, b) 50, c) 100, and d) 150.
- Figure 3.2      Numerical simulation of decaying Karman vortex street,  $Re = 90$ ; streaklines introduced at  $x/d =$  a) 0, and b) 100.
- Figure 4.1      Circular cylinder wake at  $Re = 130$ ; smoke-wire at  $x/d =$  a) 8, b) 150, and c) 200.
- Figure 4.2      Circular cylinder wake at  $Re = 140$ ; smoke-wire at  $x/d =$  a) 8, b) 50, c) 100, and d) 200.
- Figure 4.3      Circular cylinder wake at  $Re = 155$ ; smoke-wire at  $x/d =$  a) 8, b) 100, c) 100, and d) 200.
- Figure 4.4      Circular cylinder wake at  $Re = 190$ ; smoke-wire at  $x/d =$  a) 8, b) 100, and c) 200.
- Figure 4.5      Circular cylinder wake at  $Re = 2200$ ; smoke-wire at  $x/d =$  a) 1, and b) 160.
- Figure 4.6      Porous flat plate wake at  $Re = 6800$ ,  $\sigma = 29\%$ ; smoke-wire at  $x/d =$  a) 0, and b) 38.
- Figure 4.7      Porous flat plate wake at  $Re = 6000$ ,  $\sigma = 47\%$ ; smoke-wire at  $x/d =$  a) 0, and b) 44.

- Figure 5.1      Amplitude spectrum of  $v'/U_\infty$  at inflection points of mean velocity profile; circular cylinder wake at  $Re = 150$ ,  $x/d = 25$ .
- Figure 5.2      Exponential decay of Karman vortex street; circular cylinder wake at  $Re = 140$  and  $150$ .
- Figure 5.3      Amplitude spectra at several downstream distances; circular cylinder wake at  $Re = 150$ .
- Figure 5.4      Growth-decay cycles of selected discrete frequencies; circular cylinder wake at  $Re = 150$ .
- Figure 5.5      Amplitude spectra at several downstream distances; circular cylinder wake at  $Re = 140$ .
- Figure 5.6      Growth-decay cycles of selected discrete frequencies; circular cylinder wake at  $Re = 140$ .
- Figure 5.7a)     Amplitude spectra at several downstream distances; circular cylinder wake at  $Re = 500$ .
- Figure 5.7b)     Normalized amplitude spectra at several downstream distances; circular cylinder wake at  $Re = 500$ .
- Figure 5.7c)     Fully normalized amplitude spectra at several downstream distances; circular cylinder wake at  $Re = 500$ .
- Figure 5.8a)     Growth-decay cycles of selected discrete frequencies; circular cylinder wake at  $Re = 500$ .
- Figure 5.8b)     Normalized growth-decay cycles of selected discrete frequencies; circular cylinder wake at  $Re = 500$ .

- Figure 5.9 Time-trace of  $v'/U_\infty$ ; circular cylinder wake at  $Re = 150$ ,  $x/d = 200$ , and  $y/d = 1.5$ .
- Figure 5.10 Probability density functions of  $v'$  fluctuations; circular cylinder wake at  $Re = 150$ .
- Figure 5.11 Average number of cycles per group versus downstream distance; circular cylinder wake at  $Re = 150$ .
- Figure 5.12 Spatial inviscid stability solutions, Gaussian wake profile.
- Figure 5.13 Temporal inviscid stability solutions, Gaussian wake profile.
- Figure 5.14 Mean velocity profiles; circular cylinder wake at  $Re = 150$ .
- Figure 5.15 Wake half-width thickness versus downstream distance; circular cylinder wake at  $Re = 150$ .
- Figure 5.16 Mean centerline velocity defect versus downstream distance; circular cylinder wake at  $Re = 150$ .
- Figure 5.17 Numerical simulation of growth-decay cycles; circular cylinder wake at  $Re = 150$ .
- Figure 5.18 Peak frequency versus downstream distance; circular cylinder wake at  $Re = 150$ .
- Figure 5.19 Peak frequency versus downstream distance; circular cylinder wake at  $Re = 140$ .
- Figure 5.20 Peak frequency versus downstream distance; circular cylinder wake at  $Re = 500$ .



- Figure 5.21 Amplitude spectra at several  $y$ -locations; circular cylinder wake at  $Re = 300$ , and at  $x/d = 750$ .
- Figure 5.22 Prominent frequency versus  $y$ ; circular cylinder wake at  $Re = 300$ , and at  $x/d = 750$ .
- Figure 5.23 Sketch of frequency-sensitivity in the  $y$ -direction, probes at  $y_1$  and  $y_2$ ; a) high frequency, b) low frequency structure.
- Figure 5.24 Simultaneous smoke-wire and cross-wire records, circular cylinder wake at  $Re = 150$ ; smoke-wire at  $x/d = 275$ , cross-wire at  $x/d = 400$ ,  $y/d = -4$ .
- Figure 5.25 Mean velocity profiles for porous flat plate;  $\sigma = 47\%$ ,  $Re = 5000$ .
- Figure 5.26 Amplitude spectra at several downstream distances; porous flat plate wake ( $\sigma = 47\%$ ) at  $Re = 5000$ .
- Figure 5.27 Peak frequency vs. downstream distance; porous flat plate wake ( $\sigma = 47\%$ ) at  $Re = 5000$ .
- Figure 6.1 Edge and plan views of a circular cylinder wake at  $Re = 140$ ; smoke-wire at  $x/d = a) 8, b) 100, \text{ and } c) 200$ , and at  $y/d = 0$ .
- Figure 6.2 Plan view of a circular cylinder wake at  $Re = 155$ ; smoke-wire at  $x/d = 8, y/d = 0$ .
- Figure 6.3 Plan view of a circular cylinder wake at  $Re = 150$ ; smoke-wire at  $x/d = 100, y/d = 2$ .
- Figure 6.4 Edge and plan views of a circular cylinder wake at  $Re = 190$ ; smoke-wire at  $x/d = a) 8, b) 100, \text{ and } c) 200$ , and at  $y/d = 0$ .

- Figure B.1      Cross-wire calibration, polynomial fit to order 4.
- Figure B.2      Cross-wire velocity decomposition.
- Figure B.3      Mean velocity profiles for circular cylinder wake at  $Re = 140$ .
- Figure B.4      Mean velocity profiles for circular cylinder wake at  $Re = 150$ .
- Figure B.5      Mean velocity profiles for circular cylinder wake at  $Re = 500$ .
- Figure B.6      Time-trace of  $u'/U_\infty$ ; circular cylinder wake at  $Re = 150$ ,  $x/d = 200$ , and  $y/d = 1.5$ .
- Figure B.7      Time-trace of Reynolds stress,  $-u'v'/U_\infty$ ; circular cylinder wake at  $Re = 150$ ,  $x/d = 200$ , and  $y/d = 1.5$ .
- Figure B.8      Freestream spectra at tunnel conditions corresponding to each set of measurements.
- Figure B.9      Freestream spectra at tunnel conditions corresponding to each set of measurements.
- Figure C.1      Comparison of far-wake stability calculations with experiment;  $W_0 \approx 0.3$ .

## Chapter 1

### Introduction

#### 1.1. Historical Overview

Wakes generated by two-dimensional bluff bodies have been the focus of hundreds of experiments since the early 1900's. For a detailed review or bibliography of work on this subject, the reader is referred to Morkovin (1964) or Berger and Wille (1972). The majority of experimental efforts in the past have dealt primarily with near wakes (only a few diameters downstream). A more limited amount of work has been done on the *far* wakes of bluff bodies (up to several hundred diameters), and that is the subject on which we wish to focus here.

Let us consider the two-dimensional problem. It is well known from dimensional analysis and simple scaling laws that a plane far wake grows as  $x^{\frac{1}{2}}$ , while the velocity defect decays as  $x^{-\frac{1}{2}}$ . (See for example, Cantwell (1979)). We would expect therefore, as we go downstream in the wake, that the size of the largest-scale structure should increase, while its passage frequency should decrease. This in fact has been experimentally verified. Taneda (1959), using flow visualization in the wakes of two-dimensional cylinders and flat plates, observed a far wake structure much like the original Karman vortex street, but of larger scale. He viewed the process as one of changing hydrodynamic stability, i.e., the original street decays ("breaks down") and the wake "rearranges" itself into a new configuration appropriate to the new (downstream) position. Taneda found that for laminar wakes ( $50 < Re < 150$ ), the ratio of the secondary vortex street scale to that of the primary (Karman) street ( $a_2/a_1$ ) varies from 1.5 to 3.5; for turbulent wakes this ratio is roughly 10, and the secondary street does not

appear until much further downstream, after the wake has had time to grow significantly. He also reported that this sequence sometimes repeats itself.

Other investigators have also reported large scale organized structure in the far wakes of bluff bodies. Grant (1958) observed quasi-periodic large structures several hundred diameters downstream of his cylinder at  $Re = 1300$ , which he described as "jets of turbulent fluid proceeding outward from the central plane of the wake." Successive "jets" arise and decay, their overall size becoming larger with increasing downstream distance.

Gerrard (1968) studied the downstream development of a cylinder wake at  $Re = 113$ . At  $x/d = 450$  he found that the fundamental (Karman) frequency is lost in the background noise, but a lower-frequency fluctuation is found. The possibility of a secondary vortex street was suggested, the ratio of secondary to primary frequencies being about 0.033.

Zdravkovich (1968) studied the development of the wake behind a set of three circular cylinders in close proximity. He found that the shed vortices rapidly decay as they interact with each other. Subsequently, a new vortex street of larger scale appears downstream. Zdravkovich explained the formation of the secondary vortex street as a coupling of two mechanisms - shear layer instability, and a rolling up process induced by the distributed vorticity in the wake. Similar experiments were done more recently by Williamson (1983).

An obvious extension of Zdravkovich's work is the wake of a cluster of many cylinders - or, in the general case, the wake of a porous two-dimensional body, such as a screen or perforated flat plate aligned normal to the flow. Investigations of the latter have been reported by Castro (1971), and more recently by Valensi (1974). Castro categorized two distinct regimes of flow based on the solidity of the plate: a) For high solidity (low porosity) a Karman vortex street

dominates the near wake. b) For low solidity ( $\sigma < 0.8$ ) the plate does not shed Karman vortices, but there still is a dominant frequency present downstream, which he attributed to far wake instability. Valensi examined the latter regime in more detail with a 53% solid plate; he shows power spectra and smoke pictures. The dominant near-wake frequency corresponds to a rolling up of the shear layers on either side of the wake; further downstream (beyond five plate widths), the dominant frequency is associated with a Karman-type vortex street, which forms *after* the shear layers have merged. Smoke visualization confirms his hot-wire results.

Another interesting set of experiments was reported by Durgin and Karlsson (1971). They subjected the cylinder wake to a deceleration, thereby distorting the Karman vortex street. Their results show an annihilation of the concentrated vortices, and the subsequent creation of a new vortex street of lower frequency and longer wavelength. They, like Taneda, attributed this effect to changing hydrodynamic stability. Although the non-decelerated wake of Taneda does not experience bending and stretching of vortex filaments, as does the decelerated wake, the similarity of the two results is remarkable.

In a closely related experiment, Keffer (1965) used a constant-area distorting duct to impose a strain field upon the wake. His flow visualization results show a secondary vortex-street-like structure emerging with a frequency 0.36 times the Karman frequency at  $Re = 350$ .

Interest in Taneda's discovery has re-surfaced in the past decade. Based on an inviscid model, Weihs (1973) suggested that multiple Karman vortex street modes *are* possible. In an attempt to compare his model with experiment, he plotted Taneda's results and obtained the fit (for  $60 < Re < 120$ ):

$$\frac{a_2}{a_1} = \frac{220}{Re} \quad (1.1)$$

although there is considerable scatter in the data. Matsui and Okude (1980) made careful hot-wire measurements at Reynolds numbers between 100 and 180, of the velocity fluctuations associated with this secondary-street phenomenon. They also reported an inverse Reynolds number relation, but their constant was much different than Taneda's (Eq. 1.1):

$$\frac{a_2}{a_1} = \frac{295}{Re} \quad (1.2)$$

Thus it seems that the development of the secondary vortex street is not independent of experimental facility. (Taneda's cylinders were towed in a water channel, while Matsui and Okude used a low-speed wind tunnel).

Meanwhile Townsend (1979), using multiple hot-wire arrays, found periodic flow patterns resembling Karman vortex streets for a much higher Reynolds number ( $Re = 8000$  at  $x/d = 170$ ). "Groups" of three to five vortical structures were observed; the passage frequency within a group being uniform, but varying considerably from one group to the next. Regions of random fluctuations seem to fill the gaps between successive groups. Long-time-averaged spectra therefore do not show a peak at any particular frequency. Townsend estimated that these eddy groups contribute 15 to 20% of the total turbulent energy. Such grouping of structures had previously been suggested by Gupta et al. (1971) for the turbulent boundary layer.

Matsui and Okude (1981) later abandoned Taneda's original conjecture that the secondary street results from hydrodynamic instability, following the

"breakdown" of the primary street. In its stead they proposed that pairing is the mechanism for the change in scale. The possibility of amalgamation of smaller structures, as in mixing layers, had also been speculated by Roshko (1976). Matsui and Okude's conclusion, however, was based partly on flow visualization, where the flow tracer was introduced upstream of the cylinder. As will be pointed out in Chapter 3, this type of visualization can be very misleading. Furthermore, with a pairing mechanism the frequency of the secondary street should be half that of the primary street, but this is not the case for all Reynolds numbers. Matsui and Okude (1980) measured the frequencies of the primary and secondary streets. From their Figure 10 one can calculate the ratio of these two frequencies;  $f_2/f_1$  ranges from 0.2 to 0.52. Interestingly, at  $Re = 140$  this ratio is approximately 0.44; yet this was the Reynolds number chosen to support their pairing hypothesis (Matsui and Okude (1981)).

At about the same time, Cimbala, Nagib and Roshko (1981) reported strong experimental evidence in support of Taneda's stability hypothesis. Namely, they employed the smoke-wire flow-visualization technique of Corke, et al. (1977) and hot-wire anemometry to show that concentrated vortices of the Karman vortex street decay exponentially. As will be discussed in Chapter 3, the very rapid decay of the Karman vortex street has been known for quite some time (see for example Roshko (1953)); the full impact of this decay, however, has not been realized due to misinterpretation of streakline flow visualization. Cimbala, et al. showed that by 100 to 150 diameters downstream of a cylinder at  $Re \approx 100$ , the initial vortex street can no longer be found. Thus, they concluded that the development of any subsequent structure can *not* be directly dependent upon the original vortex street (i.e., amalgamation), but rather must be the result of a local wake instability of the developing mean velocity profile. Details of these and subsequent experiments are reported in the present paper. Recall that a similar conclusion had been reached by Durgin and Karlsson (1971) for the case

of a decelerated wake.

Matsui and Okude (1983), again studied the wake at  $Re = 140$ . Using simultaneous hot-wire anemometry and smoke visualization at  $x/d = 75$ , they show evidence that the smoke lumps are indeed vortices at this location; therefore they conclude, based on flow visualization of these lumps, that pairing is the predominant mechanism for the change of scale. The frequency ratio  $f_2/f_1$  is not always exactly one-half because not all of the vortices pair up; a few are left stranded, causing some irregularity. However, when Matsui and Okude acoustically excite the wake at  $\frac{1}{2}$  or  $\frac{1}{3}$  of the Karman frequency, they observe regular pairing or tripling, respectively.

In contrast to the conclusions of Matsui and Okude, Nagib and Desruelle (1982) and later Desruelle (1983) confirmed the findings of Cimbala, et al. (1981) with a different flow facility. In addition they used acoustic excitation to experimentally derive the stability characteristics of the wake. Namely, amplification rates are plotted as a function of disturbance frequency and of downstream location. As expected, the band of amplified frequencies shifts to lower values and broadens as downstream distance is increased.

Several theoretical and numerical investigations of this matter have also been made; for example, see Weihs (1973), Aref and Siggia (1981), Schatzman (1981), and Saffman and Schatzman (1981). For the most part these models are inviscid, two-dimensional, and assume an infinite array of vortices; only the subharmonic instability has been given much attention, although Saffman and Schatzman discuss other possibilities. Robinson (1984) has investigated three-dimensional stability of an initially two-dimensional row of staggered vortices.



## 1.2. Objective

For the case of a plane free shear layer, amalgamation of small vortices into larger ones is an important contributor to the growth of coherent structures. (See for example Brown and Roshko (1974).) To what extent amalgamation influences the scale of structure in a *wake* is of concern here. As discussed above, there is considerable disagreement among researchers as to the mechanism(s) responsible for the large-scale structure observed in far wakes of two-dimensional bluff bodies. The two views are summarized here:

a) Hydrodynamic instability of the mean wake profile is responsible for the growth of downstream structure, independent of and not directly resulting from the vortices shed from the body (Karman vortex street).

b) The large structure in the far wake is a result of amalgamation of the Karman vortices into larger vortical structures.

Our overall objective then is to describe definitively the mechanism that causes the change of scale. The experimental tools we have employed toward this end are hot-wire anemometry and smoke-wire visualization. We are primarily concerned with the two-dimensional aspect of the problem; three-dimensionality is also discussed briefly.

## Chapter 2

### Experimental Facility and Instrumentation

#### 2.1. Facility

The flow-visualization experiments, as well as the hot-wire measurements, were conducted in an open-return, low-turbulence wind tunnel, shown schematically in Figure 2.1. The test section was 0.5 m square and 2 m long; flow velocity was variable from 0.5 m/s to 12 m/s. The turbulence intensity  $u'_{rms}/U_\infty$  of the freestream was originally measured to be 0.4% at  $U_\infty = 2$  m/s. We had concluded that this turbulence level was too high for accurate wake measurements, where the fluctuations in the wake itself are quite low. Therefore we refurbished the facility with a new test-section and added several screens in the settling chamber, in the manner suggested by Loehrke and Nagib (1972). The final result in the test section is a background turbulence level of about 0.1 to 0.2% at  $U_\infty = 2$  m/s.

#### 2.2. Models

The circular cylinders used in the experiments varied in diameter from 0.08 cm to 0.5 cm, giving a Reynolds number range from 70 to over 2000 (based on cylinder diameter,  $Re = \frac{U_\infty d}{\nu}$ ). The cylinders, made of drill rod, spanned the test section and passed through the walls at either end, where they were held in tension by fasteners outside the tunnel walls. Drill rod provided the required strength, uniformity of diameter, and smoothness. Before each run, the cylinder was polished carefully to remove any dust build-up or corrosion.

Three-dimensionally perturbed cylinders were used as well as the smooth two-dimensional ones, (see Chapter 8). To make one of these three-dimensional

cylinders, paint was sprayed on the surface of the cylinder at specific intervals, and for certain lengths along its axis, after masking those sections which were to remain unpainted. In this manner, the cylinder diameter was increased where painted, producing a three-dimensional disturbance along the span.

In addition to circular cylinders, porous flat plates were also stretched across the test section, with their broad-sides facing the flow. The plates were approximately 2 cm in width and were cut from screens. (Reynolds number based on this width ranged from 3000 to 9000.) In the initial stages of this work, done in cooperation with H. Nagib, we looked at a number of porous plates of various solidities and mesh sizes. From these we picked one with initially laminar flow, and one with initially turbulent flow for our smoke-visualization experiments (see Chapter 4): a) a 29% solidity screen with wire diameter 0.18 mm and mesh size 1.15 mm, and b) a 47% solidity screen with wire diameter 0.43 mm and mesh size 1.59 mm, respectively. The screens were held in tension by fasteners which passed through the tunnel walls.

### **2.3. Smoke-Wire Flow-Visualization Technique**

A very simple technique for introducing closely spaced streaklines in wind tunnels is called "smoke-wire flow visualization," and is described by Corke, et al. (1977). In the present experiments, the smoke-wire used for flow visualization was a 0.13 mm diameter stainless steel wire which stretched from top to bottom of the test section through the tunnel walls. The top end of the wire passed through a No. 27G hypodermic needle and then into a 3.2 mm hollow brass cylinder, which was clamped to the outside of the tunnel. This cylinder served a two-fold purpose: a) to hold the smoke-wire in place, and b) to serve as a channel for the oil to reach the wire, as described below. The other end of the smoke-wire passed through the bottom of the test section where it was clamped to a hanging weight which provided constant tension in the wire. At either end

electrical connections were made so that current could pass through the wire. The scenario is as follows: Mineral oil is pumped through the hollow cylinder and through the hypodermic needle, forcing a large drop to fall down the smoke-wire. As the drop falls, surface tension causes the oil along the wire to break up into tiny beads or droplets. Two or three initial drops are typically used to provide a uniform distribution of smaller droplets along the span of the smoke-wire. At this point a current is passed through the wire, which heats it up sufficiently to cause the oil to burn. The result is rows of streaklines which mark the flow downstream of the smoke-wire. (The amount of current needed to accomplish this varies with tunnel speed, but is typically one ampere at a speed of 2 m/s.) After an adjustable time delay to allow the smoke to convect completely into the field of view, a camera is electronically triggered along with a strobe flash to record the streakline pattern on film.

The electronic synchronizing controller for the smoke-wire operation was built at the Illinois Institute of Technology, where this technique was perfected. For further details of its usage see Corke, et al. (1977). A Pentax ME-Super 35 mm camera with motor drive was used, along with a General Radio Model 1540 Stroboscope. We had the best success with Kodak Tri-x film pushed one stop, and printed on F-5 high contrast paper. The test section of the tunnel was plexiglass on 3 sides (top, bottom and front), and the back was wood that had been spray-painted a very flat black. The strobe was aligned perpendicular to the flow, shining up through the bottom, and the camera was positioned about a meter from the front of the test section.

#### **2.4. Instrumentation**

Freestream velocities were measured with a United Sensors pitot-static tube and an electronic Barocel manometer. The pitot-static tube was placed half-way between the top of the test section and the model axis in order to obtain

accurate freestream measurements as well as to minimize interference with the flow over the model.

Fluctuating velocities were measured with miniature hot-wire probes, purchased from T.S.I. (models 1260-T1.5 and 1248-T1.5). The single-sensor probe was a  $4\text{ }\mu\text{m}$  platinum-plated tungsten wire, with a length of 1.5 mm ( $L/d = 375$ ). It was mounted parallel to the longitudinal axis of the model, and with the probe body oriented at  $45^\circ$  with respect to the  $x$ -axis (direction of freestream). A six mm cylindrical strut supported the hot-wire assembly from the top; it was covered with an extruded aluminum airfoil-shaped tube to minimize vibration and disturbance. The entire assembly was mounted to an  $x$ - $y$  traverse which rested on top of the test section. The dual-sensor probe consisted of two wires in an "x" configuration, each wire  $45^\circ$  with respect to the freestream, but perpendicular to its neighbor. The wires were of the same diameter as that of the single-sensor probe described above. The dual-sensor probe was mounted parallel to the freestream such that the "x" lay in the  $x$ - $y$  plane. In this orientation  $u'$  and  $v'$  fluctuations could be measured as described in Appendix B. The strut, traverse, etc., were identical to those described above for the single-sensor probe.

A two-channel constant-temperature anemometer circuit was built in-house by Nosenchuck, et al. (1983). Some modifications to the circuit were required to obtain a very high signal-to-noise ratio. Its output was analyzed in one of two ways:

- a) For single-sensor real-time spectral analysis an HP 3582A spectrum analyzer was used, along with an  $x$ - $y$  plotter.
- b) For dual-sensor time-trace measurements, and for simultaneous hot-wire and smoke-wire measurements, a digital data acquisition system was used.

Following the schematic diagram of Figure 2.2, the anemometer output was sent to a signal conditioner which offset the DC component, amplified the signal to cover the full range of the 12-bit A/D converter (0 - 10 Volts), and applied a low-pass filter as an anti-aliasing precaution. An 8-bit microcomputer was used to sample and record the data digitally onto floppy disk. At a programmable time during sampling, the smoke-wire could be turned on, as well as the camera and strobe, in order to record simultaneous hot-wire data and smoke-wire photographs. The signal conditioner and relay unit were built by the author; the microcomputer was also built in-house by Nosenchuck, et al. (1983).

The hot-wire data were subsequently analyzed on GALT's DEC PDP-11 computer system.

## Chapter 3

### The Art of Flow Visualization

#### 3.1. Integration Effect of Streaklines

Flow visualization, though a very useful tool in fluid mechanics research, can often be misleading, as has been pointed out by Hooker (1936) and more recently by Hama (1962). The main problem with unsteady flows is that *streaklines* are not equivalent to *streamlines*, even though they are sometimes confused as such. In the laboratory, it is often more convenient to manufacture streaklines than streamlines; hence the former are much more popular among experimentalists. The most common method of streakline visualization is the steady introduction of a flow tracer (typically dye or smoke) from a fixed location in the flow. For wakes this location is usually upstream of the body, or else on the surface of the body itself. But a dye or smoke filament is distorted as it travels downstream, and the streakline pattern seen at some downstream location contains information integrated all the way back to its point of introduction. Thus, when studying a streakline one cannot be sure if a) the flow at a given location is *currently* experiencing the distortions implied by the streakline pattern, or b) that pattern is merely a remnant of the streakline's past history (an integrated "memory" as it were). Therefore, in order to visualize the true nature of the flow at a given location, it is desirable to introduce the flow tracer as close to that location as possible. Traditionally the hydrogen bubble technique in water has been useful because of this advantage; the smoke-wire technique in air is analogous and has been employed here.

As the case in point consider the two-dimensional Karman vortex street in the wake of a circular cylinder at low Reynolds number. Figure 3.1 shows a

series of photographs taken at different times and at progressively increasing downstream locations in the wake at  $Re = 90$ . The flow is from left to right, with the cylinder axis perpendicular to the plane of view. In each case the smoke-wire has been placed at the left-most edge of the field of view, and the photographs are aligned so that any vertical line passes through the same downstream location in all of the photographs. In photo a) the smoke-wire is just downstream of the cylinder; the vortex street is clearly marked and remains visible to the downstream end of the photograph ( $x/d = 200$ ). From photo a) alone one might conclude that the Karman vortex street is still active at this downstream location. In photos b) and c) the smoke-wire has been moved downstream to 50 and 100 diameters, respectively. The vortices are seen to be much weaker for these smoke-wire positions than would appear from photograph a) alone. In photo d) the smoke-wire is at  $x/d = 150$  and all the streaklines are parallel, which implies that the street at this location is so weak it can not be detected by the smoke-wire technique. This essentially parallel wake profile continues downstream with no further evidence of discrete vortices all the way to 350 diameters.

The integration effect of streaklines, as described above, is clearly demonstrated by comparing the flow pattern observed at  $x/d = 200$  in each of the photographs in Figure 3.1; the pattern is drastically different, depending on smoke-wire position. Photo a) shows what appears to be the Karman vortex street at  $x/d = 200$ . Photos b) and c) show a similar structure but much weaker, while photo d) indicates that no structure is present at this wake location. Which photo then can we trust? That is, how can we objectively describe the flow field from this confusing array of photographs? It is our contention that in order to accurately discern the flow at some location, the smoke-wire must be placed at a proper distance upstream of that location. If it is placed too far upstream, the streaklines become very distorted and may lead us to erroneous conclusions.



Likewise if it is placed too close to our observation point, the streaklines may not have had time to deform, again leaving us confused.

The clue to understanding this figure lies in the following: Suppose a streakline rolls up as it marks a vortex moving downstream. The resulting pattern will clearly indicate that vortex. Now suppose that the vortex, as it travels, decays at a much faster rate than the smoke diffuses. We can then argue that the smoke remains in its integrated pattern, even after the vorticity has largely diffused (leaving the vortex extremely weak). The streakline pattern is now fixed, and is simply convecting along with the mean flow, no longer changing its shape. This is exactly what we observe in photo a) of Figure 3.1; notice that beyond 100 diameters or so, the streakline pattern no longer changes significantly - it merely convects downstream. There is of course some shearing of the pattern, as the outside of the wake convects faster than the center. This can be seen in photo b) as well as in photo a) of Figure 3.1. Zdravkovich (1969) shows what he describes as extremely elongated elliptical vortices at  $x/d \approx 600$ ; his smoke was introduced at the cylinder, and therefore suffers the same integration effect as our photo a).

Keeping these concepts in mind, we can now answer the questions posed above. Each photograph in the figure is useful only for a finite distance downstream of the smoke-wire. To obtain an accurate description of the *entire* developing flow field, it is necessary to place the smoke-wire at various positions, and then look at the collage of pictures as a whole. For example, the very rapid decay of the Karman vortex street is not clear from any *one* of the photographs in Figure 3.1; but when the entire figure is studied simultaneously, the decay is quite evident. We should mention here that the smoke-wire itself has a wake, but the Reynolds number based on wire diameter is only about seven. At Reynolds numbers below forty or so, the wake of the smoke-wire is steady and only

influences the flow immediately downstream. We therefore consider the smoke-wire as essentially non-intrusive.

At this point the reader may be questioning the validity of the above argument for air flow, where the ratio of viscous to molecular diffusivity (Schmidt number) is of order unity. One may argue that as a structure in the flow is dissipated by viscosity, the smoke particles are diffused at nearly the same rate; smoke should not remain in a pattern for any longer time period than the lifetime of the structure generating that pattern. A simple explanation concerning this apparent dilemma is as follows: Smoke in air is actually composed of tiny aerosol-type particles, whose mass is significantly greater than the mass of surrounding air molecules. Hence diffusion of these particles is extremely slow on a molecular scale; we may then define an "effective Schmidt number" which is orders of magnitude larger than that for air alone. Lapple (1961) has calculated the diffusion coefficient of particulate matter into air at 25° C. For oil smokes, particle size is approximately 0.2  $\mu\text{m}$ , which gives a diffusion coefficient of about  $2 \times 10^{-6} \text{ cm}^2/\text{s}$ . In air,  $\nu \approx 0.16 \text{ cm}^2/\text{s}$ ; Our effective Schmidt number is thus of order  $10^5$ .

That the diffusion of smoke is indeed slow is clearly seen in Figure 3.1; if one follows a single streakline in the freestream outside of the wake, no significant dispersion of that streakline is observed (i.e., it does not broaden as it travels downstream). We can quantitatively estimate (by dimensional reasoning) that the width of a streakline in the freestream should grow like

$$\Delta w \sim \sqrt{\frac{Dz}{U_\infty}} \quad (3.1)$$

where  $D$  is the mass diffusivity and  $w$  the width of the streakline. In Figure

3.1,  $U_\infty = 115 \text{ cm/s}$ ,  $d = 0.13 \text{ cm}$ , and the total distance in our field of view (200 diameters) corresponds to about 25 cm. For  $D \approx 2 \times 10^6 \text{ cm}^2/\text{s}$ , the expected width increase at the end of the photograph is  $\Delta w \approx 6.6 \times 10^{-4} \text{ cm}$  ( $5 \times 10^{-3}$  diameters). Such a small width increase would be hardly noticeable; indeed in Figure 3.1 the initial width of the streakline is smaller than one cylinder diameter, and does not change significantly downstream.

### 3.2. Numerical Simulation of Streaklines

It is a relatively simple exercise to model streakline patterns numerically for a given velocity field. Following Hama (1962), we introduce marked "particles" at a fixed point, and track each particle in time as it is carried away by the velocity field (Lagrangian reference frame). Plotting a curve through each particle results in a numerical streakline (of infinite Schmidt number). This method was adapted here to simulate smoke-wire streaklines numerically at various downstream positions in a plane wake.

The velocity field chosen for this simulation is a convecting ideal Karman vortex street (Lamb 1945), modified to include the effect of viscosity. This model was originally suggested by Hooker (1936), and recently has been used by Davies (1976); details are given in Appendix A.

Figure 3.2 shows numerical results which simulate a cylinder wake at  $Re = 90$ . The "smoke-wire" is located at  $x/d = 0$  and at  $x/d = 100$ . Comparison of the two patterns shows the misleading integration effect of streaklines. When the point of introduction of the flow tracer is far upstream of the wake location being considered, its entire history is contained in the streakline pattern, and may confuse the interpretation. The conclusion from this exercise again is that extreme care must be taken when interpreting streakline patterns!

## Chapter 4

### Flow Visualization Results

#### 4.1. Decay of the Karman Vortex Street

As discussed in Chapter 3, an observation immediately apparent from Figure 3.1 is the very rapid decay of the Karman vortex street. This decay was found to occur at all Reynolds numbers we investigated. In each case, when the smoke-wire is placed far enough downstream of the cylinder, the shed vortices can no longer be found. Furthermore, the location of their disappearance seems to move upstream with Reynolds number. For  $Re = 90$  it occurs at about 125 to 150 diameters. For  $Re = 155$ , where the wake is just on the verge of transition to turbulent flow, the Karman vortex street can not be visualized beyond 75 to 100 diameters. (Of course, in this case a secondary wake structure is rapidly developing at this downstream location, as will be discussed in the following section.) For transitional and turbulent wakes ( $Re > 160$ ) the vortices are dissipated much more rapidly, and are not seen beyond  $x/D = 50$ .

The rapid decay of the Karman vortex street has been known for quite some time. For example Roshko (1953) found that for  $Re = 50$  and 100, the energy intensity of the Karman vortices is so low beyond 100 diameters, that background tunnel turbulence becomes significant. For Reynolds numbers in the "transition range" ( $150 < Re < 300$ ), the decay is even more pronounced. For turbulent wakes Roshko's results are again supported by the present experiments, where Karman vortices could not be seen beyond 50 diameters. Nevertheless, it seems that the full implication of this decay, particularly for laminar vortex streets, has been stifled due to misinterpretation of streakline photographs. For example, Zdravkovich (1969) shows what appear to be very

elongated Karman vortices at  $x/d = 800$ ! In light of our discussion of streakline integration effects in Chapter 3, his elongated ellipses are merely the integrated pattern from far upstream. Tritton (1977) states that "... the vortex street continues to all distances downstream," again a misinterpretation of streakline patterns. In actuality, the Karman vortex street has completely decayed by at most one or two hundred diameters. Indeed, based on this rapid decay, the rows of vortices should not really be called a "street" at all (the original term having implied a long, regularly-spaced pattern). In Chapter 5 we take a quantitative look at this decay, using hot-wire anemometry.

#### 4.2. The Secondary Vortex "Street"

Because we are able to mount smoke-wires at any desired position, the smoke-wire technique is convenient for studying development of downstream structure in a wake. In particular, placement of a smoke-wire at positions beyond which the Karman vortex street has largely decayed yields some interesting results. For Reynolds numbers less than about 100, we do not observe any further reorganization or development of large structure in the far wake. Figure 3.1 shows a typical case ( $Re = 90$ ). Notice that beyond  $x/d = 150$ , the streaklines in photo d) are parallel, with no apparent regions of concentrated vorticity. For these low-Reynolds-number wakes, large secondary structure could not be seen as far downstream as we investigated, which was about 500 diameters (not shown in Figure 3.1).

For  $100 < Re < 180$ , a structure quite similar to that of the Karman vortex street, but of larger scale, is observed. Three cases in this Reynolds number range are shown in Figures 4.1 through 4.3, at  $Re = 130, 140$ , and  $155$  respectively. The photos are aligned in the same manner described for Figure 3.1. The "strength" of the secondary street may be determined by how quickly the streaklines deform. From these photographs and others, we observe that the

strength increases with Reynolds number in the range  $100 < Re < 160$ . The scale of this structure is roughly 2 to 3 times that of the primary Karman street. Figure 4.3 shows some of the strongest and most regular secondary structure that we have recorded on film. Photos b) and c) represent identical tunnel conditions, but were taken about ten seconds apart. Both are included here to illustrate that the secondary structure is not always continuous - it comes and goes in time. Photo b) shows an irregular secondary street; this is a more typical case than photo c), where an unusually regular and strong street has been captured. Three-dimensionality may play an important role in determining how regular the downstream structure appears in these edge views. We discuss three-dimensionality in Chapter 6.

For  $Re > 160$  the wake becomes turbulent, making flow visualization extremely difficult. Taneda (1959) reports having seen a secondary street at high Reynolds number, but only after several hundred diameters. Matsui and Okude (1980) could not find any such street for  $Re > 160$ , although they had not looked as far downstream as had Taneda. In the present experiments we did not find a well-organized, easily-recognizable secondary "street" for  $Re > 160$ . However, "groups" or "bursts" of large vortical structures can sometimes be observed, similar to those observed by Grant (1958) and Townsend (1979). Figure 4.4, for example, shows a cylinder wake at  $Re = 190$ . Notice that after the Karman street decays, the wake becomes very disorganized. However, if we follow a streakline in the outer edge of the wake at  $x/d \approx 200$ , (photo b)) we see a somewhat regular wavy pattern, of a scale much larger than the original Karman street. Figure 4.5 shows the wake at  $Re = 2200$ ; some of this structure can also be observed in photo b) at  $x/d \approx 250$ . Here the structure is more regular than for the case at  $Re = 190$ .

#### 4.3. Porous Flat Plate Wakes

It is important to note that in all the above cases, secondary structure emerges *after* the primary (Karman) street has largely decayed. The secondary structure therefore appears to develop independently; for example its scale (or frequency) is not necessarily in a fixed ratio to that of the primary street. This observation leads us to suspect that the secondary structure results from an instability of the mean wake profile. It therefore seems reasonable to assume that if we can produce a wake which initially has no Karman vortex street, a street-like structure may emerge downstream due to wake instability. Such a wake is produced by a porous flat plate aligned normal to the flow direction, provided the solidity  $\sigma$  is lower than about 80%, according to Castro (1971).

Two porous plate wakes are shown in Figures 4.6 and 4.7. In the first case, the plate is very porous ( $\sigma = 29\%$ ), and the wake immediately downstream shows no structure of any scale. Presumably all that exists is a laminar "top-hat" velocity profile. At about 10 diameters downstream (Figure 4.6a), a shear layer instability leads to the growth of small vortices on either side of the wake. These vortices amalgamate, and as they grow they arrange themselves eventually into a fairly regular vortex street pattern at  $x/d \approx 20$ , presumably caused by far-wake instability. At conditions similar to ours, Castro (1971) observed a dominant frequency in the wake, which he also attributed to hydrodynamic instability of the mean velocity profile.

The second case (Figure 4.7) is for a porous flat plate with a much higher solidity ( $\sigma = 47\%$ ), but at approximately the same Reynolds number. The obvious difference here is the abundance of small-scale turbulent structure immediately downstream of the plate. Notice however that the body is still not solid enough to shed a Karman vortex street. Nevertheless, this wake also goes unstable downstream, and by 30 or 40 diameters a well-defined vortex street is observed.

Indeed, if we could ignore the small-scale structure superposed on this flow, Figure 4.7 is strikingly similar to Figure 4.6. Valensi (1974) shows a similar photograph for a plate with  $\sigma = 53\%$  at  $Re = 5 \times 10^4$ .

Hot-wire measurements for the second case above are discussed in Chapter 5.



## Chapter 5

### Hot-Wire Measurements

#### 5.1. Exponential Decay of the Karman Vortex Street

Smoke-wire flow visualization of the far wakes of bluff bodies has given us new qualitative insight into Taneda's phenomenon of vortex street breakdown and rearrangement. We now present the results of hot-wire measurements which give us *quantitative* information about this process.

To obtain detailed velocity measurements in the wake, we used a "cross-" or "x-" wire, as discussed in Chapter 2, along with a digital data acquisition system. The calibration procedure and details of the data acquisition are described in Appendix B. Specific details, such as freestream velocity, cylinder diameter, mean velocity profiles, etc., as well as a description of the methods used to analyze the data, can also be found in that appendix.

First, let us consider the decay of the Karman vortex street as downstream distance is increased. As had been pointed out by Bevilacqua (1975), velocity fluctuations due to a vortex street are more readily detected in the cross-wake ( $v$ ) velocity component. Hence consider the  $v'$  fluctuations, where  $v = V + v'$ . In Figure 5.1 we plot the amplitude spectrum of  $v'/U_\infty$  for a circular cylinder wake at  $Re = 150$  and at  $x/D = 25$ . (Amplitude spectrum is the square root of power spectrum; the units are in percent of freestream velocity.) As expected, a delta function spike is seen at the shedding frequency,  $f_k$ , which is the only significant frequency in the near wake. Such spectra were taken at each  $x$ -location, averaged at the two  $y$ -locations corresponding to inflection points in the mean velocity profile (one on either side of the wake). Discrete spectral

amplitude at  $f = f_k$  is plotted against downstream distance  $x/d$  in Figure 5.2 for  $Re = 140$  and well as for  $Re = 150$ . For both Reynolds numbers, the amplitude is seen to decay exponentially for  $25 < x/d < 150$ . By least-squares fitting a straight line through the first 6 or 7 data points in Figure 5.2, we obtain initial decay rates of 0.0246 decades per diameter for  $Re = 150$ , and 0.0249 decades per diameter for  $Re = 140$ . Similar decay rates have been reported for the  $u'$  fluctuations by other investigators as well. Hussain and Ramjee (1976) obtained hot-wire traces of  $u'$  at  $Re = 145$  for various downstream distances. From their Figure 4, the amplitude of the fluctuations can be seen to decay exponentially in the region  $5 < x/d < 60$ . In our earlier work (Cimbala, et al. (1981)) at  $Re = 155$ , we measured discrete  $u'$  fluctuations at the shedding frequency, and found  $u'_{rms}$  to decay exponentially up to 100 diameters. Matsui and Okude (1981) made similar measurements at  $Re = 140$ , while Desruelle (1983) showed an exponential decay for three different Reynolds numbers. The decay rates for all these cases are summarized below:

<i>Reference</i>	<i>Velocity</i>	<i>Re</i>	<i>Decay Rate</i> (decade/diameter)
Desruelle (1983)	$u'$	80	0.0143
Desruelle (1983)	$u'$	120	0.0169
Present Results	$u'$	140	0.0187
Present Results	$v'$	140	0.0249
Matsui & Okude (1981)	$u'$	140	0.0170
Hussain & Ramjee (1976)	$u'$	145	0.0156
Present Results	$u'$	150	0.0209
Present Results	$v'$	150	0.0246
Desruelle (1983)	$u'$	155	0.0225
Cimbala, et al. (1981)	$u'$	156	0.0167
Present Results	$u'$	500	0.0284
Present Results	$v'$	500	0.0305

The general trend is faster decay rates with increasing Reynolds number. This is especially apparent when we only consider data from one facility (e.g., the three rates of Desruelle, or our present results). There is much scatter in the data from different facilities; the decay rate is probably sensitive to background disturbances in the freestream.

## 5.2. Downstream Structure

As downstream distance in the wake is increased, fluctuations appear at frequencies lower than the shedding frequency. Figure 5.3 shows amplitude spectra at several downstream positions for  $Re = 150$ . As in Figure 5.1, the spectra are averaged over the two  $y$ -locations where the slope of the mean velocity profile is a maximum (inflection points). We observe in Figure 5.3 a shift to

lower and lower frequencies as  $x/d$  is increased. In particular, the Karman frequency ( $f_k \approx 166$  Hz) is initially the only significant frequency. At  $x/d = 100$  in Figure 5.3 a broad band of frequencies has arisen with the most-prominent peak at  $f \approx 90$  Hz, and other peaks at  $f \approx 120, 83$ , and 70 Hz. By  $x/d = 200$ , disturbances at  $f \approx 90$  and 70 Hz have amplified significantly, as well as the subharmonic ( $f = 83$  Hz); the peaks at  $f = f_k = 166$  Hz and at  $f = 120$  Hz have decayed. With further increase in  $x/d$ , the band of prominent disturbances shifts to lower frequencies and broadens. At  $x/d = 400$  the most-prominent band of frequencies is centered around 70 Hz, while all frequencies above 100 Hz have disappeared. By  $x/d = 750$ , there are no longer any outstanding spikes; instead, a very broad hump is seen for  $0 < f < 75$  Hz. In general, following the life-cycle of a particular frequency, we notice that the fluctuation amplitude at that frequency first rises, then decays; the lower the frequency, the further downstream is its life-cycle. In Figure 5.4 we have plotted spectral amplitudes at several discrete frequencies versus downstream distance. The growth-decay cycle is clear.

Notice in Figure 5.4 that there is nothing outstanding about the subharmonic,  $f = 83$  Hz. That is to say, disturbances at the subharmonic experience the same kind of growth and decay as at any other nearby frequency. For example, the growth-decay cycle at  $f \approx 90$  Hz leads the one at the subharmonic by about 20 diameters, but is almost identical in magnitude and shape.

Figure 5.5 shows amplitude spectra at a lower Reynolds number of 140. Here the shift to lower frequencies is more "choppy;" i.e., the peaks in the spectra are not as broad as those for  $Re = 150$  - it appears that a large percentage of the fluctuation energy is concentrated at discrete frequencies which are almost integral multiples of 25 Hz. The reason for this behavior is not entirely clear. As seen in Figure B.8 (Appendix B), tunnel disturbances were strong at 25 Hz and

its harmonics relative to other freestream disturbances - the wake may have "locked in" at these frequencies in response to the external forcing. Figure 5.6 shows spectral amplitudes at several of these discrete frequencies as a function of  $x/d$ . Their growth-decay cycles are very similar to those of the wake at  $Re = 150$ .

Figure 5.7a) also shows amplitude spectra, but at a cylinder Reynolds number of 500, where the wake is turbulent. In this case spectral peaks are much less prominent because of fluctuations at all frequencies. A broad hump is discernible, however, and shifts to lower frequencies much more smoothly than for the laminar cases above. Notice that the magnitude of the entire spectrum decays with downstream distance, as energy is dissipated by turbulent mixing. Figure 5.8a) shows growth-decay cycles at  $Re = 500$ ; we don't really see regions of growth, but rather decay at each discrete frequency. In this case it is useful to display *normalized* spectra where  $v'$  is divided by the local mean velocity defect  $\Delta U$ , where  $\Delta U = U_{\infty} - U_0 = U_{\infty} W_0$ , instead of by  $U_{\infty}$ . Figures 5.7b) and 5.8b) are normalized versions of Figures 5.7a) and 5.8a) respectively. These normalized plots illustrate the growth-decay cycles much more clearly.

In Figure 5.7c) we show normalized spectra at all twelve downstream positions. Here we have normalized frequency as well as spectral amplitude, in the manner discussed in Section 5.4 below. The fully normalized spectra show a self-similar behavior beyond about 100 diameters. The center of the spectral peak in these coordinates occurs at approximately  $\beta = 1.5$ . The band of prominent frequencies is very wide, much more so than for the case of a plane mixing layer. This is most likely due to the much slower divergence of wakes than mixing layers. In Section 5.4 we compare these results with predictions of linear stability theory.

### 5.3. The Group Phenomenon

By studying time-traces of velocity fluctuations, as in Figure 5.9, at  $Re = 150$ , it becomes evident that the secondary structure occurs in groups. (Groups are defined as packets of large fluctuations, lasting for several cycles, and followed by periods of relative calm.) Recall from Chapter 1 that Townsend (1979) had observed this phenomenon for the turbulent cylinder wake. His results show that the frequency or scale of the fluctuations is constant within a particular group but varies from group to group. Here we wish to quantify this variation — i.e., how much of a spread in frequency is there?

Long-time-averaged power spectra tell us little about the *instantaneous* structure in a flow field. However, much can be learned by examining the short-time-averaged power spectrum of each group of structures. Details of the numerical technique used here are presented in Appendix B. Basically, the most-energetic frequency of each group is recorded; a probability density function (PDF) of the spectral peaks is then calculated for all these frequencies, weighted by the amplitude of the fluctuations.

Figure 5.10 shows spectral-peak probability density vs. frequency at several downstream positions in the cylinder wake at  $Re = 150$ . Close to the cylinder, the shedding frequency ( $f_k \approx 166$  Hz) is dominant and the width of the PDF is extremely small, as expected. At  $x/D = 100$ , the dominant frequency shifts to about 90 Hz. As we continue downstream we see a shift to lower frequencies as well as further broadening of the frequency band-width, just as had been observed in the spectra of Figure 5.3.

The width of the spectral-peak PDF is significant. For a given frequency band to have non-zero probability density, the passage frequency of at least one group of definable structures has to lie within that frequency band. Whereas power spectra only give us a measure of the energy content of fluctuations at a

given frequency, probability densities tell us that identifiable groups of energetic fluctuations occur at discrete frequencies. The broader the width of the PDF, the more distributed are the frequencies of these groups. Thus our results support Townsend's (1979) observation that far-wake structure occurs in groups; the frequency within a group being fairly constant, but varying from one group to the next. The significance of this result will be more apparent in the following section, where we compare our data to linear stability theory.

Another interesting result is the average number of cycles,  $n_g$ , within a group. The original Karman street of course is practically continuous, and  $n_g$  is extremely large. Figure 5.11 shows how  $n_g$  varies with downstream distance beyond 100 diameters, after the Karman street has largely decayed. In general,  $n_g$  lies between about 2 and 12, but seems to decrease slowly with  $x/d$ .

#### 5.4. Comparison with Linear Stability Theory

Inviscid linear stability of a parallel wake profile has been analyzed by many investigators, both in the temporal and spatial modes. Our intent here is to compare predictions from these analyses with our experiment results. Namely, for the measured mean velocity profiles, how well can linear theory predict which frequencies are most prominent in the wake? It is convenient to express the frequency non-dimensionally as in Figure 5.7c). We define

$$\beta = \frac{2\pi\delta f}{U_\infty} \quad (5.1)$$

where  $f$  is the dimensional frequency, and  $\delta$  is the wake half-width, defined by the  $y$ -location where  $U^* = 0.5$ .  $U^*$  is the normalized mean velocity,

$$U^* = \frac{U - U_{\infty}}{U_0 - U_{\infty}}, \quad (5.2)$$

and  $U_0$  is the mean centerline velocity.  $U_0$  and the wake half-width  $\delta$  are calculated by fitting a Gaussian profile to the measured mean velocities, as described in Appendix B.

For comparison with experiment, spatial stability analysis is preferred over temporal analysis, as has been pointed out by Mattingly and Criminale (1972). Kubota (1983) has generated numerical solutions for both cases; inviscid disturbances are superposed on a parallel Gaussian wake profile. Details of this effort are given in Appendix C. Figure 5.12 shows spatial growth rate  $-\alpha_i$  as a function of dimensionless frequency  $\beta$ , and for several values of  $W_0$ , the normalized centerline velocity defect in the wake. ( $W_0 = 1 - U_0/U_{\infty}$ .) Recall that for spatial stability analysis, frequency  $\beta$  is real, while wave number  $\alpha$  may be complex. Figure 5.13 shows a similar family of curves for the temporal mode, where  $\alpha$  is real and  $\beta$  may be complex. We plot *spatial* growth rate  $g$ , however, using the transformation discussed in Appendix C. Notice that there is not a great discrepancy between the two modes. We are not concerned here with predicting fluctuation amplitudes exactly; our main concern is the *relative* amplitude of fluctuations at various frequencies. Toward this end either mode is applicable; we have chosen the temporal mode for convenience in our analysis below. Another important thing to note in either figure is that as velocity defect decreases, the growth curve shifts toward higher  $\beta$ . Thus, as we travel downstream in the wake,  $W_0$  decreases, and the relevant growth curve is continually shifting to the right, as well as decaying in magnitude.

Kubota (1983) has argued that the growth curves shown in Figure 5.12 or 5.13 may be extended to negative growth (de-amplification) beyond the neutral point.



$\beta_n$ . This is extremely important in the following analysis, where such a de-amplification region is required in order to predict growth-decay cycles of large-scale structures. For lack of details in this region, we have extrapolated the growth curves in Figure 5.13 by straight lines, whose slopes are matched with those at the neutral points.

Let us consider which prominent frequency  $f_p$  we expect to find in our measurements; i.e. we wish to predict  $f_p$  as a function of downstream distance  $x$ . At first glance one may expect  $f_p$  to equal the locally most-amplified frequency (the peak in the growth curve). This turns out not to be the case however, due to non-parallelism of the mean wake. It must be remembered that the growth rates shown in Figure 5.13 are calculated for a parallel wake (no  $x$ -dependence); the real wake of course is not parallel, but widens downstream. Obviously the best predictions would come from fully-non-parallel stability analysis, where one includes downstream-widening of the mean wake; nevertheless we expect the curves in Figure 5.13 to be adequate approximations locally. Hence, a scheme was developed to approximate non-parallelism ( $x$ -dependence) using only parallel stability calculations. Namely, in order to predict how large a disturbance to expect at some particular frequency, we integrate growth rate at that frequency with respect to downstream distance  $x$ . Doing this for a number of frequencies gives us disturbance amplitude as a function of frequency for each downstream distance. It is then a simple matter to find that frequency which is predicted to be the most prominent,  $f_p$ , as a function of  $x$ , (i.e., the frequency whose amplitude is greatest at a given  $x$ -location). The entire process is outlined below:

1. Measure mean velocity profiles at several downstream positions in the wake.
2. Calculate (with least-squares fitting to a Gaussian wake profile) the half-width  $\delta$  and centerline velocity defect  $W_0$  for each  $x$ -position. (Examples are

shown in Figure 5.14.)

3. Fit smooth continuous curves through  $W_0$  and  $\delta$  so as to obtain  $W_0(x)$  and  $\delta(x)$ . Examples are shown in Figures 5.15 and 5.16, respectively.
4. The appropriate growth-rate curve  $g(x, f)$ , such as those shown in Figure 5.13, is chosen locally for each  $x$  according to  $W_0(x)$ ,  $\delta(x)$ , and Equation (5.1). ( $g$  is extrapolated to negative growth rates, as discussed above.)
5. Knowing  $g(x, f)$ , we assume a locally exponential growth of amplitude  $A$ ; namely,

$$\frac{\partial A(x, f)}{\partial x} = g(x, f) \cdot A(x, f). \quad (5.3)$$

We can predict the amplitude of fluctuations at frequency  $f$  and at location  $x$  by integrating the exponential growth from  $x = 0$  to  $x$ , i.e.,

$$A(x, f) = A_0 \exp \left[ \int_0^{x'} g(x', f) dx' \right]. \quad (5.4)$$

where  $A_0(f)$  is the initial perturbation amplitude at frequency  $f$ , and  $x' = x/\delta(x)$  is the non-dimensionalized downstream distance. In Figure 5.17 we show  $A(x, f)$  versus  $x/\delta$  for a number of fixed frequencies  $f$  at  $Re = 150$ . We have assumed, for simplicity, that  $A_0(f) = 1 = \text{constant}$  for all  $f$ . Notice the growth-decay cycles, similar to our experimental results.

6. To find the frequency  $f_p(x)$  where the amplitude given by Equation (5.4) is a maximum, we simply take the partial derivative of  $A(x, f)$  and set it to zero:

$$\frac{\partial A(x, f)}{\partial f} = A_0 \exp \left[ \int_0^{x^*} g(x^*, f) dx^* \right] \left[ \int_0^{x^*} \frac{\partial g(x^*, f)}{\partial f} dx^* \right] = 0,$$

or, at  $f = f_p$ .

$$\int_0^{x^*} \frac{\partial g(x^*, f)}{\partial f} dx^* = 0. \quad (5.5)$$

7. Compare this predicted peak frequency,  $f_p(x)$ , to the measured peak frequency at each  $x$ -location.

Let us now examine our experimental results at  $Re = 150$  in light of the above discussion. We show in Figure 5.18 a plot of frequency versus  $x/d$ . The circles represent experimental frequencies at which the most-prominent disturbances were measured. The vertical lines represent 70% confidence levels, and give the reader a feel for the band-width of prominent frequencies. These observed  $f_p$  should be compared to the predicted  $f_p$  as described above — given here as the solid line. Also shown in Figure 5.18 are the locally neutral frequency (dashed line), and the frequency corresponding to the locally most-amplified disturbance (dotted line). Note that, because of the integration, the frequency which is locally most-amplified is not necessarily the frequency with the largest (integrated) amplitude.

Close to the cylinder, the Karman frequency is the most-prominent observed frequency, as expected. Comparison with linearized theory is futile in the very near wake where the amplitude of fluctuations can exceed 30% (Nishioka and Sato (1978)). Note that the Karman vortices are initially formed by a mechanism much different than far-wake instability. The mechanism consists of a

complex combination of unsteady boundary-layer separation and near-wake instability, and is not yet completely understood. We therefore do not expect  $f_k$  to match our far-wake predictions. Indeed, it is interesting in Figure 5.18 that the Karman frequency is well above our predicted peak frequency. In fact,  $f_k$  even lies above the locally neutral frequency  $f_n$ , and is thus in the region of damping, according to stability theory. This is consistent with our observation that fluctuations at Karman frequency  $f_k$  decay exponentially in the region  $25 < x/d < 125$ .

As disturbances at  $f_k$  decay rapidly, lower frequencies take over; beyond  $x/d = 100$  the agreement between predicted and observed frequencies is quite good.

Figure 5.19 shows a similar comparison for  $Re = 140$ . Again,  $f_k$  ( $\approx 149$  Hz) lies above the neutral curve; fluctuations at  $f_k$  decay beyond our first measurement station ( $x/d = 40$ ). Lower-frequency disturbances become prominent beyond 100 diameters, and the agreement with the predicted frequencies is again quite good. Subharmonic  $f_k/2 \approx 75$  Hz seems to lock in for  $125 < x/d < 250$ . Beyond  $x/d = 250$ ,  $f_k/2$  lies above the neutral curve; lower-frequency fluctuations arise as the subharmonic decays. The 70% confidence level bars are quite short; this implies very narrow band-widths, as had been observed previously in the spectra at this Reynolds number. (See Figure 5.5.)

Figure 5.20 shows the comparison between theory and experiment for the case of a turbulent cylinder wake at  $Re = 500$ . Here,  $f_k$  is approximately 630 Hz, and is off the scale. In this case  $f_k$  is prominent only in the very near wake. Already by  $x/d = 50$ , a lower-frequency band (centered around  $f_p \approx 290$  Hz) is prominent. Notice that the observed  $f_p$  decreases quite smoothly with  $x$  as we travel downstream. 90% confidence levels have been chosen; the band of prominent frequencies is very broad. Interestingly, our observed  $f_p$  lies above the predicted  $f_p$ ; in fact, it follows almost exactly the locally *neutral* frequency  $f_n$ .

It is unclear why our prediction scheme works so well for  $Re = 140$  and  $150$ , but not for  $Re = 500$ . At  $Re = 500$  the wake is turbulent, and fluctuations are strong at all frequencies in the range of interest. Recall from Figures 5.7a) and 5.8a) that fluctuations at any given frequency never really have a chance to "grow," since the entire power spectrum decays with  $x/d$ . The most-prominent frequency  $f_p$  is then the one which suffers the least *integrated* decay as the disturbances travel downstream. That frequency is apparently the locally neutral frequency  $f_n$ , as Figure 5.20 shows. No attempt has been made in our calculations to account for the additional rapid decay of fluctuations due to turbulent stresses. Perhaps a more rigorous model is necessary. We may point out here that similar results have been shown recently by Wygnanski, et al. (1983) for the case of a plane turbulent wake at  $Re = 4000$ . Namely, the observed prominent frequency matches well with the neutrally amplified frequency, as predicted by linear stability theory. Ho and Huerre (1984) have observed this agreement for the case of a plane turbulent mixing layer as well. Lessen and Singh (1974), using eddy viscosity models, have postulated a similar behavior for *axisymmetric* turbulent jets and wakes.

Indeed, it is surprising that such a simple prediction scheme as employed here (with local parallelism) works as well as it does. We may conclude from this exercise that two-dimensional inviscid parallel hydrodynamic stability theory, when interpreted properly, is adequate to predict which frequencies are expected in a far wake. Furthermore, this agreement supports our hypothesis that structure appearing far downstream of a bluff body is the result of hydrodynamic instability of the mean velocity profile, and is not directly dependent on the shed vortices of the Karman vortex street.

### 5.5. A Look at $y$ -Dependence

As discussed in Chapter 2, "on-line" spectral analysis was also done with a single inclined hot wire and a digital spectrum analyzer. In particular, we are interested in the dependence of amplitude spectrum on distance from the wake centerline ( $y$ -direction). Figure 5.21 shows long-time-averaged amplitude spectra in a circular cylinder wake at  $Re = 300$ , at  $x/d = 750$ , and at several  $y$ -locations. Output from the hot-wire anemometer was input directly to the spectrum analyzer, without any linearization; the amplitude scale is therefore in arbitrary (log) units. (Velocity fluctuations are very small this far downstream; hot-wire response is assumed to be linear.)

Close to the centerline ( $0 < y/d < 15$ ), no peak in the spectrum can be found. For  $y/d > 15$  however, a broad-band peak in the spectrum exists; furthermore, the band shifts to lower frequencies and becomes narrower as we travel outward in the wake. The most-prominent frequency  $f_p$  is plotted as a function of  $y/d$  in Figure 5.22; an almost linear decrease in  $f_p$  is seen.

We can explain this frequency shift as follows: The wake profile at a particular  $x$ -location is unstable to a broad band of frequencies. Fluctuations at high frequencies may be measured occasionally, the scale of which is smaller than the local wake scale. We can think of these structures as originating upstream of our measurement position. Because of their smaller scale, they will be sensed more readily by a probe nearer the wake centerline. When the probe is near the outer edge of the wake, it can only sense structures of larger scale (lower frequency), which can be thought of as originating further downstream. These ideas are sketched in Figure 5.23. Sketch a) shows high-frequency structures which originate upstream and are sensed at probe position  $y_1$  but not at  $y_2$ ; sketch b) shows lower-frequency structures which can be sensed at probe position  $y_2$ .

### 5.6. Simultaneous Smoke-Wire and Cross-Wire Records

The microprocessor was programmed such that a smoke-wire photograph could be taken at any specified time during the data-collection interval. As illustrated in Figure 2.2, the microprocessor first sends a pulse to the relay unit, which turns on the smoke and opens the camera shutter (the room is dark, of course). After a specified delay to allow the smoke to convect completely into the field of view, the strobe is triggered to flash once. Subsequently the smoke is turned off, and the camera shutter closed.

The sequence outlined above enables us to display smoke-wire and hot-wire records simultaneously; an example is shown in Figure 5.24 for a cylinder wake at  $Re = 150$ . The smoke-wire is at  $x/d = 275$ , while the cross-wire is positioned at  $x/d = 400$  and at  $y/d = -4$ . Note that in order to avoid damage to the hot wires, the cross-wire assembly was moved slightly out of the plane of smoke. The time trace in Figure 5.24 has been displayed "backwards" (i.e., time increasing to the left), so that direct comparison between the flow-visualization photograph and time-trace is possible. The scales have been matched according to

$$t = \frac{x}{U_c} \quad (5.6)$$

where  $U_c$  is the local convection velocity (assumed to be the mean velocity at the location of the probe). In this example,  $d = 0.0016$  m,  $U_\infty = 1.528$  m/s. and  $U_c = 1.397$  m/s. The time axis has also been shifted such that the strobe flash occurs at  $t = 0$ .

Because of the integration effect of streaklines, as discussed in Chapter 3, we do not expect the time-trace to exactly match the distortions of streaklines in the photograph. Nevertheless, a general agreement is certainly present. Notice for example the burst of orderly structure at  $-60 < t < 0$ ; large-scale vortices

are clearly seen in the photograph at  $400 < x/d < 460$ . Just ahead of the probe ( $350 < x/d < 390$ ) there appears in the photograph a smaller-scale group of vortices. This is also recognizable in the time-trace as a very weak higher-frequency oscillation. Short-time spectra of the fluctuations shown in Figure 5.24 give frequencies of 64 Hz for the larger-scale structure, and 84 Hz for the smaller-scale structure. Both of these frequencies are within the range of amplified frequencies, according to linear stability theory, as can be seen in Figure 5.18 at  $x/d = 400$ .

Both the time-trace and smoke-wire photograph of Figure 5.24 support Townsend's suggestion that far-wake structure appears as groups of several vortices. Such a hypothesis is consistent with the explanation that downstream structure arises because of wake instability of the mean velocity profile and not directly because of vortex amalgamation. Furthermore, Figure 5.24 shows that far-wake structure convects at the local mean velocity; it does not appear to have unequal group and phase velocities.

### 5.7. Porous Flat Plate Wake Surveys

Cross-wire surveys were also taken in the wake of a 47% solid flat plate at  $Re_d = 5000$ , where  $d$  is the width of the plate. Mean velocity profiles are shown in Figure 5.25. As expected, very near to the plate the profile is a sharp "top hat" which gradually relaxes as the shear layers on either side of the wake begin to merge. By ten diameters the profiles are far-wake-like, and have been fitted here with Gaussians.

Amplitude spectra of  $v'/U_\infty$  are plotted in Figure 5.26 for several  $x$ -locations; each spectrum is averaged at the two inflection points of the mean velocity profile, as discussed previously. At  $x/d = 1$ , spectral energy at low frequencies is small, but there is a noticeable bump centered around 410 Hz. Recall from our flow-visualization results that the plate does not appear to shed Karman-type



vortices; the peak in the spectrum may instead be associated with the plane shear layers which exist initially on the outer edges of the wake. We can calculate the local Strouhal number of one of these shear layers:

$$St = \frac{f \theta_{SL}}{\bar{U}}, \quad (5.7)$$

where  $\theta_{SL}$  is the shear layer integral thickness,

$$\theta_{SL} = \int_{-\infty}^{\infty} \left( \frac{U - U_1}{U_2 - U_1} \right) \left( 1 - \frac{U - U_1}{U_2 - U_1} \right) dy, \quad (5.8)$$

and  $\bar{U}$  is the average of  $U_1$  and  $U_2$ . At  $x/d = 1$  in Figure 5.26 we have  $U_1 = 2.39$  m/s,  $U_2 = 4.54$  m/s, and  $\theta_{SL} = 0.0507$  cm. For  $f = 410$  Hz, Equation (5.7) gives  $St = 0.06$ , which is consistent with the observations of Ho and Huerre (1984) for a growing free shear layer. Namely, they report that  $St = 0.032$  when the shear layer first begins to oscillate, and  $St = 0.079$  further downstream as the shear layer grows. Our value lies between these two extremes, which confirms our speculation that the peak at  $f = 410$  Hz is associated with the shear layers on either side of the wake, and *not* with any kind of Karman-type vortex shedding.

At four diameters downstream the amplitude spectrum is devoid of any outstanding peaks, except for a very broad band centered at approximately 150 Hz; the peak at 410 Hz has disappeared. We shall designate the range  $4 < x/d < 10$  as a transition range, where the stability problem changes from that of two (independent?) plane shear layers to that of a plane far wake.

At  $x/d = 10$  the spectrum has increased in magnitude at the lower frequencies, and in particular there is a broad hump centered around 75 Hz. Beyond 10 diameters, in the "far wake" region, the peak in the spectrum shifts to lower

frequencies (larger scales) as downstream distance increases.

Figure 5.27 shows a comparison between observed and predicted prominent frequencies  $f_p$ ; the predicted values come from our locally-parallel stability analysis, as discussed in Section 5.4. The agreement is quite good beyond  $x/d = 10$ , in the far-wake region. 75% confidence levels are also plotted in Figure 5.27 to indicate the band-width of prominent frequencies.

Direct comparison between circular cylinder wakes and wakes of other bluff bodies can be accomplished by equating Reynolds number based on momentum thickness  $\theta$ , where

$$\theta = \int_{-\infty}^{\infty} \frac{U}{U_{\infty}} \left( 1 - \frac{U}{U_{\infty}} \right) dy. \quad (5.9)$$

For the case of the 47% solid plate discussed here, we have  $d = 1.78$  cm,  $\theta/d = 0.35$ , and  $U_{\infty} = 4.54$  m/s;  $Re_{\theta}$  is therefore equal to 1750. For our circular cylinder wakes we found  $\theta/d \approx 0.6$ ;  $Re_{\theta}$  is thus 60% of  $Re_d$ .

## Chapter 6

### Three-Dimensional Effects

#### 6.1. Unforced Three-Dimensionality

Up to this point our discussion has been confined to the x-y plane; now let us consider three-dimensionality. Possibly the earliest experiments on far-wake structure are those of Townsend (1956) and of Grant (1958). Grant's work, an extension of Townsend's, consists of measured velocity correlations in the far wake ( $\approx 500$  diameters) of a two-dimensional cylinder at  $Re = 1300$ . A peculiar *three-dimensional* structure was inferred from these time-averaged measurements, and was christened the "vortex-pair eddy," later called the "double-roller eddy" by Townsend (1970). More detailed calculations by Payne and Lumley (1967) of Grant's data yielded a similar structure.

Since that time, neither the instantaneous nature of this structure nor its origin have been adequately explained, although there has been some speculation (see for example, Keffer (1965), Townsend (1970), Roshko (1976) and Townsend (1979)). In particular, Roshko (1976) suggested the structure may actually be the time-averaged superposition of vortex loops, formed by the pinching off and joining together of vortices from opposite sides of the street. That long-time-averaging seriously distorts one's interpretation of the instantaneous structure was also mentioned by Townsend (1979). He suggested that time-averaging of the large-scale velocity patterns "makes them appear more complex because of the superposition of patterns from eddies at all stages of ... [his proposed] growth-decay-renewal cycle." An excellent discussion of some of these ideas is offered by Wlezien (1981).

Most recently Mumford (1983), using a pattern-recognition technique, suggests that the double-roller eddies may be even more complex than previously thought. He found that the structures are often confined to one side of the wake centerplane, rather than extending across the entire wake. Furthermore, eddies of similar type tend to occur in groups of two or more, one after another in the streamwise direction

Regardless of its exact nature, it is interesting that the characteristic large structure far downstream in a plane wake appears to be three-dimensional.

The smoke-wire flow-visualization setup was modified for plan views by aligning the cylinder parallel to the smoke-wire. Figure 6.1 shows both edge ( $x-y$  plane) and plan ( $x-z$  plane) views of the cylinder wake at  $Re = 140$ . (The two views were recorded for the same tunnel conditions, though not simultaneously.) The edge view illustrates the decay of the Karman vortex street and the subsequent growth of secondary structure. The smoke-wire was positioned at  $x/D = 8, 100$ , and  $200$  in the manner discussed previously.

For the plan view, the smoke-wire was at the same three  $x$ -positions as above, but at  $y/D = 0$  (i.e., in the center-plane of the wake), and parallel to the cylinder. In photo a) one immediately notices the skewed angle at which vortices are shed from the body. The reason for this is not entirely clear, but similar observations have been reported by many others. (See for example Tritton (1959), Gerrard (1966), Nishioka and Sato (1978).) Our own experiments indicate the slantwise shedding to be quasi-stable; i.e., vortices are sometimes shed parallel, sometimes slanted one way, and other times the opposite way. Subtle non-uniformities of the freestream, end conditions, or the body itself are the most likely candidates for triggering transitions between the three "modes." Figure 6.2 shows an unusual case where we have vortices shed slantwise at two opposing angles with an "elbow" in between.

At any rate, in Figure 6.1 the shed vortices are parallel to each other, with no appreciable spanwise structure. After the decay of the primary street however, three-dimensionality is seen in the secondary structure beyond 100 diameters (photos b and c). The honeycomb-like pattern also is skewed in these photographs; but, just as with the shed vortices, the skewness comes and goes. The size of the cells is approximately 20 cylinder diameters.

What exactly is this structure? What is the mechanism by which it develops? How, if at all, does it relate to Grant's "vortex-pair eddy?"

Figure 6.3 may provide a hint for at least the second of these questions. For  $Re = 150$ , with the smoke-wire at  $x/d = 100$ , we see the gradual formation of three-dimensional structure. By moving the smoke-wire out of the wake center-plane ( $y/d = 2$ ), we are able to visualize vortex lines from just one side of the secondary street. In this particular case, the vortices are initially straight and parallel. A waviness quickly develops, with successive vortices  $180^\circ$  out of phase. The amplitude of this perturbation grows downstream, eventually to where one vortex overlaps the next. Presumably the other side of the street has a similar experience; the interaction between the two sides may be quite complex, but it is not inconceivable that such an interaction could culminate in vortex "loops." As was suggested by Roshko (1976), long-time-averaged correlations of these loops could be interpreted as Grant's "vortex-pair eddies." Some evidence that vortex loops can exist in a wake is provided by Breidenthal (1980). A three-dimensionally-perturbed splitter plate in a shear-layer facility was used to produce the loops, which persist for large downstream distances.

For higher Reynolds numbers, where the wake becomes turbulent, smoke visualization is encumbered by small-scale structure. In Figure 6.4 however, at  $Re = 190$ , we are still able to recognize wavy structures similar to those of the laminar wake.

### 6.2. Forcing Attempts

We should point out here that Figures 6.1 and 6.3 represent exceptional cases. Only rarely is the three-dimensionality as strong as in these photographs. Nevertheless, it seems that there exists an inherent three-dimensional instability, which under proper conditions can become quite significant. We made a number of attempts at enhancing three-dimensionality; for the most part these attempts were not successful.

The first such attempt was to modify the cylinder itself. Paint was sprayed on the cylinder at regular intervals, causing periodic variation of its diameter. The hope was to generate fixed-wavelength disturbances, which would initiate orderly three-dimensional structure downstream. Unfortunately even a very small diameter perturbation ( $\approx 2\%$ ) significantly disturbs the vortex shedding mechanism, and leads to very irregular unsteady flow patterns downstream. Orderly three-dimensionality is not enhanced.

Acoustic excitation was also attempted. A loudspeaker was flush-mounted to the tunnel wall at about 150 diameters, such that the speaker axis was parallel to that of the cylinder. Theoretically, for certain frequencies of excitation, a standing wave pattern can be generated between the walls of the tunnel, thereby imposing a steady fixed-wavelength disturbance on the wake. Practically, however, it is extremely difficult to generate a steady standing wave; therefore this technique was also unsuccessful at enhancing three-dimensionality.

## Chapter 7

### Discussion and Conclusions

#### 7.1. Interpretation of Streakline Patterns

We found smoke-wire flow visualization to be very effective, as well as easy-to-use, in the study of wakes of bluff bodies. We must emphasize, however, that extreme caution should be taken when interpreting streakline patterns. In particular, when the classical case of a Karman vortex street is visualized by placement of smoke-wires at several downstream locations, the confusing integration effect of streaklines becomes immediately apparent. The conclusion to be drawn from this exercise is that in an unsteady flow it is best to introduce flow tracers at not just one, but several positions in the flow. Only by studying a collage of photographs arranged in the manner described in this paper can one be confident that he is not being misled by the integration effect of streaklines.

#### 7.2. Decay of the Karman Vortex Street

It has been shown, with flow visualization as well as with hot-wire measurements, that the Karman vortex street shed in the wake of a circular cylinder does not persist indefinitely, but rather decays exponentially with downstream distance. In the present experiments, the decay is so rapid that fluctuating velocity measurements at the Karman frequency are lost in background "noise" by 100 to 150 diameters at  $Re = 150$ . The decay is even faster for turbulent wakes where small-scale structure is prevalent.

Such rapid decay is by no means a new revelation; however its full impact has not been realized up to now because of the misinterpretation of streakline flow visualization, as discussed in Chapter 3. Reasons for the decay are certainly a)

viscosity, and b) de-amplification in the sense of hydrodynamic stability. In our numerical streakline simulations only the first of these, i.e. viscosity, is included. The decay rate inferred from Figure 3.2 is not as rapid as that for the experimental case of Figure 3.1; this shows that viscosity is not the only mechanism of decay. Desruelle (1983) shows evidence that the second mechanism, hydrodynamic de-amplification, accounts for at most 77% of the vortex street decay rate. Other possibilities contributing to the decay include c) cancellation of vorticity from opposite sides of the street, and d) the Karman vortices may be located differently with respect to the centerline than a regular eigenfunction. This final point was suggested by Desruelle, where he shows that as  $\delta$  increases with  $x$ , the lateral spacing  $b$  between Karman vortices does not "keep up;" Karman vortices that initially sit on the edge of the wake move closer to its center as the wake grows. More detailed studies of this phenomenon and its effect on the decay of a vortex street have not been attempted to date.

### 7.3. Downstream Structure

As the wake widens with downstream distance, the scale of large structures must also increase. The mechanism by which this is accomplished is hydrodynamic instability of the developing mean wake profile. Frequencies are selectively amplified and then damped, according to the local growth rates, as determined by the local mean wake profile. Observed prominent frequencies agree fairly well with predictions of parallel inviscid linear stability theory, provided that streamwise growth of the wake is taken into account.

The distribution of frequencies which are prominent broadens with downstream distance. The structure appears as groups of several vortices, separated by regions of random fluctuations; the frequency (or scale) of vortices within a group is constant, while it can vary considerably from group to group. Such a pattern agrees intuitively with what one expects in a hydrodynamically unstable



system. As a disturbance grows it convects downstream until it is no longer amplified, but damped. Meanwhile, in a somewhat random fashion, disturbances at other frequencies are amplified, perhaps originating at different  $x$ -positions, and go through similar life-cycles.

The above scenario is appropriate for turbulent as well as laminar wakes. In the turbulent case, additional complications arise because of small-scale turbulent structure. Townsend (1966) proposes his equilibrium hypothesis as a mechanism for the growth-decay cycles of large structures. Namely, large eddies develop during a period of quiescence, when the turbulence intensity is low. The large eddies grow in strength and cause rapid entrainment, which leads to an increase of turbulent intensity at all scales. Turbulent motion of smaller scales resists the growth of large eddies by absorbing some of their energy. The large eddies therefore decay, and another period of quiescence begins. Further downstream, where the wake is wider, larger-scale (lower-frequency) structure emerges, and the cycle recurs. Our results are not inconsistent with Townsend's equilibrium hypothesis. We stress *in addition* the important role of local hydrodynamic stability in the growth and decay of large structures.

Let us now address the phenomenon of vortex amalgamation. As discussed in the introduction, there seems to be some dispute as to the role of vortex pairing in the changeover to larger-scale structure in wakes. There are those who argue that pairing instability is paramount in this changeover. It is our contention however that vortex amalgamation is not necessary for the growth of larger structure; but rather, hydrodynamic instability of the developing mean velocity profile results in the selective amplification of frequencies which are locally unstable. If amalgamation does occur it is purely incidental, not the driving mechanism of the flow. Wakes of porous flat plates are particularly supportive of this statement. Wake instability alone establishes a street-like structure

downstream - no shed vortices even exist.

Nevertheless, we do observe the subharmonic  $f_k/2$  to be a popular frequency in the data, particularly at  $125 < x/d < 250$  for the cylinder wake at  $Re = 140$ . At  $x/d \approx 100$ , the primary (Karman) street has not completely decayed; it is likely that disturbances at the subharmonic  $f_k/2$  are present because of the residual Karman vortices. If such is the case, these disturbances have a "head-start" at being amplified when compared to those at frequencies not close to  $f_k/2$ . Thus  $f_k/2$  disturbances may be chosen to be amplified, even though they are not necessarily the maximally-amplified disturbances predicted by stability theory. The residual Karman vortices will pair, not due to a pairing instability in and of itself, but merely in response to the growing subharmonic disturbance. For the most part, the frequency of downstream fluctuations shifts gradually, particularly for turbulent wakes. At  $Re = 500$ , for example, no identifiable trends exist that would indicate amalgamation.

Indeed, except perhaps for the special case of  $Re = 140$ , vortex pairing was not observed by this experimenter. At  $Re = 150$  or  $500$ , for example, there is nothing outstanding about the subharmonic frequency. That is to say, disturbances at the subharmonic experience the same kind of growth and decay as at any other nearby frequency.

A plot of  $a_2/a_1$  (ratio of secondary-street scale to that of the primary street) versus Reynolds number, as shown for example by Matsui and Okude (1980), has a great amount of scatter, particularly among different flow facilities. Furthermore,  $a_2/a_1$  is exactly equal to two only for isolated cases. Hydrodynamic stability theory adequately explains the scatter. As indicated by Figure 5.13, the wake at a given location is unstable to a broad band of frequencies. If there exist relatively large background disturbances at specific frequencies within this band, these will most likely be the ones selected to amplify. It is then

clear why such facility-dependency exists. Moreover, because a broad band of scales are amplified in the wake, and because the band of amplified frequencies shifts to the left with  $x$ ,  $\alpha_2$  can not be defined unambiguously; a plot of  $\alpha_2/\alpha_1$  is thus meaningless, perhaps even misleading.

#### 7.4. Three-Dimensionality

The far-wake structure behind a two-dimensional cylinder appears to be three-dimensional. Our flow-visualization experiments reveal that three-dimensionality begins around 100 diameters, where secondary vortices exhibit a waviness which amplifies downstream. Waviness of vortex lines in the  $x-z$  plane has been observed previously by other investigators. Hama (1957) and Tritton (1959) are two of the earliest reporters of this phenomenon. More recently Gerrard (1978) and Slaouti and Gerrard (1981) investigated the influence of flow non-uniformities and end effects on vortex lines. Recent numerical work by Robinson (1984) indicates that a vortex street can be more unstable to three-dimensional disturbances than to two-dimensional disturbances over a significant range of street spacing ratios. Hama (1963) described how a vortex filament can be distorted three-dimensionally and progressively by its own induction. This mechanism, along with influences from other vortices on either side of the street, is postulated here for our observed progressive three-dimensionality.

Although the evidence is not conclusive, we may speculate that such distortions eventually lead to "pinching off" of vortices from either side of the wake to form loops. As pointed out by Roshko (1976), loops of this kind, when averaged for a long time, may explain Grant's "vortex-pair eddy" which has puzzled us for so many years.

## Appendix A

### Numerical Streaklines

#### A.1. Procedure

Following Hama (1982), Euler's method is used to calculate streaklines generated in a given velocity field. Particles are released from a fixed point at each time-step  $\Delta t$ . The position of each particle is advanced every time-step, according to

$$\mathbf{x}(t+\Delta t) = \mathbf{x}(t) + \frac{d\mathbf{x}(t)}{dt}(\Delta t) + \frac{1}{2!} \frac{d^2\mathbf{x}(t)}{dt^2}(\Delta t)^2 + \dots \quad (\text{A.1})$$

In the computer code Equation (A.1) is calculated to second order for every particle at each time-step. Connecting a string of these particles together (all of which had been introduced from the same point) constitutes a streakline.

#### A.2. Viscously-Decaying Vortex Street

The two-dimensional velocity field used for the numerical simulation in Chapter 3 is described here. Following Lamb (1945), the inviscid velocity field of an infinite row of vortices, each with strength  $\Gamma$ , and coordinates  $(0,0)$ ,  $(\pm a,0)$ ,  $(\pm 2a,0)$  ... is

$$u = \frac{-\Gamma}{2a} \frac{\sinh\left(\frac{2\pi y}{a}\right)}{\cosh\left(\frac{2\pi y}{a}\right) - \cos\left(\frac{2\pi x}{a}\right)} \quad (\text{A.2})$$

$$v = \frac{\Gamma}{2a} \frac{\sin\left(\frac{2\pi x}{a}\right)}{\cosh\left(\frac{2\pi y}{a}\right) - \cos\left(\frac{2\pi x}{a}\right)}. \quad (\text{A.3})$$

To model a Karman vortex street two such rows are superposed. One of the rows has its vortex centers midway between those of the other row, with the circulation equal but opposite; the two rows are separated by distance  $b$  in the  $y$ -direction. Such a configuration has a self-induced velocity in the negative  $x$ -direction,

$$U_i = \frac{\Gamma}{2a} \tanh\left(\frac{\pi b}{a}\right). \quad (\text{A.4})$$

Adding a constant freestream velocity to the array of vortices completes the inviscid model; each vortex convects downstream with velocity  $U_c = U_\infty - U_i$ .

To add the effects of viscosity, the vortices are allowed to diffuse as their lifetimes increase. Each shed vortex is assumed to be axisymmetric about its center and viscously decaying, with its induced tangential velocity given by

$$u_\theta = \frac{\Gamma}{2\pi r} \left(1 - e^{-\frac{r^2}{4\nu t}}\right) \quad (\text{A.5})$$

where  $r$  is the distance from the center,  $\Gamma$  is the circulation or strength of the vortex, and  $\nu$  is the kinematic viscosity of the fluid medium. At time  $t = 0$  Equation (A.5) reduces to that of an inviscid axisymmetric vortex. As time increases, the vorticity spreads out (diffuses) in such a manner that total circulation remains constant. Far enough away, the induced velocity of this vortex is

no different than that for an inviscid rectilinear vortex. Thus, to model viscosity, the inviscid vortices of the idealized Karman street are replaced by Equation (A.5) near regions of interest, i.e., close to the expanding core of the vortex. Time  $t$  is chosen as the "lifetime" of the vortex; in the computer code  $t = x/U_c$  where  $x$  is the downstream distance the vortex has travelled and  $U_c$  is its convection speed. Vortices are thus "born" periodically at  $x = 0$ , and are convected downstream to form the Karman vortex street pattern.

It should be kept in mind that the above model is not an exact solution of the equations of motion, but as discussed by Hooker (1936), it is nevertheless a very reasonable model. The constants in Equation (A.5) were chosen to simulate the flow represented by Figure 3.1. In dimensionless variables Equation (A.5) becomes

$$u_\theta^* = \frac{\Gamma^*}{2\pi r^*} \left[ 1 - e^{-\frac{(r^*)^2 \text{Re}}{4t^*}} \right] \quad (\text{A.6})$$

where

$$u_\theta^* = \frac{u_\theta}{U_\infty}, \quad t^* = \frac{(x/d)}{U_c/U_\infty},$$

$$r^* = r/d, \quad \Gamma^* = \frac{\Gamma}{U_\infty d},$$

$$\text{Re} = \frac{U_\infty d}{\nu}.$$

For the calculations shown in Figure 3.2,  $\Gamma^* = 1.4$ , (an experimental result of

Matsui & Okude (1981)),  $Re = 90$ ,  $a/d = 6$ , and  $b/d = 1.69$ . The latter two values are close to those measured in Figure 3.1. Based on experimental results of Hooker (1936), each vortex is given an "apparent age" at  $x = 0$  of  $t^* = 2$ .

## Appendix B

### Cross-Wire Wake Surveys

#### B.1. Cross-Wire Calibration Procedure

A pitot-static tube and electronic manometer were used to calibrate cross-wire voltages against tunnel velocity, immediately prior to each run. This was done by simultaneously recording the voltage from each wire along with manometer output - the cross-wire probe and pitot-static tube being positioned near each other and in the freestream of the tunnel. thirty-two two-second averages were recorded as the tunnel velocity was varied. (The hot-wire voltages were first conditioned to lie within the range 0 to 10 volts, so as to use the full range of the A/D converter.) The voltage from each wire was then plotted against velocity normal to that wire. A typical calibration (fitted to a fourth-order polynomial) is shown in Figure B.1. This calibration curve was subsequently used to calculate the instantaneous  $u$  and  $v$  velocities for each sample in the wake survey.

#### B.2. Wake Surveys

Because of the large ( $\approx 550$ ) length-to-diameter ratio of the wires, hot-wire end effects were neglected, in accord with the experimental conclusions of Champagne, Sleicher, and Wehrmann (1967). Thus, a simple trigonometric decomposition (the "cosine law") was used to obtain  $u$  and  $v$  for each cross-wire sample; i.e.,

$$u = (u_{+45^\circ} + u_{-45^\circ})\cos 45^\circ, \quad (B.1)$$



$$v = (u_{+45^\circ} - u_{-45^\circ})\cos 45^\circ . \quad (B.2)$$

where  $u_{+45^\circ}$  and  $u_{-45^\circ}$  are the velocity components normal to the  $+$  and  $-45^\circ$  wires, respectively, as defined in Figure B.2.  $u$  and  $v$  are the instantaneous velocities which we now write in terms of mean and fluctuating components,

$$u = U + u' , \quad (B.3)$$

$$v = V + v' , \quad (B.4)$$

For the case of circular cylinder wakes at  $Re = 150$  and  $500$ , the specifics of the wake surveys are as follows: The cylinder diameter was  $0.16$  cm; Reynolds numbers of  $150$  and  $500$  were obtained with freestream velocities of  $1.52$  and  $4.97$  m/s respectively. Twelve  $x$ -locations were chosen, namely  $x/d = 25, 50, 75, 100, 125, 150, 200, 250, 300, 400, 500$  and  $750$ . At each of these, data were recorded at thirty-two  $y$ -positions (the spacing in the  $y$ -direction was adjusted according to the local width of the wake). The sampling rate was  $2000$  Hz for each of the two wires; the total number of samples per wire at each position in the wake was  $8192$ . Thus, the total sampling time at each position was slightly more than four seconds.

The same cylinder was used for the data at  $Re = 140$ , at a freestream velocity of  $1.38$  m/s. The  $x$ -locations chosen for the survey were more compact than those above;  $x/d = 40, 50, 60, 75, 100, 125, 150, 175, 200, 250, 300$ , and  $350$ . The porous plate chosen for detailed cross-wire surveys was a  $47\%$  solidity screen of width  $d = 1.78$  cm, whose wire diameter and mesh size were  $0.43$  and  $1.59$  mm respectively. Surveys were made at  $x/d = 1, 2, 4, 7, 10, 15, 20, 25, 30, 40$ , and  $50$ .

Two channels of data were recorded simultaneously - the voltage output from the  $+45^\circ$  and  $-45^\circ$  wires. The calibration curve, an example of which is shown in Figure B.1, was used to calculate  $u_{+45^\circ}$  and  $u_{-45^\circ}$ ; Equations (B.1) and (B.2) provide  $u$  and  $v$ , which we could average over the entire record to obtain  $U$  and  $V$ . The fluctuating velocity components  $u'$  and  $v'$  are then derived from Equations (B.3) and (B.4). Figures B.3 - B.5 show  $U$  profiles for various downstream positions in a cylinder wake at  $Re = 140, 150$ , and  $500$  respectively.

### B.3. Analysis of the Data

Let us consider the wake survey for a circular cylinder wake at  $Re = 150$ . Having recorded  $u$  and  $v$  for each sample, there are many ways to analyze the data. Firstly the mean velocity  $U$  is normalized in the usual manner:

$$U^* = \frac{U - U_\infty}{U_0 - U_\infty} = e^{-(\ln 2) y^{*2}}, \quad (\text{B.5})$$

where  $U_0$  is the centerline velocity,  $U_\infty$  is the freestream velocity, and  $y^*$  is the normalized transverse coordinate,

$$y^* = \frac{y - y_0}{\delta}. \quad (\text{B.6})$$

In Equation (B.5), the constant  $\ln 2$  was chosen such that  $U^* = \frac{1}{2}$  at  $y^* = 1$  or  $-1$ .  $\delta$  is the wake half-width;  $y_0$  is the transverse distance corresponding to the centerline of the wake.  $U_0$ ,  $\delta$ , and  $y_0$  were chosen to give the best (least-squares) fit to Equation (B.5). Figure 5.14 shows an example of how well the data collapse onto this Gaussian wake profile. The wake half-width  $\delta$  is an important quantity which is used to normalize frequency  $f$ :

$$\beta = \frac{2\pi\delta f}{U_{\infty}} \quad (B.7)$$

Another important quantity is the centerline velocity defect,

$$W_0 = 1 - \frac{U_0}{U_{\infty}} \quad (B.8)$$

Figures 5.15 and 5.16 provide examples of how  $\delta$  and  $W_0$  vary with downstream distance  $x/D$ .

It is not certain why such a large scatter exists in these measurements. Our conjecture is that non-uniform, unsteady boundary layer transition on the walls of the test section leads to a low-frequency oscillation of the freestream. Ideally, data should be gathered at all wake positions simultaneously to avoid any such problems; this was not possible however, since only one cross-wire was used. Hence freestream conditions could have changed during the course of a survey. Four seconds may not have been a long enough sampling period to average away these (very-low-frequency) fluctuations.

In addition, the height ( $y$ -direction) of the cross-wire was approximately the same as the cylinder diameter. Hence, close to the cylinder, where the wake width is small, we would not expect good resolution in measurements of mean velocity. For this reason, the smoothing in Figures 5.15 and 5.16 is weighted in favor of far-wake data.

In all subsequent numerical calculations in which  $\delta$  and  $W_0$  were required, smoothed values were used rather than the measured values, as shown in Figures 5.15 and 5.16. It is important to note here that power spectra, probability density functions, and other quantities based on the instantaneous fluctuations

are not affected by this smoothing.

There are several methods by which we can search for wake structure, given the time-traces of  $u'$  and  $v'$ :

a) *Time plots* - An example plot of  $v'/U_\infty$  versus sample time is shown in Figure 5.9. We have also plotted  $u'/U_\infty$  and the instantaneous Reynolds stress  $-u'v'/U_\infty$  in Figures B.6 and B.7, respectively.

b) *Amplitude spectrum* - A fast-Fourier-transform (FFT) algorithm can be used to obtain the amplitude spectrum of the signal. This gives us a quantitative description of the fluctuation magnitude as a function of frequency; an example is shown in Figure 5.1. The method of modified periodograms was used to generate power spectra, as discussed in Rabiner and Gold (1975). (Amplitude spectrum is defined as the square root of the power spectrum.) Spectra of the freestream tunnel conditions for each wake survey are shown in Figures B.8 and B.9.

c) *Probability density* - If, in the time-trace of the fluctuating velocity, there exist identifiable "groups" or "bursts" of structure, the power spectrum can be calculated for each such group individually. The most prominent frequency  $f_p$  of each group is then determined, and the results of the entire time-trace are displayed in terms of probability density of spectral peaks as a function of frequency. Probability density is a bin-independent quantity calculated as follows: frequency is divided into bins spaced apart by  $\Delta f$ . We then count the number of times  $f_p$  falls into each bin. The result is called a probability distribution, which is not independent of bin-width  $\Delta f$ . Dividing by the total area under the probability distribution curve gives the probability density, which by definition has unit area, and is therefore bin-independent. An example of such a spectral probability

density function (PDF) is given in Figure 5.10.

To identify a group, an algorithm was written to scan the data, searching for a place where peak-to-peak fluctuations remain above some velocity threshold for a longer period than some time threshold. In the code the velocity threshold  $u_t$  was chosen to be  $\sqrt{2} u'_{rms}$ , where  $u'_{rms}$  was calculated for the entire time-trace. The factor  $\sqrt{2}$  was chosen since for a sine wave  $u'_{p-p} = \sqrt{2} u'_{rms}$ . The proper time threshold to choose is somewhat less clear. If too small, the frequency resolution of the FFT would be poor; if too large, some of the shorter-lasting groups of structure would not be considered. The time threshold chosen in our calculations therefore varied with location and Reynolds number. Typically,  $t_t$  was chosen so as to allow at least two cycles of a disturbance at the minimum expected frequency.

The PDF's were weighted by the amplitude of fluctuations within a group - i.e., those groups with large-amplitude fluctuations contributed more to the PDF than groups with smaller amplitudes.

## Appendix C

### Inviscid Linear Stability Calculations

For parallel two-dimensional mean flows, with  $U=U(y)$  only, inviscid linear hydrodynamic stability theory may be applied. Basically, a small unsteady perturbation is superposed on the known steady mean solution; analysis of the resulting set of equations can predict which disturbances are likely to be amplified. Following Gaster (1965), let the perturbation stream function be given by

$$\psi(y; x, t) = \varphi(y) e^{i(\alpha x - \beta t)}, \quad (C.1)$$

where

$$u = \frac{\partial \psi}{\partial y}, \quad v = \frac{-\partial \psi}{\partial x}. \quad (C.2)$$

$\alpha$  is called the wave number, while  $\beta$  is the frequency; in the general case both  $\alpha$  and  $\beta$  may be complex. Substituting  $\psi$  and the known mean solution  $U(y)$  into the equations of motion yields the Orr-Sommerfeld equation. Neglecting viscosity, the resulting equation is the simpler Rayleigh equation,

$$(U(y) - \beta/\alpha)(\varphi'' - \alpha^2 \varphi) = 0, \quad (C.3)$$

where primes denote differentiation with respect to  $y$ .

For the present case of a far-field two-dimensional wake, an appropriate parallel mean solution is the Gaussian:

$$U(y) = U_{\infty}(1 - W_0 \xi), \quad (C.4)$$

where

$$\xi = \frac{U(y) - U_{\infty}}{U_0 - U_{\infty}} = e^{-(\ln 2)(y/\delta)^2}, \quad (C.5)$$

$$W_0 = 1 - \frac{U_0}{U_{\infty}}, \quad (C.6)$$

$\delta$  is the wake half-width,  $U_0$  is the wake centerline velocity, and the constant  $\ln 2$  is chosen so that  $\xi = \frac{1}{2}$  at  $\frac{y}{\delta} = \pm 1$ . Putting (C.4) into (C.3) results in

$$(C - \xi)(\varphi'' - \alpha^2 \varphi) + \xi'' \varphi = 0, \quad (C.7)$$

with

$$C = \frac{1}{W_0} \left[ 1 - \frac{\beta}{\alpha U_{\infty}} \right]. \quad (C.8)$$

Kubota (1983) has obtained solutions for wave speed  $C$ , given  $\alpha = \text{real}$  (temporal mode); and also for wave number  $\alpha$ , given  $\beta = \text{real}$  (spatial mode). In the latter case, spatial amplification is equal to  $-\alpha_i$ ; in Figure 5.12 we have plotted  $-\alpha_i$  vs.  $\beta$  for various values of  $W_0$ . For the temporal mode, the corresponding spatial growth rate is approximated by  $g = \alpha \beta_i / \beta_r$ , according to Gaster (1965). This growth rate as a function of  $\beta_r$  is plotted in Figure 5.13.

In Figure C.1 the calculations at  $W_0 = 0.3$  are compared with experimental results of Deruelle (1983). He measured growth (and decay) rates of acoustically-excited fluctuations in the far wakes of circular cylinders at low Reynolds numbers. Also shown on the plot are recent calculations by Hultgren (1984) for the case of *viscous* spatial linear stability of a far wake at  $W_0 = 0.3$ , and at  $Re_\delta = 70$ .  $Re_\delta$  is based on the wake half-width and velocity defect,

$$Re_\delta = \frac{W_0 U_\infty \delta}{\nu} \quad (C.9)$$

Reynolds number based on cylinder diameter  $d$  is also listed in Figure C.1 for comparison.



## 1. References

- AREF, H. and SIGGIA, E. 1981 *Evolution and breakdown of a vortex street in two dimensions*, J. Fluid Mechanics **109**, 435-463.
- BERGER, E. and WILLE, R. 1972 *Periodic flow phenomena*, Ann. Rev. Fluid Mechanics **4**, 313-340.
- BEVILAQUA, P. 1975 *Intermittency, the entrainment problem*, ARL Technical Report 75-0095, USAF.
- BREIDENTHAL, R. 1980 *Response of plane shear layers and wakes to strong three-dimensional disturbances*, Phys. Fluids **23**, 1929-1934.
- BROWN, G. and ROSHKO, A. 1974 *On density effects and large structures in turbulent mixing layers*, J. Fluid Mechanics **64**, 775-816.
- CANTWELL, B.J. 1979 *Coherent turbulent structures as critical points in unsteady flow*, Archives of Mechanics **31**, no. 5, 707-721.
- CASTRO, I. 1971 *Wake characteristics of two-dimensional perforated plates normal to an air-stream*, J. Fluid Mechanics **48**, 599-609.
- CHAMPAGNE, F., SLEICHER, C. and WEHRMANN, O. 1967 *Turbulence measurements with inclined hot-wires. Part 1. Heat transfer experiments with inclined hot-wire*, J. Fluid Mechanics **28**, 153-175.
- CIMBALA, J., NAGIB, H. and ROSHKO, A. 1981 *Wake instability leading to new large scale structures downstream of bluff bodies*, Bull. Am. Phys. Soc. **26**, no. 9, 1258.
- CORKE, T., KOGA, D., DRUBKA, R. and NAGIB H. 1977 *A new technique for introducing controlled sheets of streaklines in wind tunnels*, IEEE Publication 77-CH 1251-8 AES.
- DAVIES, M.E. 1976 *A comparison of the wake structure of a stationary and oscillating bluff body using a conditional averaging technique*, J. Fluid Mechanics **75**, 209-231.
- DESRUELLE, D. 1983 *Beyond the Karman vortex street*, M.S. Thesis, Illinois Institute of Technology, Chicago, Illinois.

DURGIN, W. and KARLSSON, S. 1971 *On the phenomenon of vortex street breakdown*, J. Fluid Mechanics **48**, no. 3, 507-527.

GASTER, M. 1965 *The role of spatially growing waves in the theory of hydrodynamic stability*, Prog. in Aero. Sciences **6**, 251-270.

GERRARD, H. 1966 *The three-dimensional structure of the wake of a circular cylinder*, J. Fluid Mechanics **25**, 143-164.

GERRARD, J. 1978 *The wakes of cylindrical bluff bodies at low Reynolds number*, Phil. Trans. Roy. Soc. London A **288**, 351-382.

GRANT, H.L. 1958 *The large eddies of turbulent motion*, J. Fluid Mechanics **4**, 149-198.

GUPTA, A., LAUFER, J. and KAPLAN, R. 1971 *Spatial structure in the viscous sub-layer*, J. Fluid Mechanics **50**, 493-512.

HAMA, F.R. 1957 *Three-dimensional vortex pattern behind a circular cylinder*, J. of Aero. Sciences **24**, 156-157.

HAMA, F.R. 1962 *Streaklines in a perturbed shear flow*, Phys. Fluids **5**, 644-650.

HAMA, F.R. 1963 *Progressive deformation of a perturbed line vortex filament*, Physics of Fluids **6**, 526-534.

HO, C.-M. and HUERRE, P. 1984 *Perturbed free shear layers*, Annual Review of Fluid Mechanics **16**, 365-424.

HOOKE, S. 1936 *On the action of viscosity in increasing the spacing ratio of a vortex street*, Proc. Roy. Soc. London **154A**, 67-89.

HULTGREN, L.S. 1984 Private Communications, Illinois Institute of Technology, Chicago, Illinois.

HUSSAIN, A.K.M.F. and RAMJEE, V. 1976 *Periodic wake behind a circular cylinder at low Reynolds numbers*, Aeronautical Quarterly **27**, 123-142.

KEFFER, J. 1965 *The uniform distortion of a turbulent wake*, J. Fluid Mechanics **22**, 135-159.

KUBOTA, T. 1983 Private Communications, California Institute of Technology, Pasadena, California.

- LAMB, H. 1945 *Hydrodynamics*, 8th edition, Dover, New York, 224-229.
- LAPPLE, C.E. 1961 *The little things in life*, Stanford Research Inst. Jour. 5, 94-102.
- LESSEN, M. and SINGH, P. J. 1974 *Stability of turbulent jets and wakes*, Phys. Fluids 17, 1329-1330.
- LOEHRKE, R. and NAGIB, H. 1972 *Experiments on management of free-stream turbulence*, AGARD Report No. 598; AD749891.
- MATTINGLY, G.E. and CRIMINALE, W.O. 1972 *The stability of an incompressible two-dimensional wake*, J. Fluid Mechanics 51, 233-272.
- MATSUI, T. and OKUDE, M. 1980 *Rearrangement of Karman vortex street at low Reynolds numbers*, XVth International Congress of Theoretical and Applied Mechanics, Univ. of Toronto, August, 1-27.
- MATSUI, T. and OKUDE, M. 1981 *Vortex pairing in a Karman vortex street*, Proceedings from the Seventh Biennial Symposium on Turbulence, Rolla, Missouri.
- MATSUI, T. and OKUDE, M. 1983 *Formation of the secondary vortex street in the wake of a circular cylinder*, in Structure of Complex Turbulent shear flow, IUTAM Symposium, Marseille, 1982, Springer-Verlag.
- MORKOVIN, M. 1964 *Flow around circular cylinder - a kaleidoscope of challenging fluid phenomena*, Proc. ASME Symposium on Fully Separated Flows, Philadelphia, 102-118.
- MUMFORD, J.C. 1983 *The structure of the large eddies in fully developed turbulent shear flows. Part 2: The plane wake*, J. Fluid Mechanics 137, 447-456.
- NAGIB, H. and DESRUELLE, D. 1982 *Controlled excitation of the far wake instability*, Bull. Am. Phys. Soc. 27, no. 9, 1193.
- NISHIOKA, M. and SATO, H. 1978 *Mechanism of determination of the shedding frequency of vortices behind a cylinder at low Reynolds numbers*, J. Fluid Mechanics 89, 49-60.
- NOSENCHUCK, D., TAYLOR, S. and ROBEY, H. 1983 Private Communications, California Institute of Technology, Pasadena, California.

PAYNE, F. and LUMLEY, J. 1967 *Large eddy structure of the turbulent wake behind a circular cylinder*, Phys. Fluids Supplement, S194-S196.

RABINER, L. and GOLD, B. 1975 *Theory and application of digital signal processing*, Prentice-Hall, Inc., New Jersey, 414-419.

ROBINSON, A. 1984 *Existence and stability of vortices and vortex arrays*, Ph.D. Thesis, California Institute of Technology, Pasadena, California.

ROSHKO, A. 1953 *On the development of turbulent wakes from vortex streets*, NACA TN 2913 (see also, NACA Rep. 1191 (1959)).

ROSHKO, A. 1976 *Structure of turbulent shear flows: a new look*, AIAA J. 14, no. 10, 1349-1357.

SAFFMAN, P. and SCHATZMAN, J. 1981 *An inviscid model for the vortex street wake*, Applied Mathematics Department, California Institute of Technology, Pasadena, California.

SCHATZMAN, J. 1981 *A model for the von Karman vortex street*, Ph.D. Thesis, California Institute of Technology, Pasadena, California.

SLAOUTI, A. and GERRARD, J. 1981 *An experimental investigation of the end effects on the wake of a circular cylinder towed through water at low Reynolds numbers*, J. Fluid Mechanics 112, 297-314.

TANEDA, S. 1959 *Downstream development of wakes behind cylinders*, J. Phys. Soc. Japan 14, no. 6, 843-848.

TOWNSEND, A.A. 1956 *The structure of turbulent shear flow*, Cambridge University Press.

TOWNSEND, A.A. 1966 *The mechanism of entrainment in free turbulent flows*, J. Fluid Mechanics 26, 689-715.

TOWNSEND, A.A. 1970 *Entrainment and the structure of turbulent flow*, J. Fluid Mechanics 41, 13-46.

TOWNSEND, A.A. 1979 *Flow patterns of large eddies in a wake and in a boundary layer*, J. Fluid Mechanics 95, 515-537.

TRITTON, D.J. 1959 *Experiments on the flow past a circular cylinder at low Reynolds numbers*, J. Fluid Mechanics 6, 547-567.

TRITTON, D.J. 1977 *Physical fluid dynamics*, International Student Edition, Van Nostrand Reinhold, New York, 23.

VALENSI, J. 1974 *On the aerodynamic of porous sheets*, in "Omaggio a Carlo Ferrari: Torino, Libreria Editrice Universitaria Levrotto & Bella."

WEIHS, D. 1973 *On the existence of multiple Karman vortex-street modes*, J. Fluid Mechanics **61**, no. 1, 199-205.

WILLIAMSON, C.H. 1983 *Evolution of a single wake behind a pair of bluff bodies normal to a stream*, University of Cambridge, (to be published).

WLEZIEN, R. 1981 *The evolution of the low-wavenumber structure in a turbulent wake*, Ph.D. Thesis, Illinois Institute of Technology, Chicago, Illinois.

WYGNANSKI, I., CHAMPAGNE, F. and MARASLI, B. 1983 *On the large scale structures in two-dimensional small deficit, turbulent wakes*, Rough Draft Manuscript, University of Arizona.

ZDRAVKOVICH, M.M. 1968 *Smoke observations of the wake of a group of three cylinders at low Reynolds number*, J. Fluid Mechanics **32**, 339-351.

ZDRAVKOVICH, M.M. 1969 *Smoke observations of the formation of a Karman vortex street*, J. Fluid Mechanics **37**, 491-496.

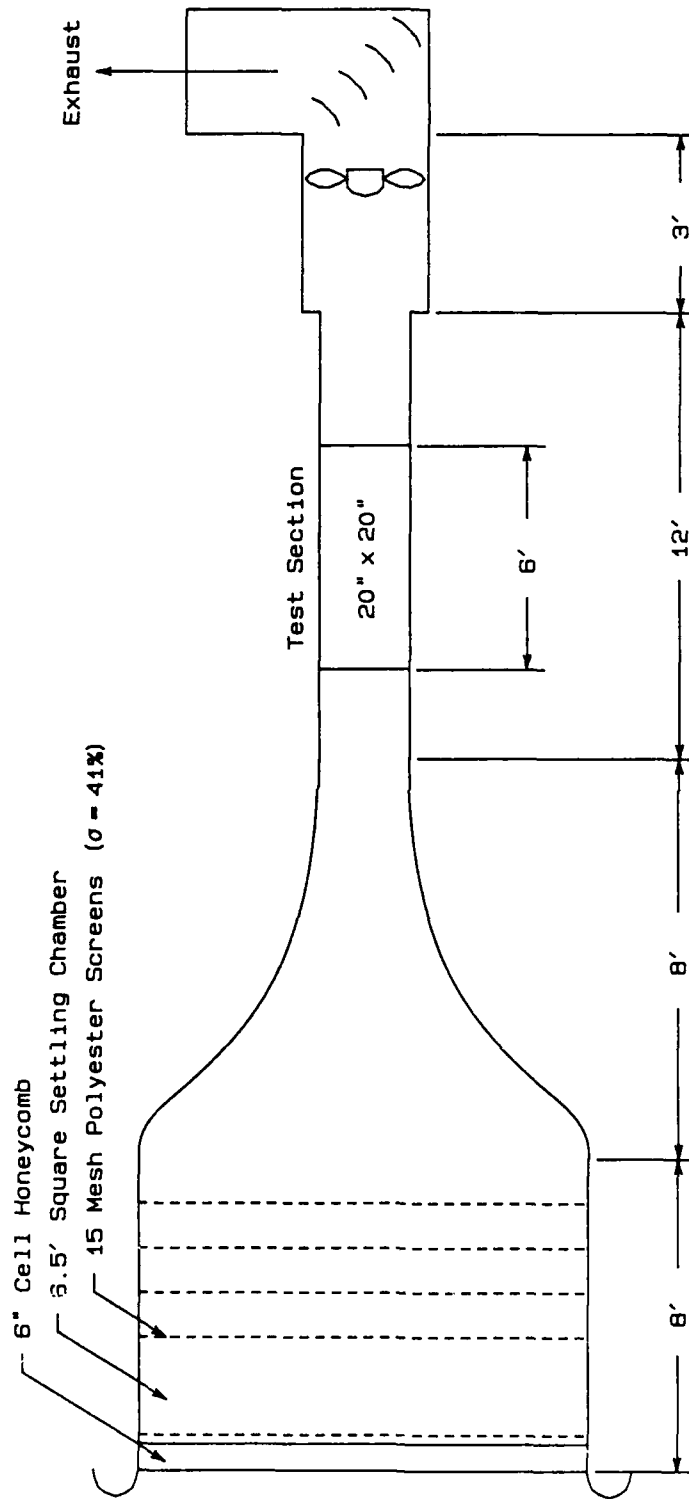


Figure 2.1: Wind tunnel facility, side view (not to scale).

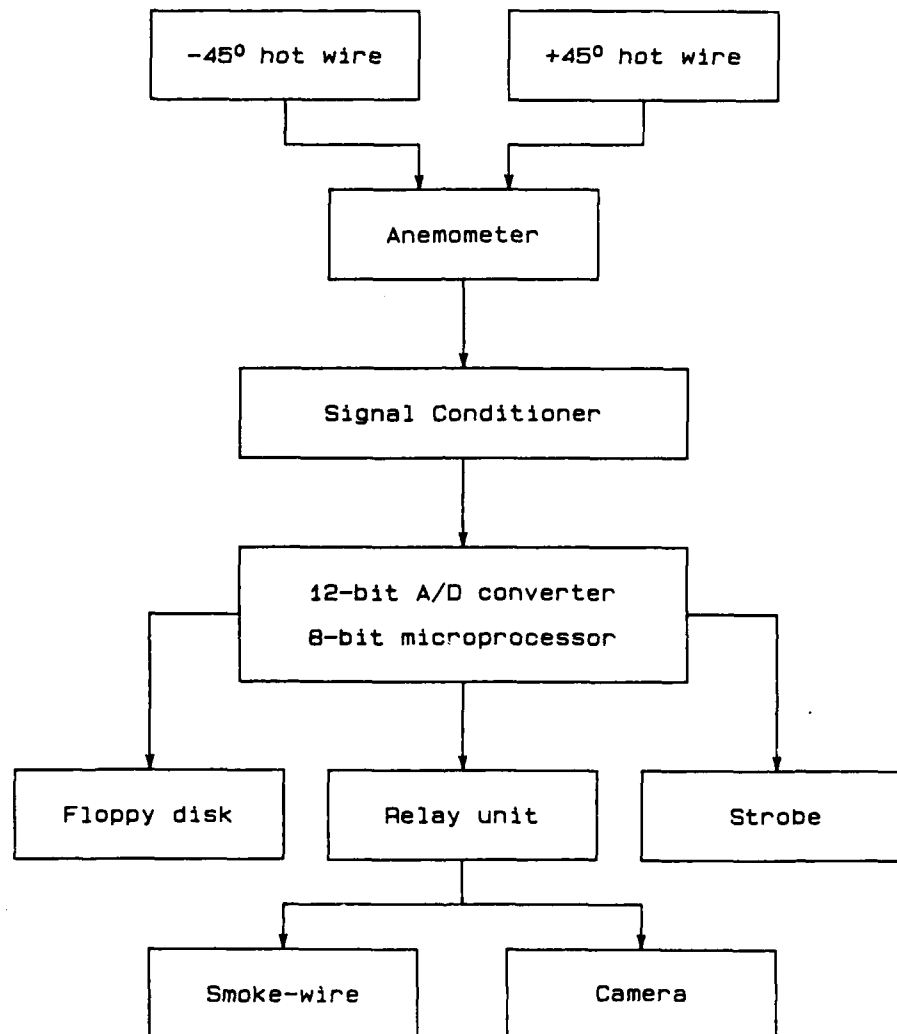


Figure 2.2: Digital data acquisition system.

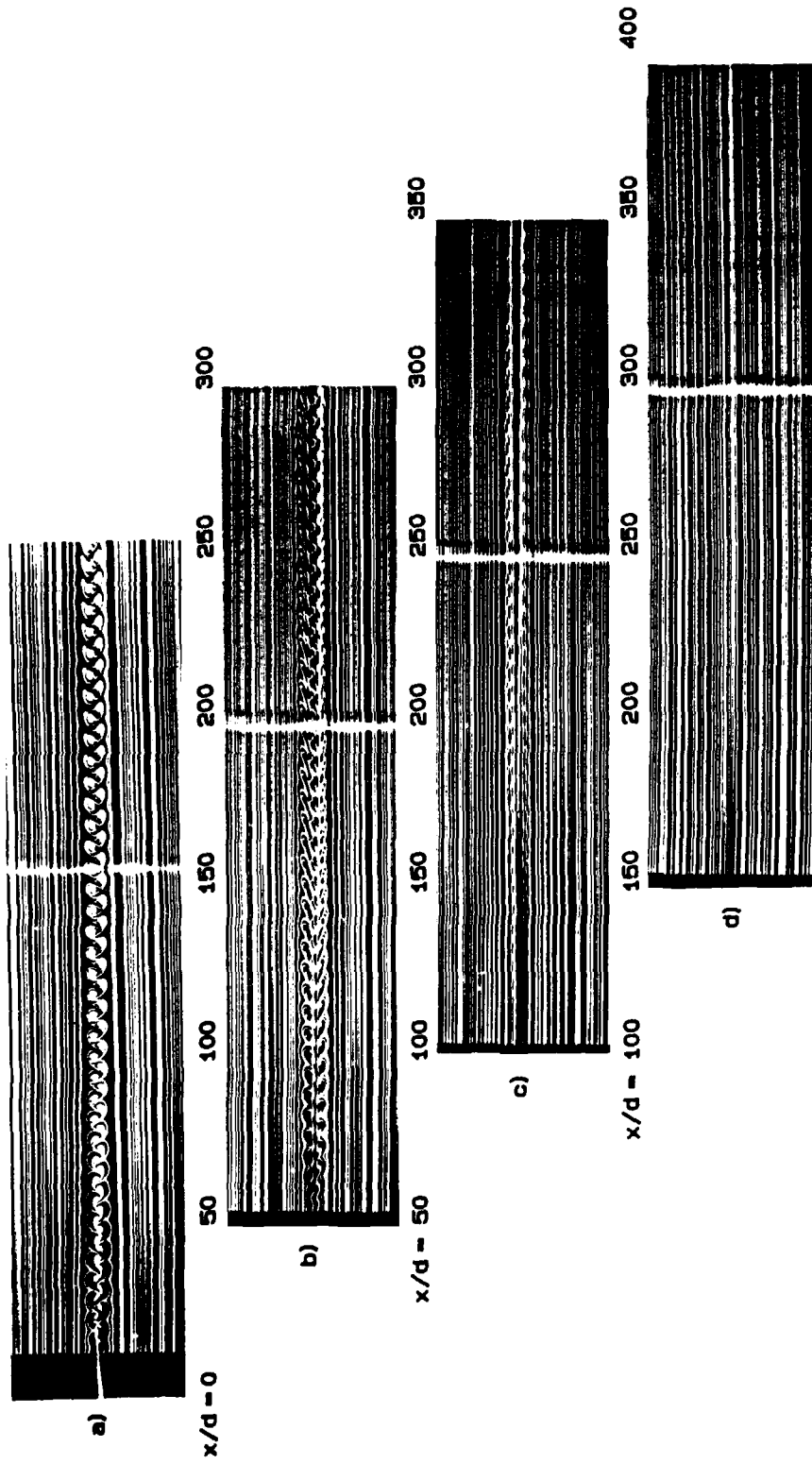
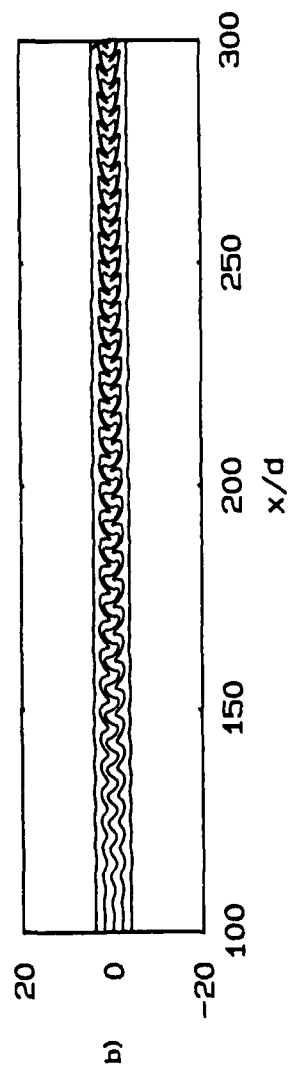
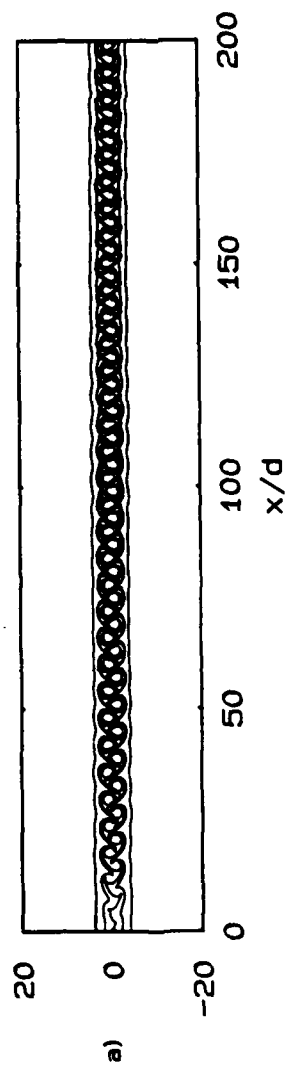


Figure 3.1: Circular cylinder wake at  $Re = 90$ : smoke-wire at  $x/d =$  a) 0, b) 50, c) 100, and d) 150.





-71-

Figure 3.2: Numerical simulation of decaying Karman vortex street.  $Re = 90$ :  
streaklines introduced at  $x/d = a)$  0, and  $b)$  100.

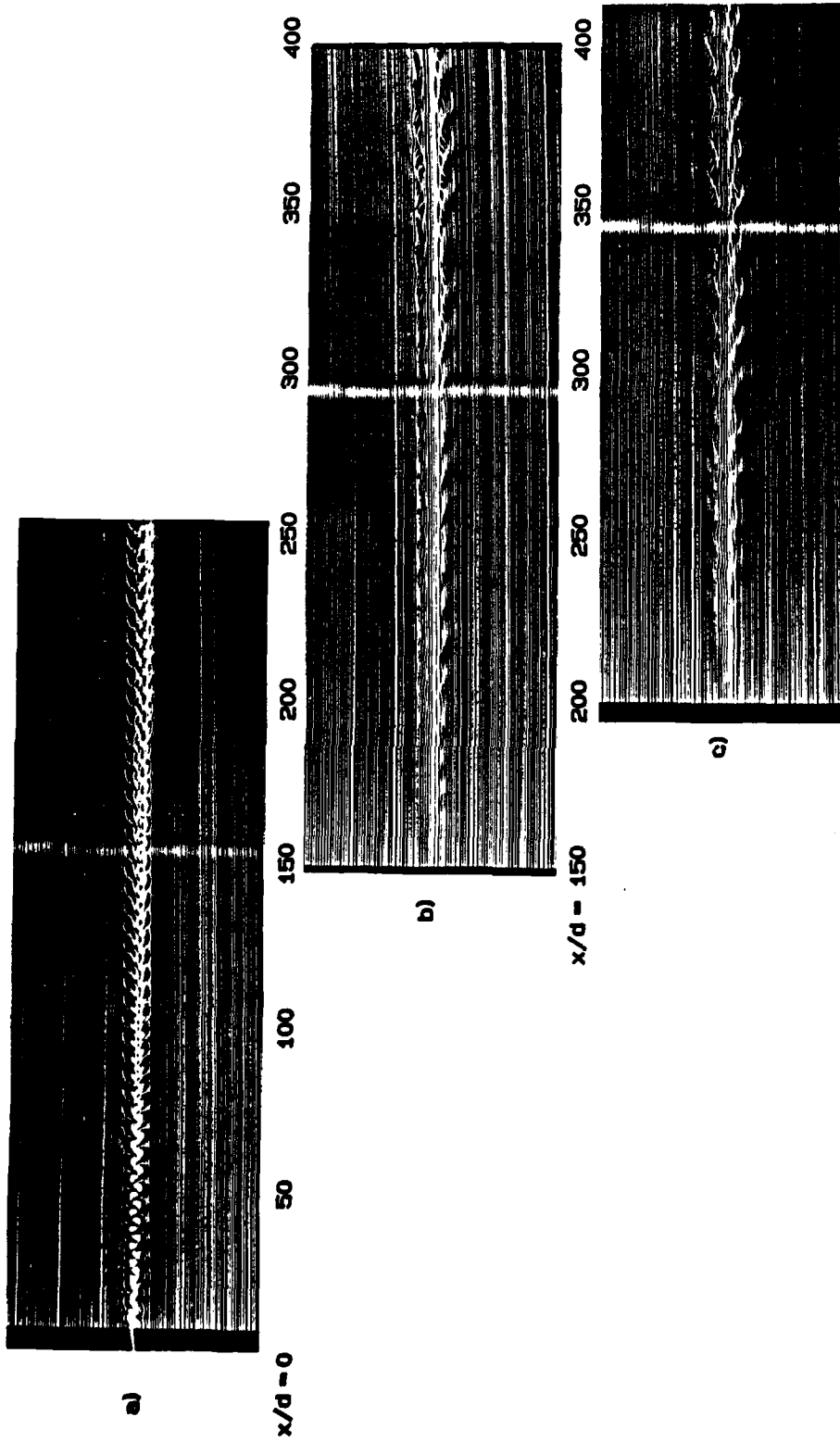


Figure 4.1: Circular cylinder wake at  $Re = 130$ ; smoke-wire at  $x/d = a)$  8, b) 150, and c) 200.

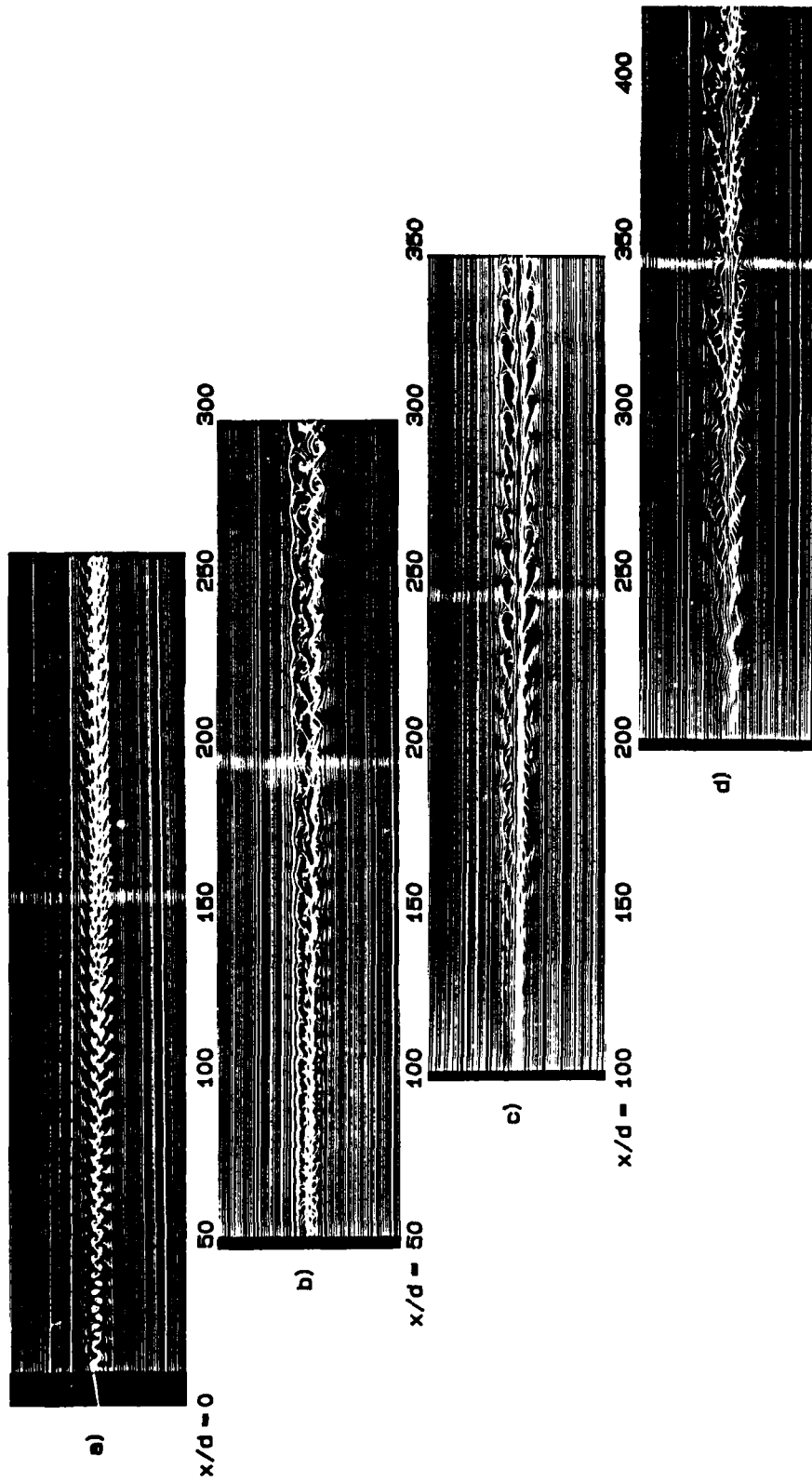


Figure 4.2: Circular cylinder wake at  $Re = 140$ : smoke-wire at  $x/d = a)$  0, b) 50, c) 100, and d) 200.

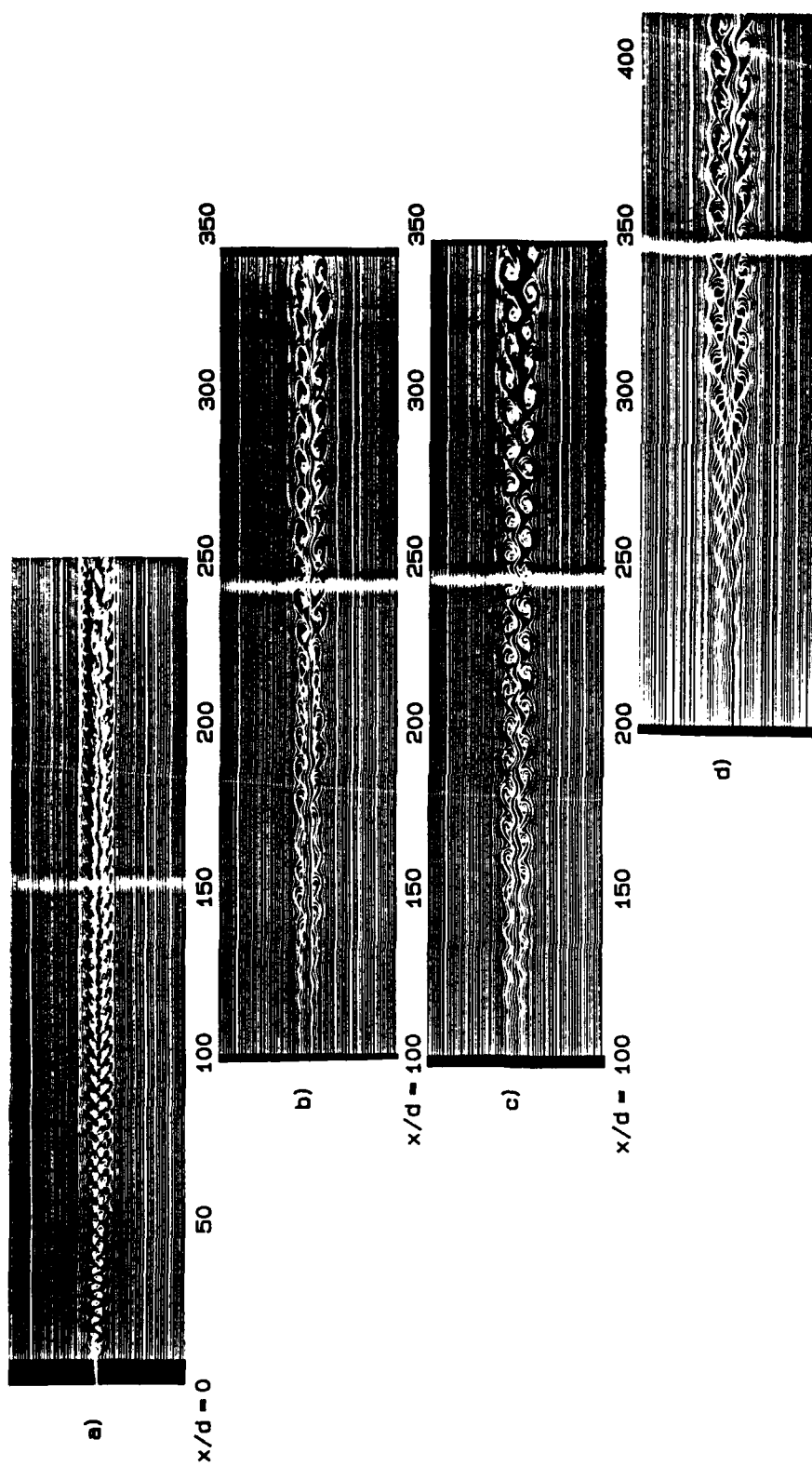


Figure 4.3: Circular cylinder wake at  $Re = 155$ ; smoke-wire at  $x/d = a)$  8, b) 100, c) 100, and d) 200.

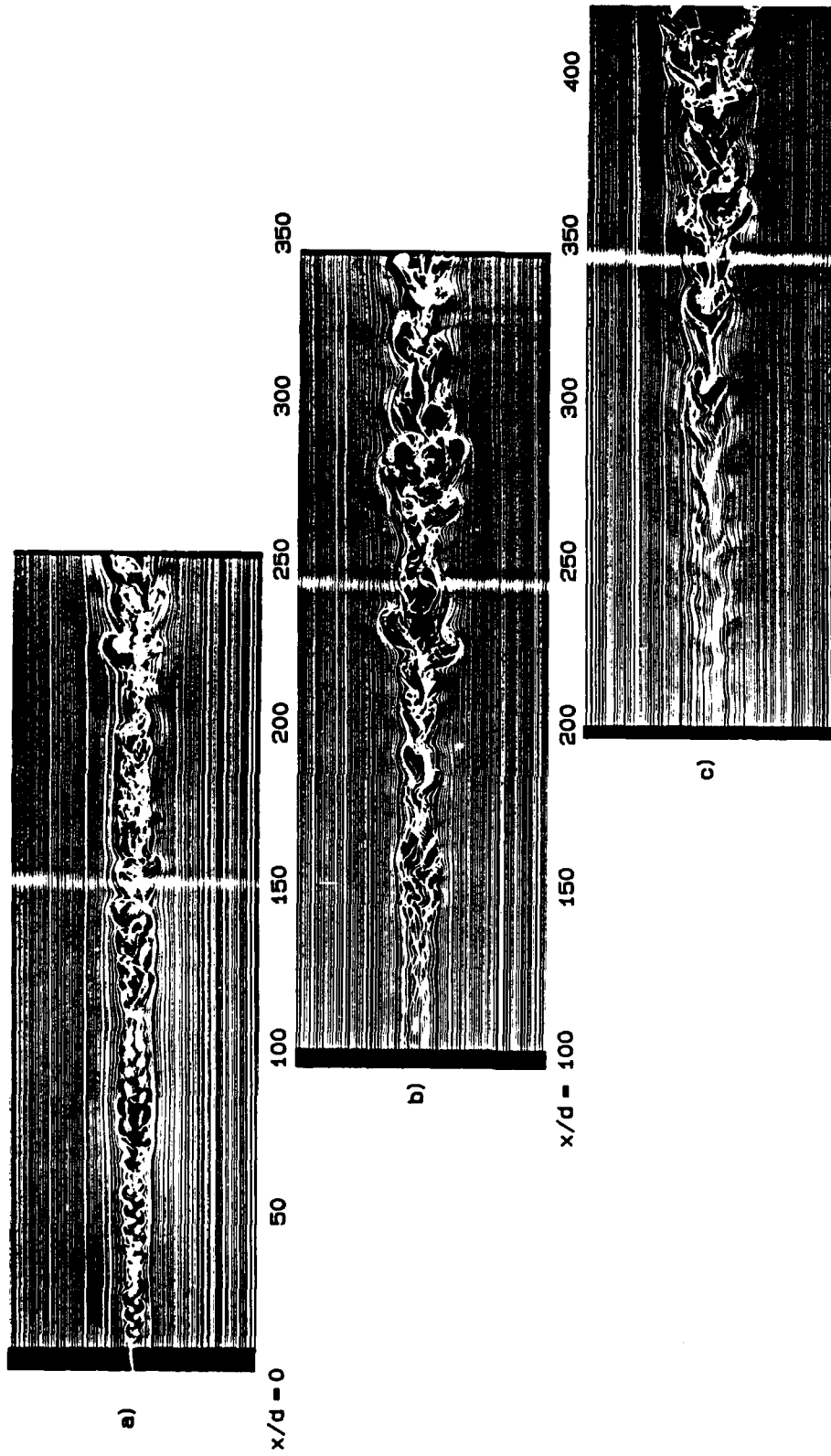


Figure 4.4: Circular cylinder wake at  $Re = 190$ ; smoke-wire at  $x/d = a)$  0,  $b)$  100, and  $c)$  200.

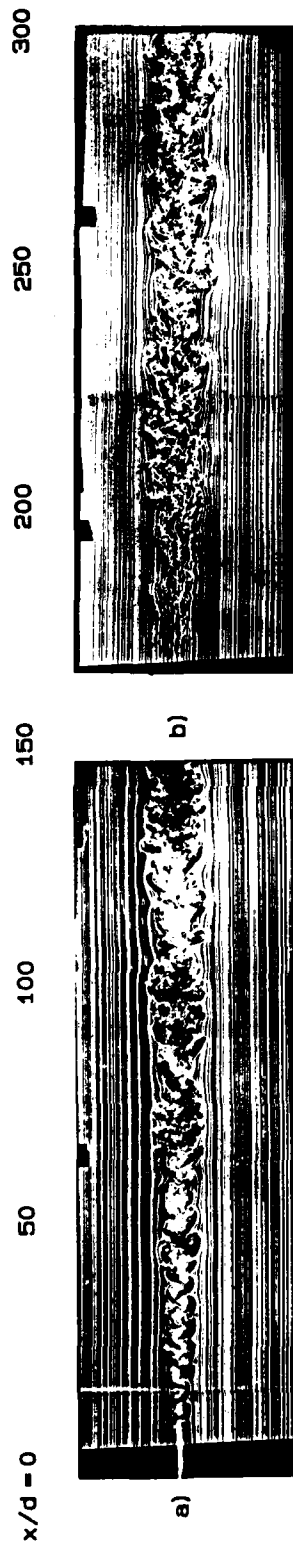


Figure 4.5: Circular cylinder wake at  $Re = 2200$ ; smoke-wire at  $x/d = a) 1$ , and b) 160.

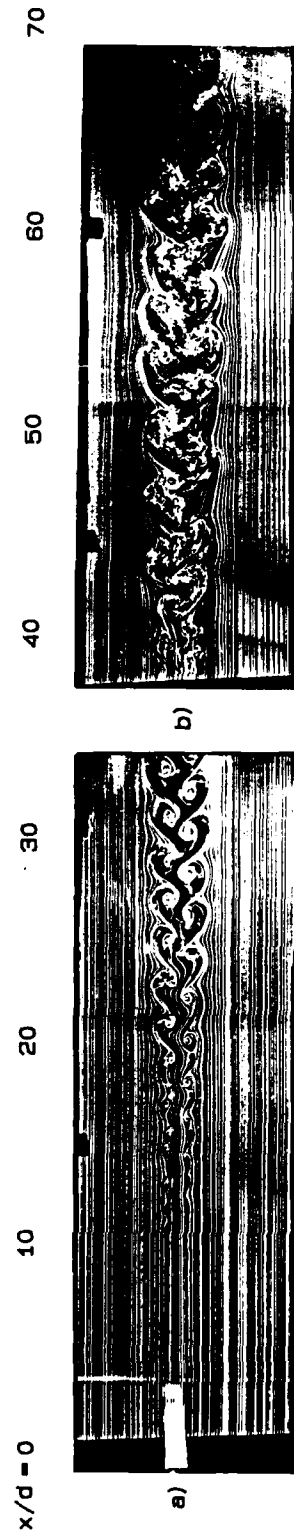


Figure 4.6: Porous flat plate wake at  $Re = 6800$ ,  $\sigma = 29\%$ ; smoke-wire at  $x/d = a) 0$ , and b) 38.

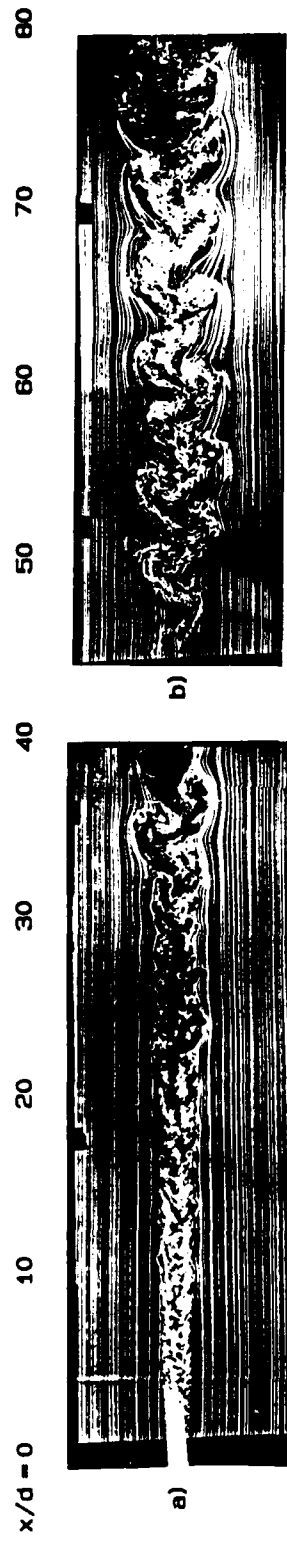


Figure 4.7: Porous flat plate wake at  $Re = 6000$ ,  $\sigma = 47\%$ ; smoke-wire at  $x/d = a) 0$ , and  $b) 44$ .



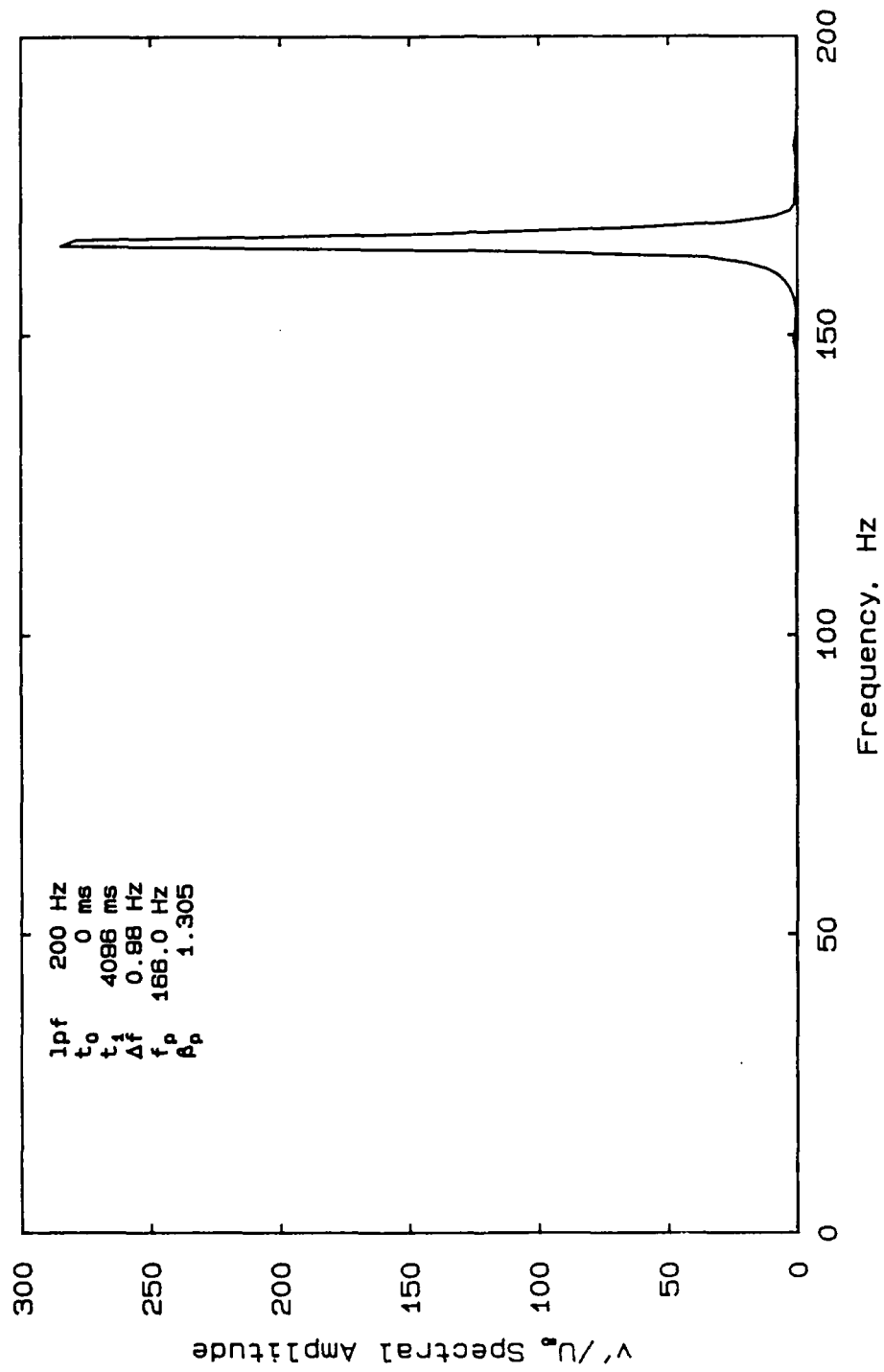


Figure 5.1: Amplitude spectrum of  $v'/U_\infty$  at inflection points of mean velocity profile; circular cylinder wake at  $Re = 150$ ,  $x/d = 25$ .

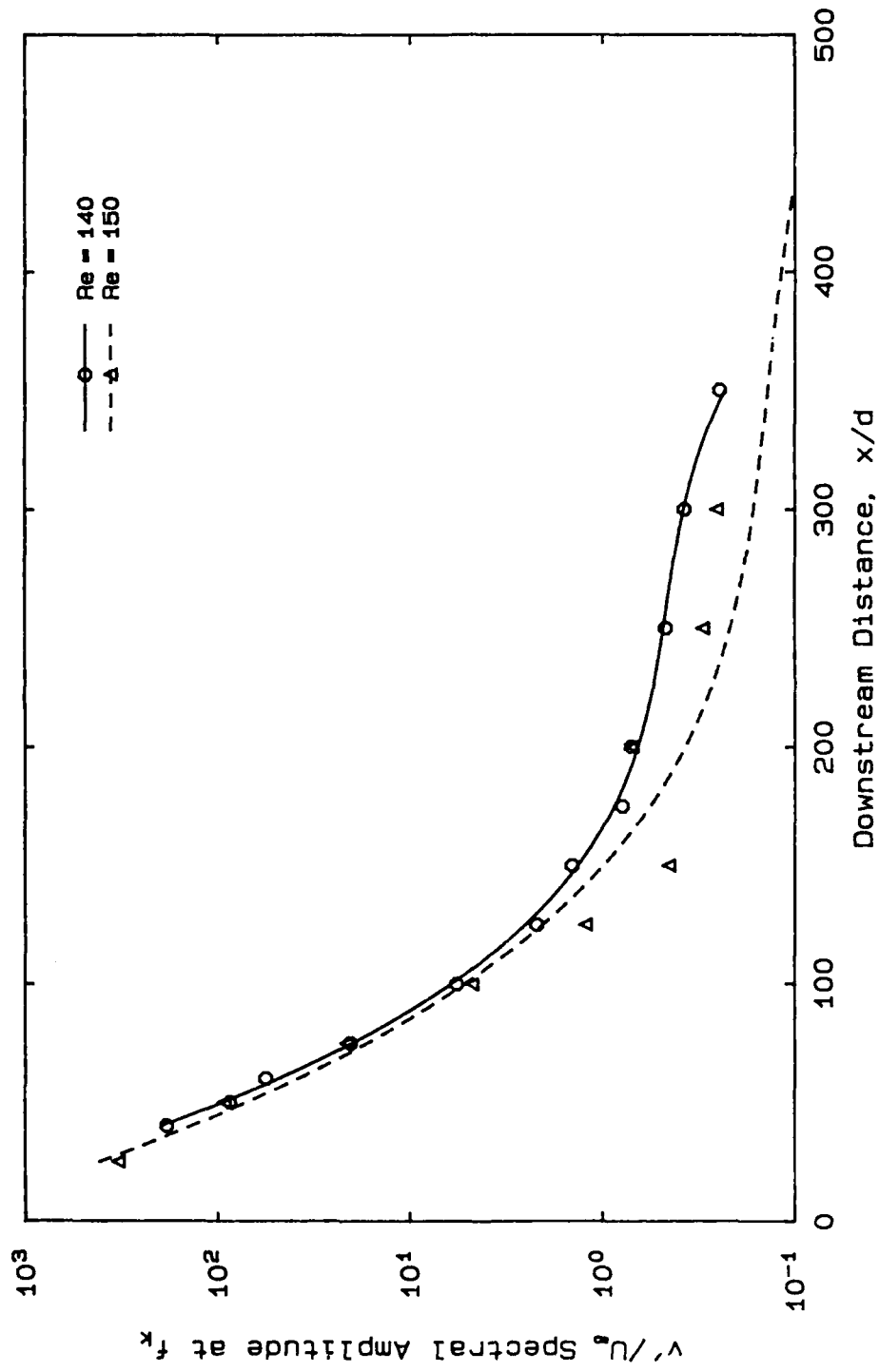


Figure 5.2: Exponential decay of Karman vortex street; circular cylinder wake at  $Re = 140$  and  $150$ .

AD-A143 642

LARGE STRUCTURE IN THE FAR WAKES OF TWO-DIMENSIONAL  
BLUFF BODIES(U) CALIFORNIA INST OF TECH PASADENA  
GRADUATE AERONAUTICAL LABS J M CIMBALA 1984

2/2

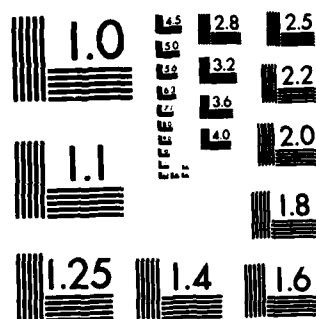
UNCLASSIFIED

N00014-76-C-0260

F/G 20/4

NL





MICROCOPY RESOLUTION TEST CHART  
NATIONAL BUREAU OF STANDARDS-1963-A

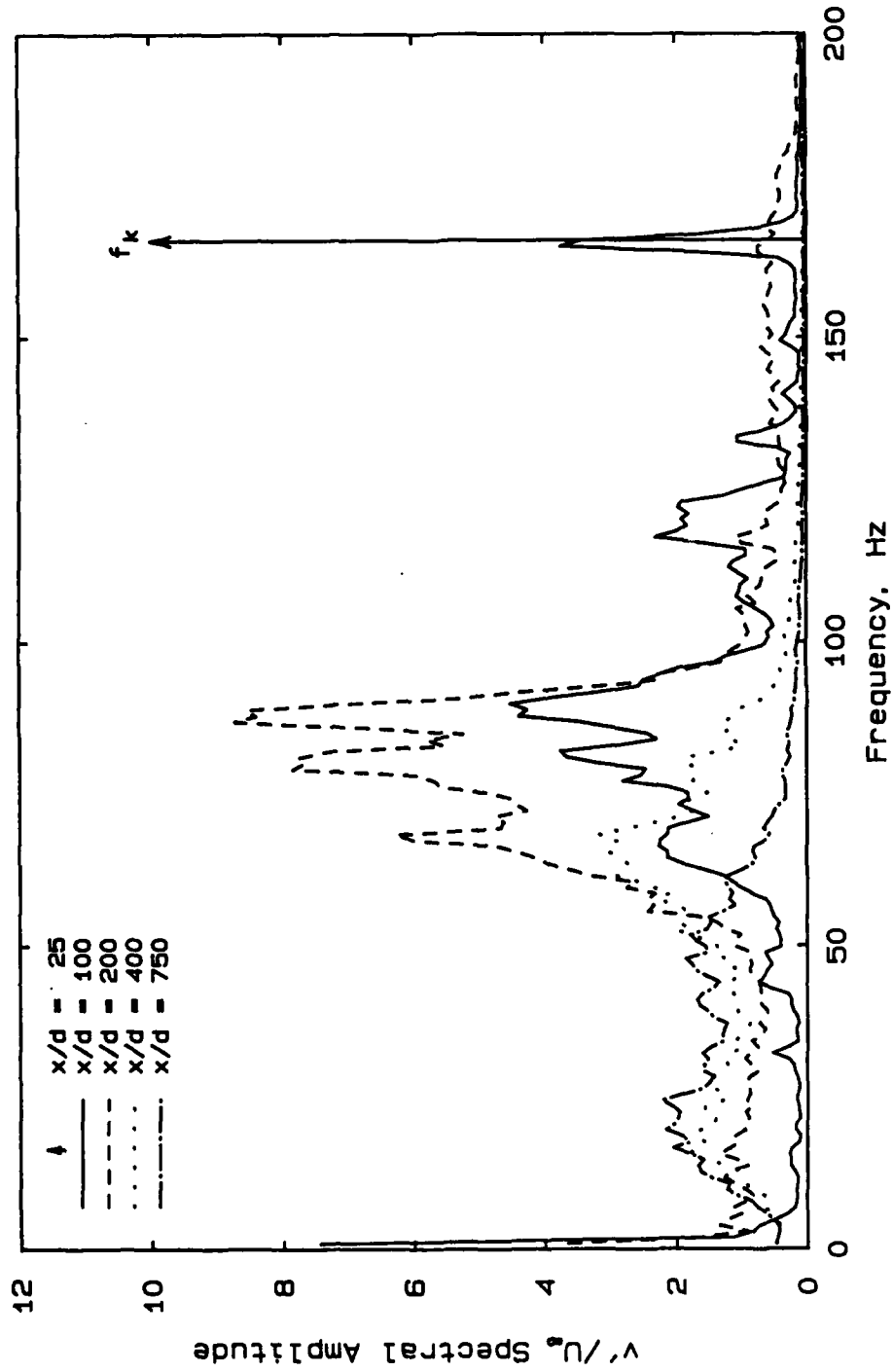


Figure 5.3: Amplitude spectra at several downstream distances;  
circular cylinder wake at  $Re = 150$ .

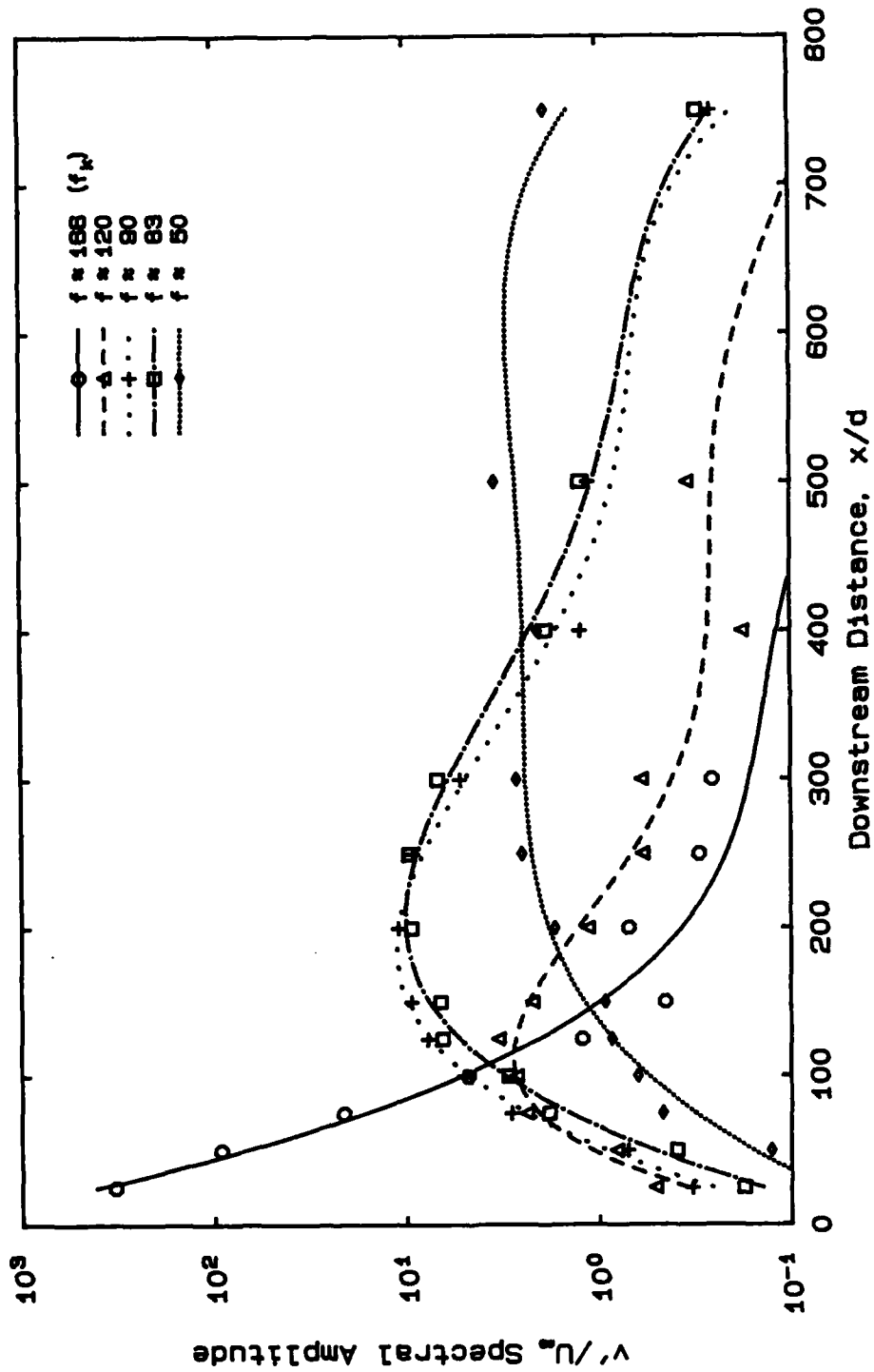


Figure 5.4: Growth-decay cycles of selected discrete frequencies: circular cylinder wake at  $Re = 150$ .

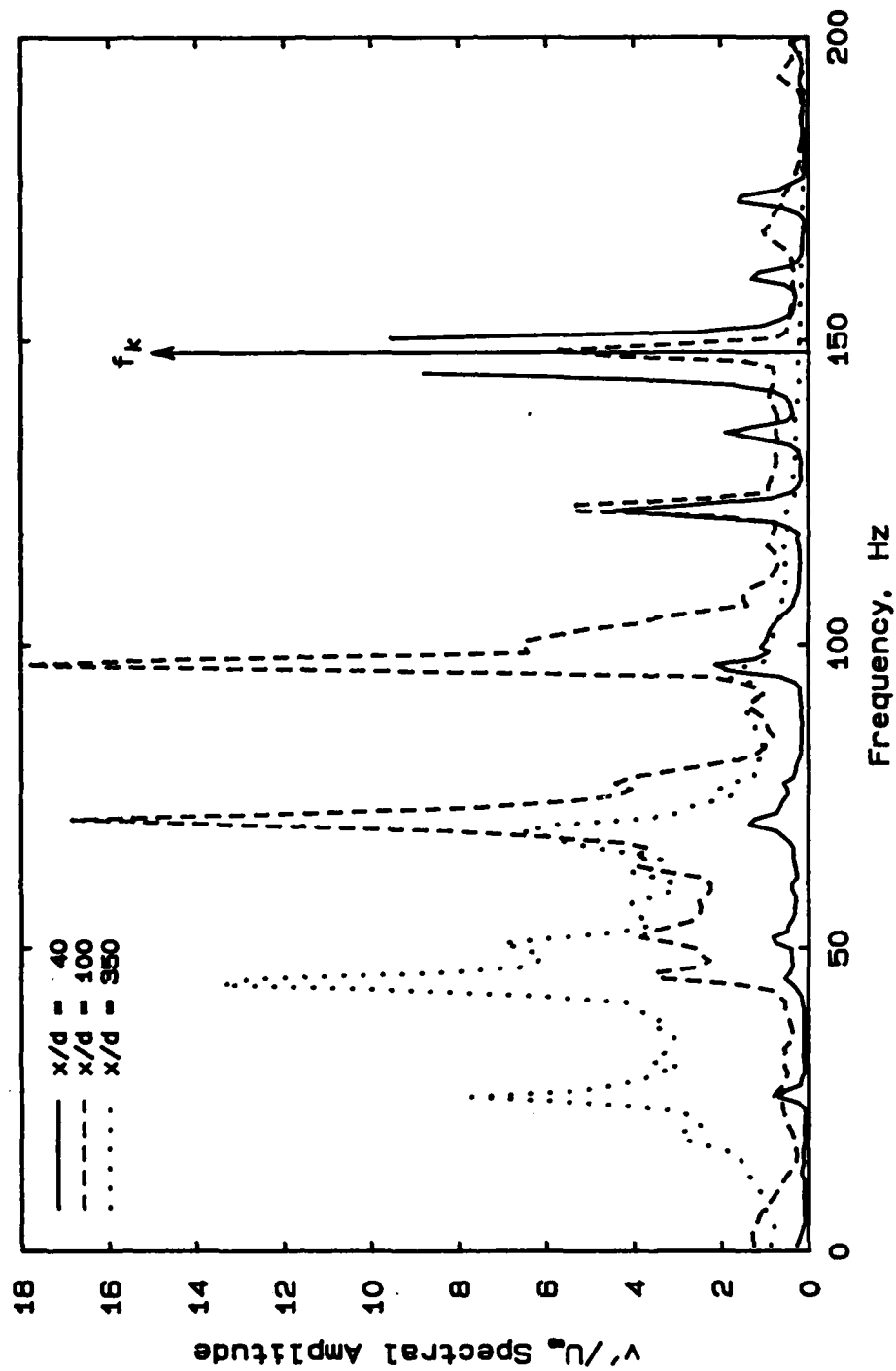


Figure 5.5: Amplitude spectra at several downstream distances:  
circular cylinder wake at  $Re = 140$ .

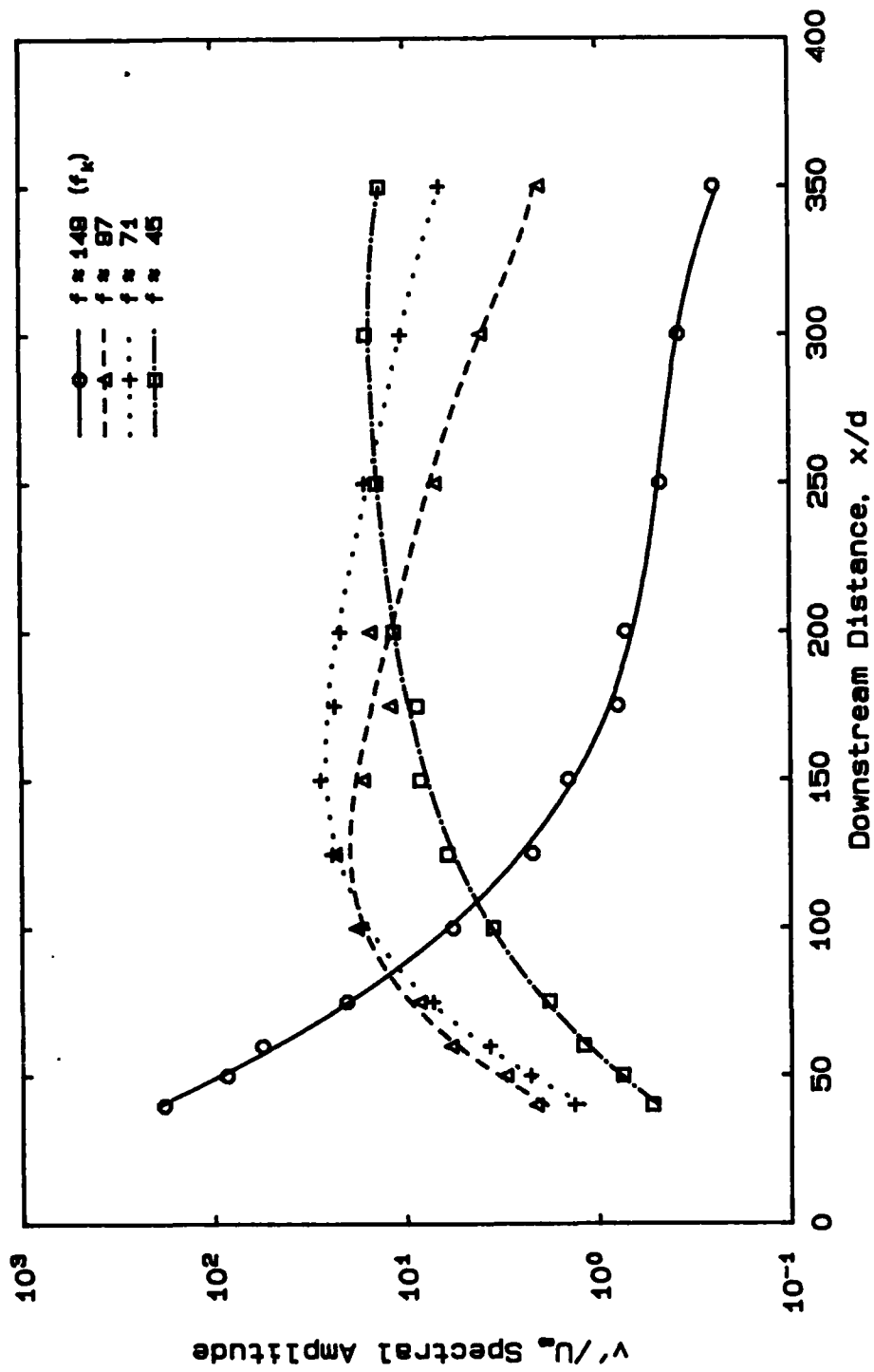


Figure 5.8: Growth-decay cycles of selected discrete frequencies: circular cylinder wake at  $Re = 140$ .



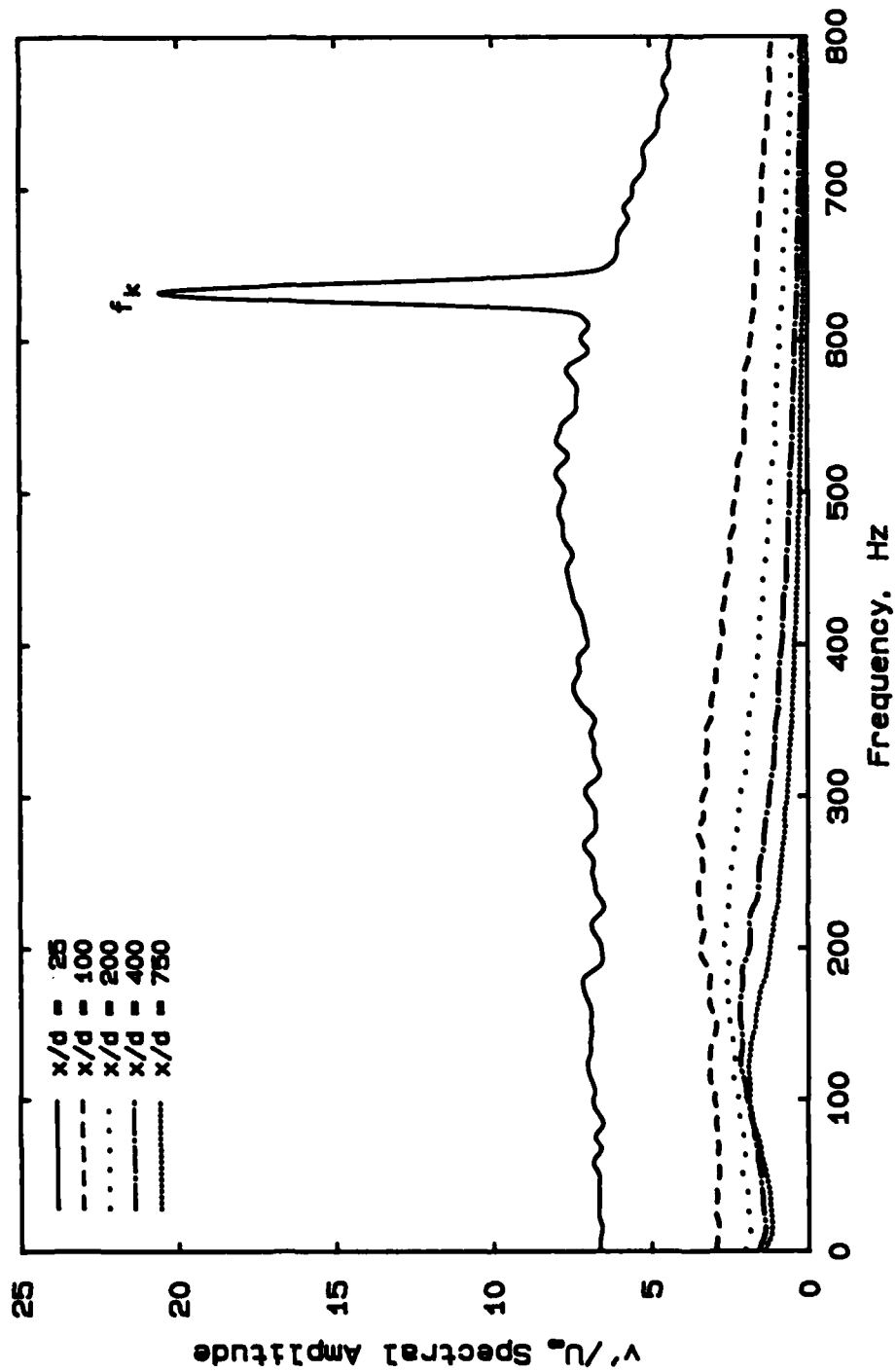


Figure 5.7a) : Amplitude spectra at several downstream distances:  
circular cylinder wake at  $Re = 500$ .

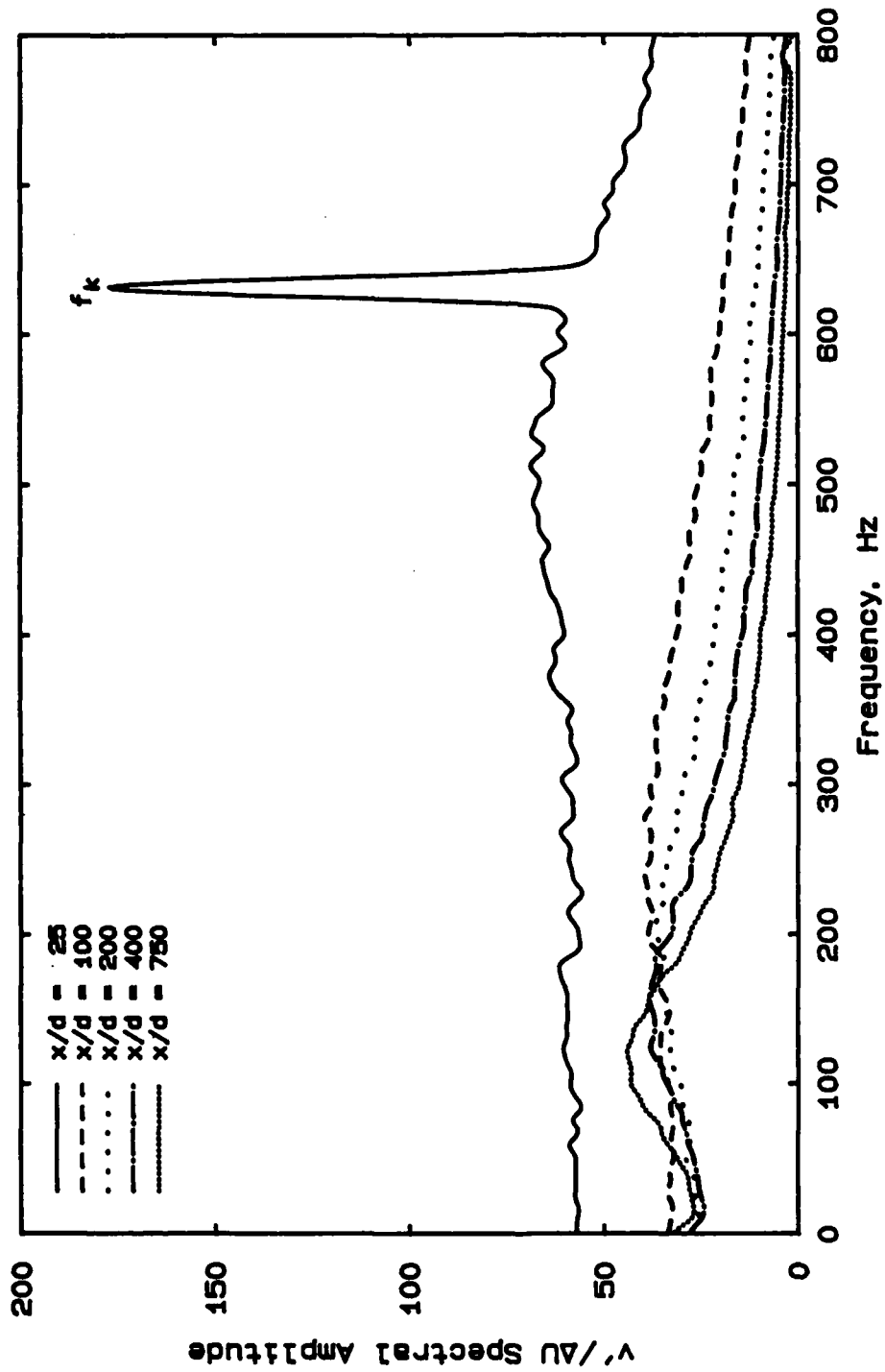


Figure 5.7b) : Normalized amplitude spectra at several downstream distances; circular cylinder wake at  $Re = 500$ .

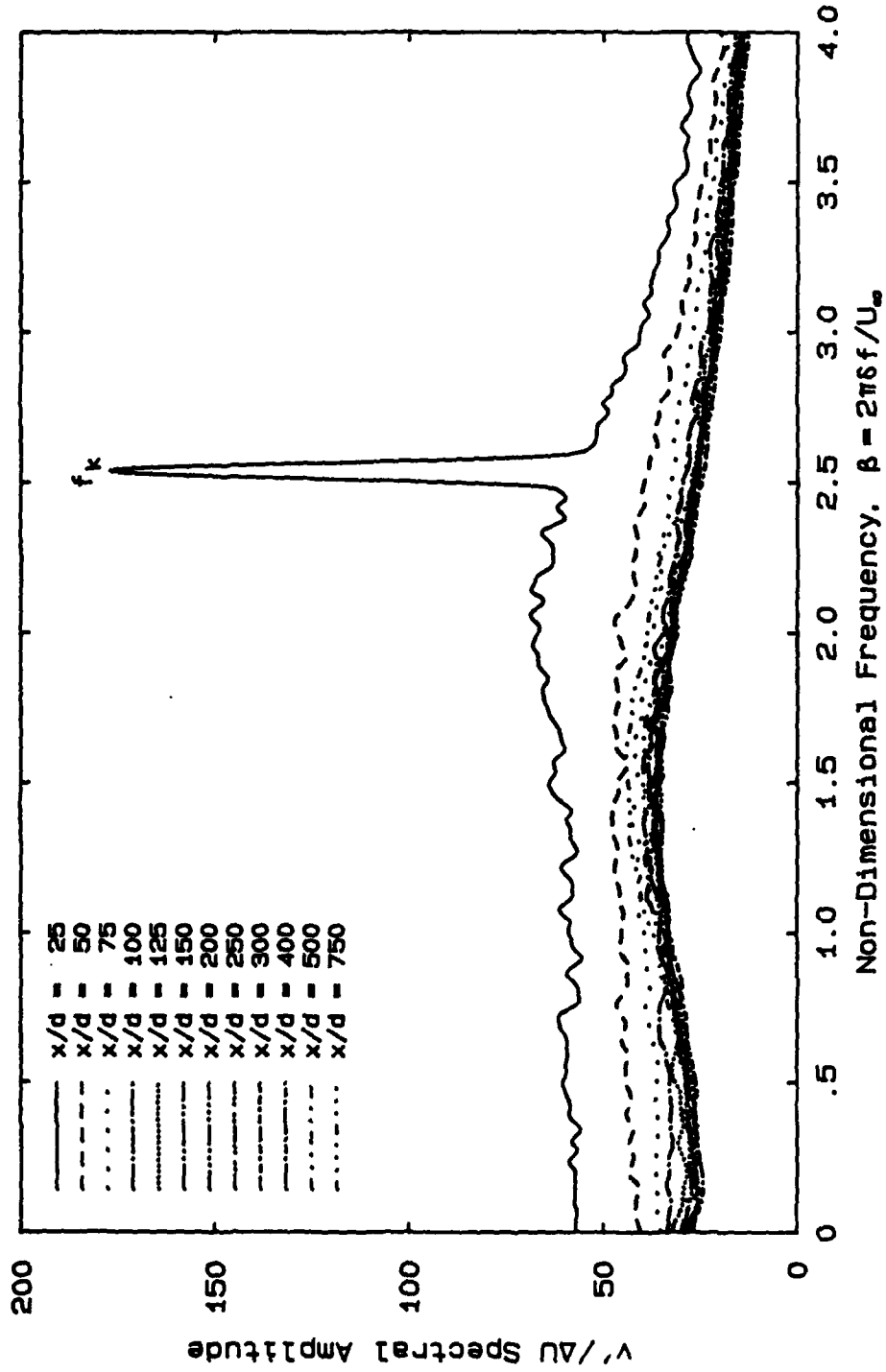


Figure 5.7c) : Fully normalized amplitude spectra at several downstream distances; circular cylinder wake at  $Re = 500$ .

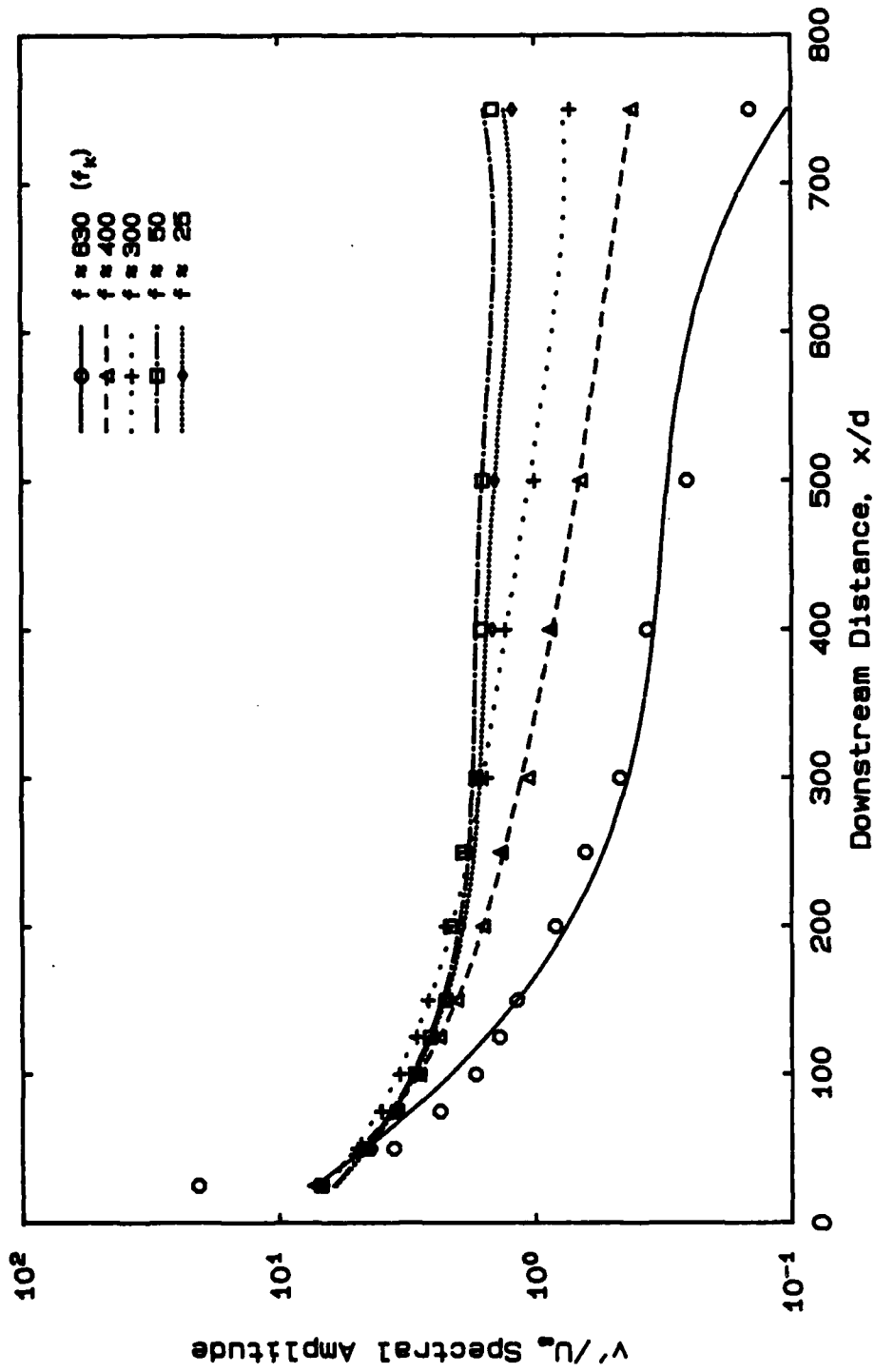


Figure 5.8a) : Growth-decay cycles of selected discrete frequencies:  
circular cylinder wake at  $Re = 500$ .

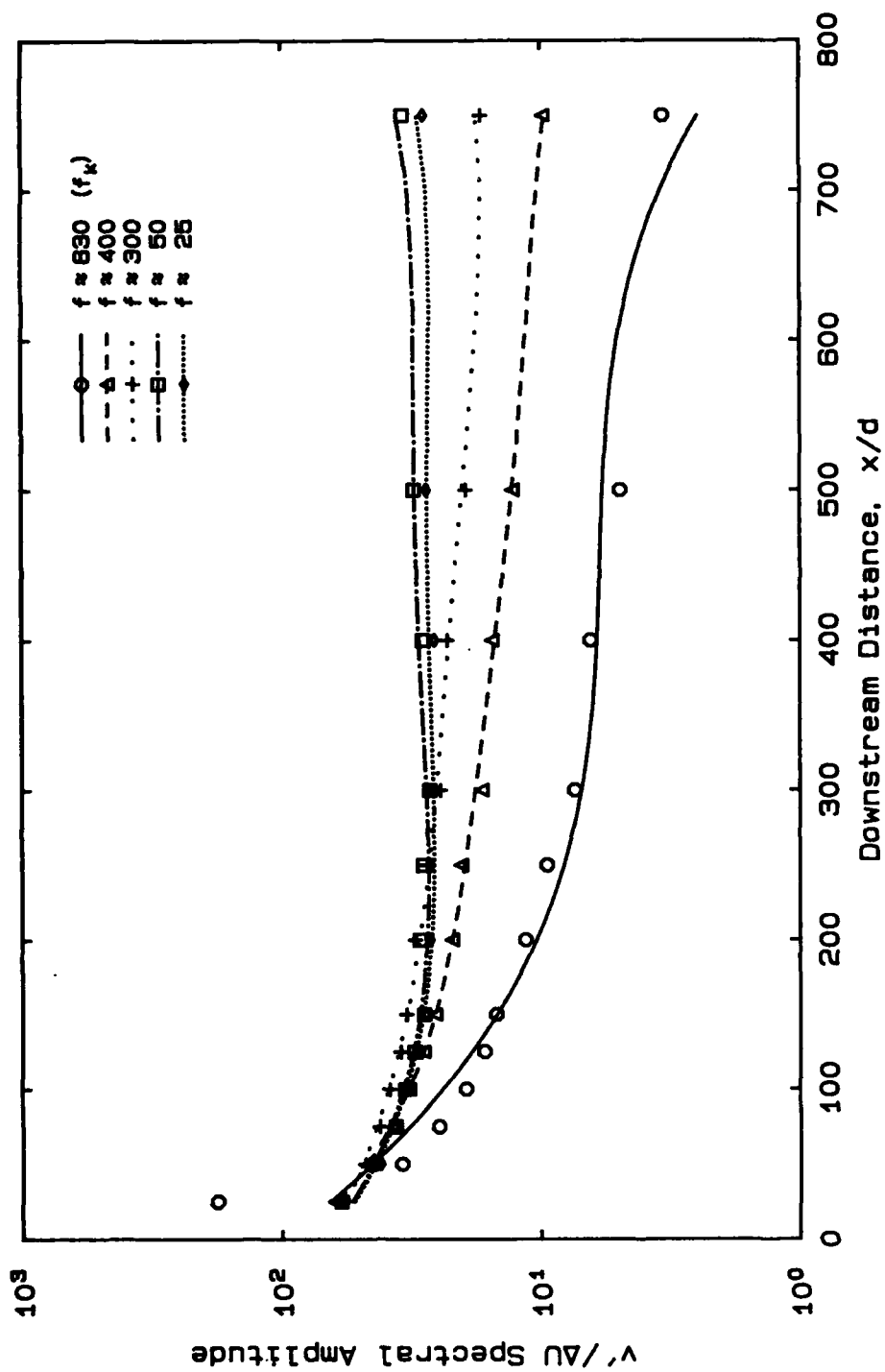


Figure 5.8b) : Normalized growth-decay cycles of selected discrete frequencies; circular cylinder wake at  $Re = 500$ .

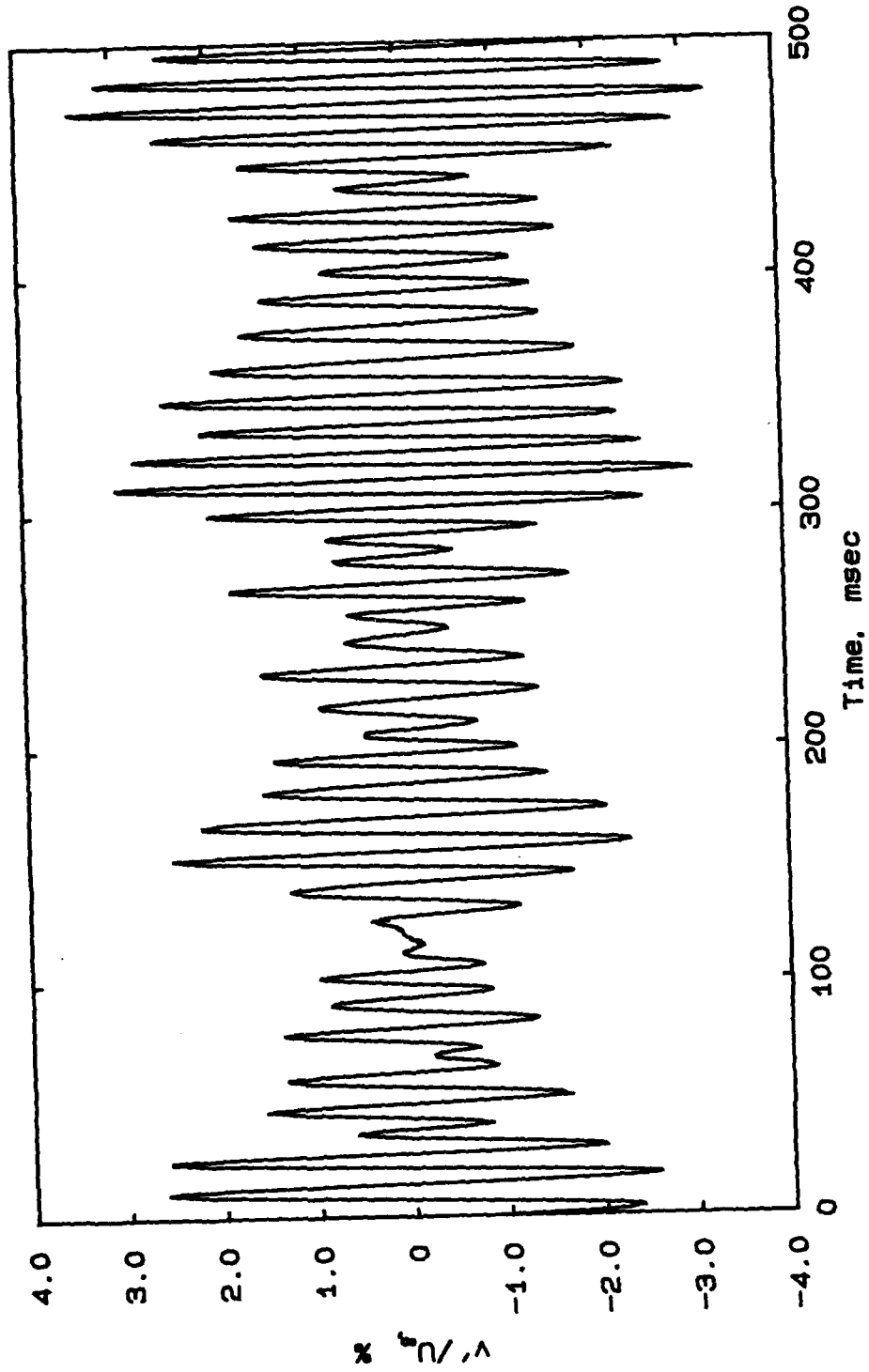


Figure 5.9: Time-trace of  $v'/U_\infty$ : circular cylinder wake  
at  $Re = 150$ ,  $x/d = 200$ , and  $y/d = 1.5$ .

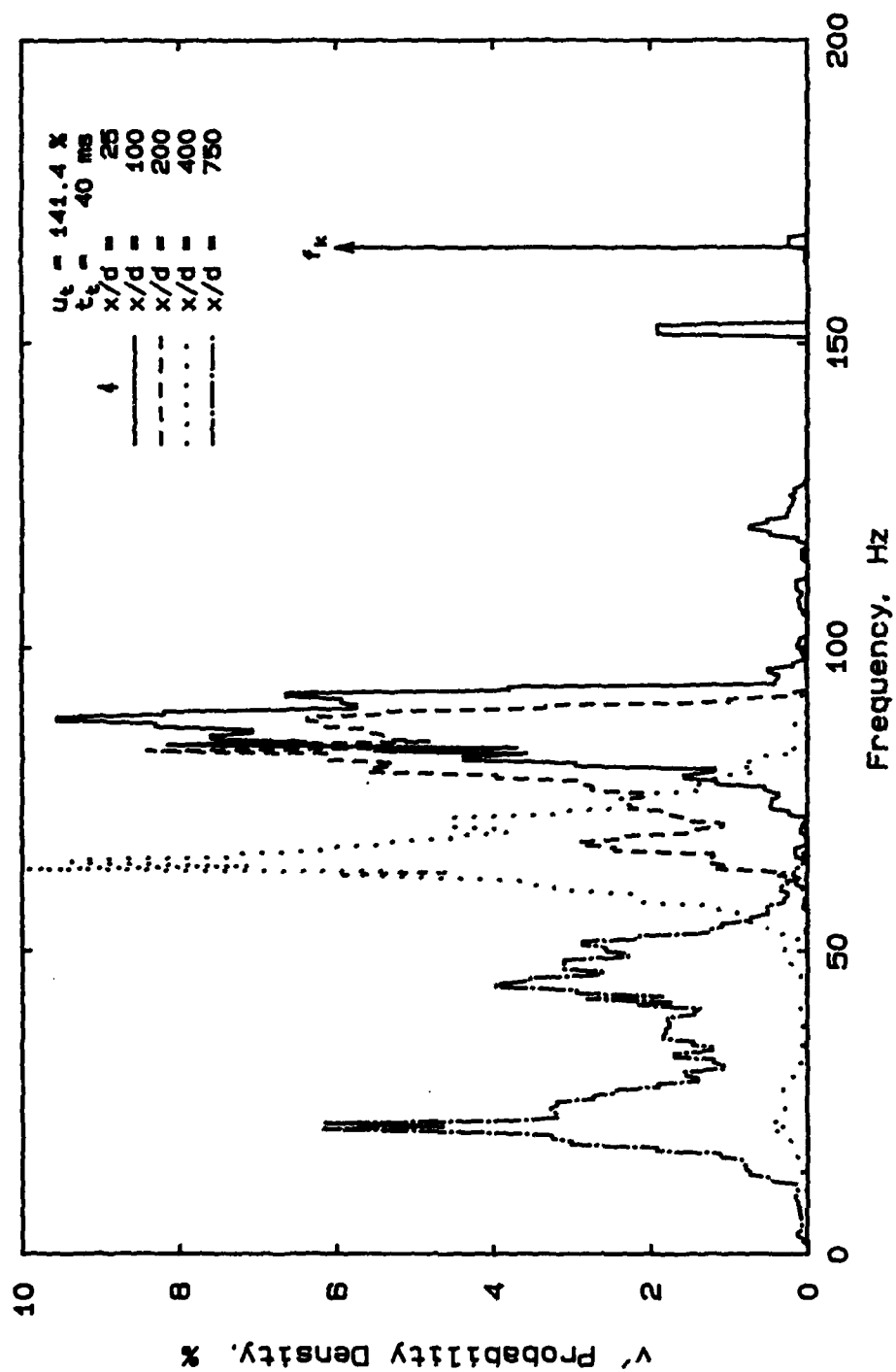


Figure 5.10: Probability density functions of  $v'$  fluctuations: circular cylinder wake at  $Re = 150$ .

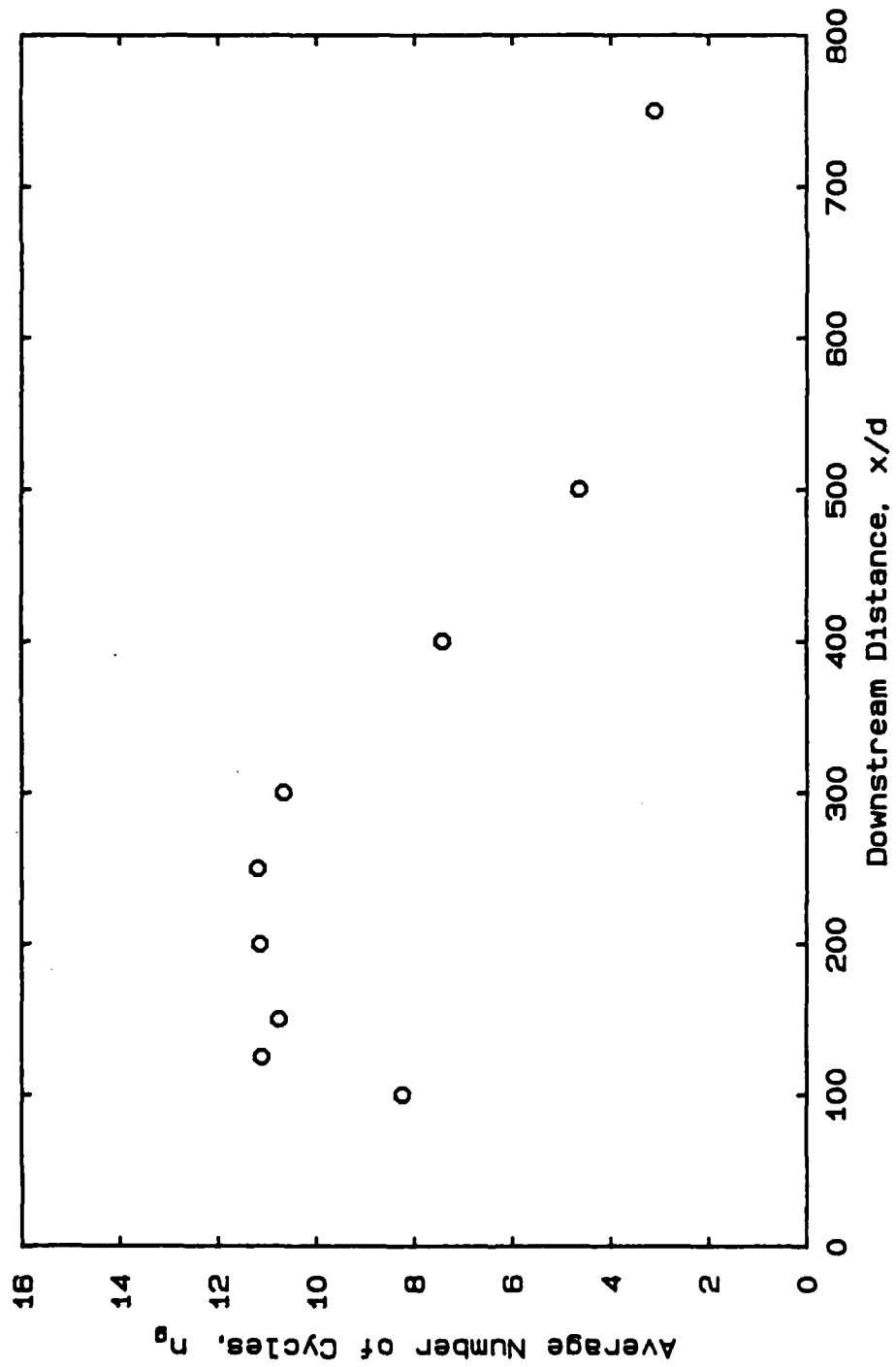


Figure 5.11: Average number of cycles per group versus downstream distance; circular cylinder wake at  $Re = 150$ .



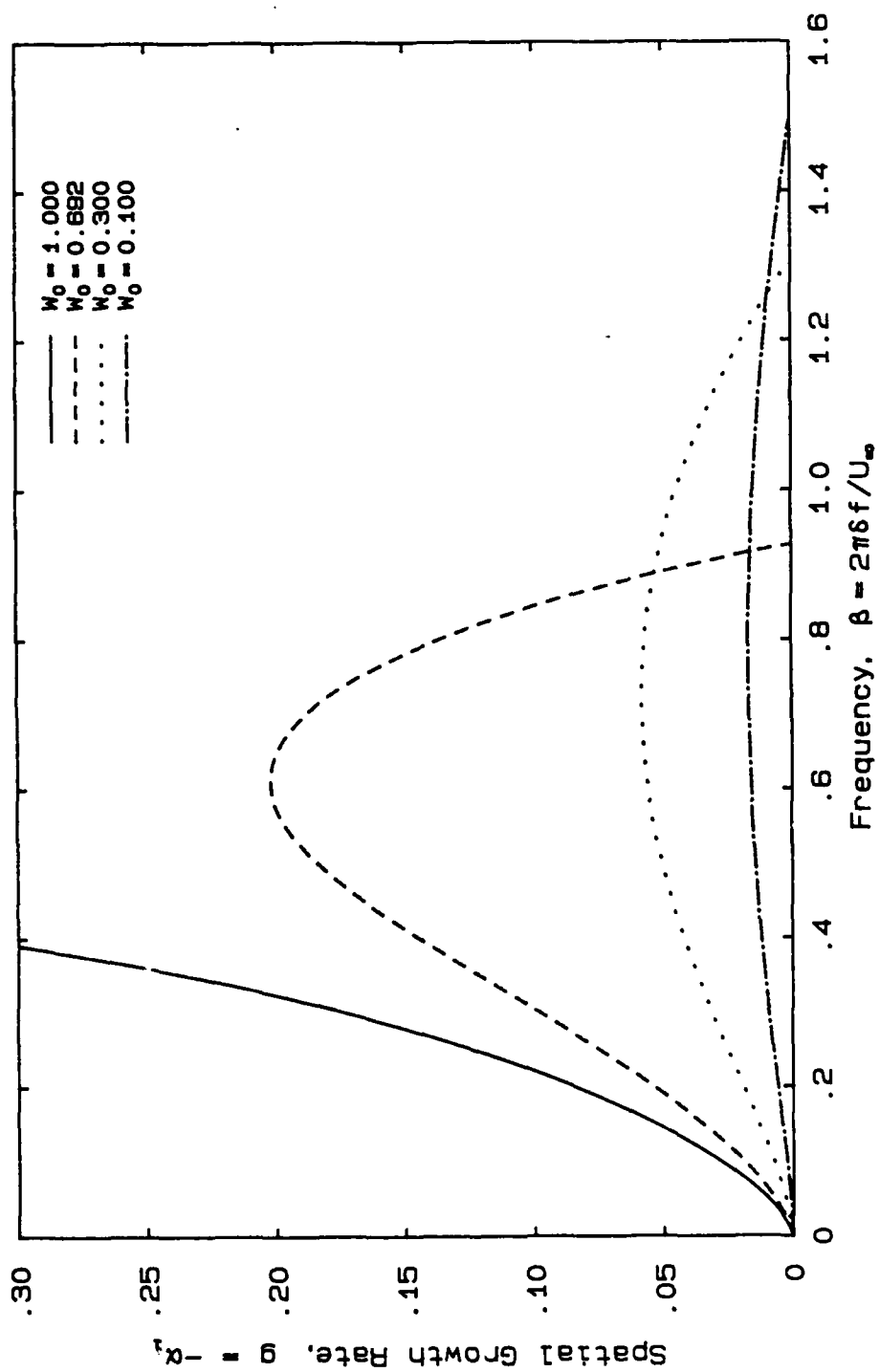


Figure 5.12: Spatial inviscid stability solutions. Gaussian wake profile.

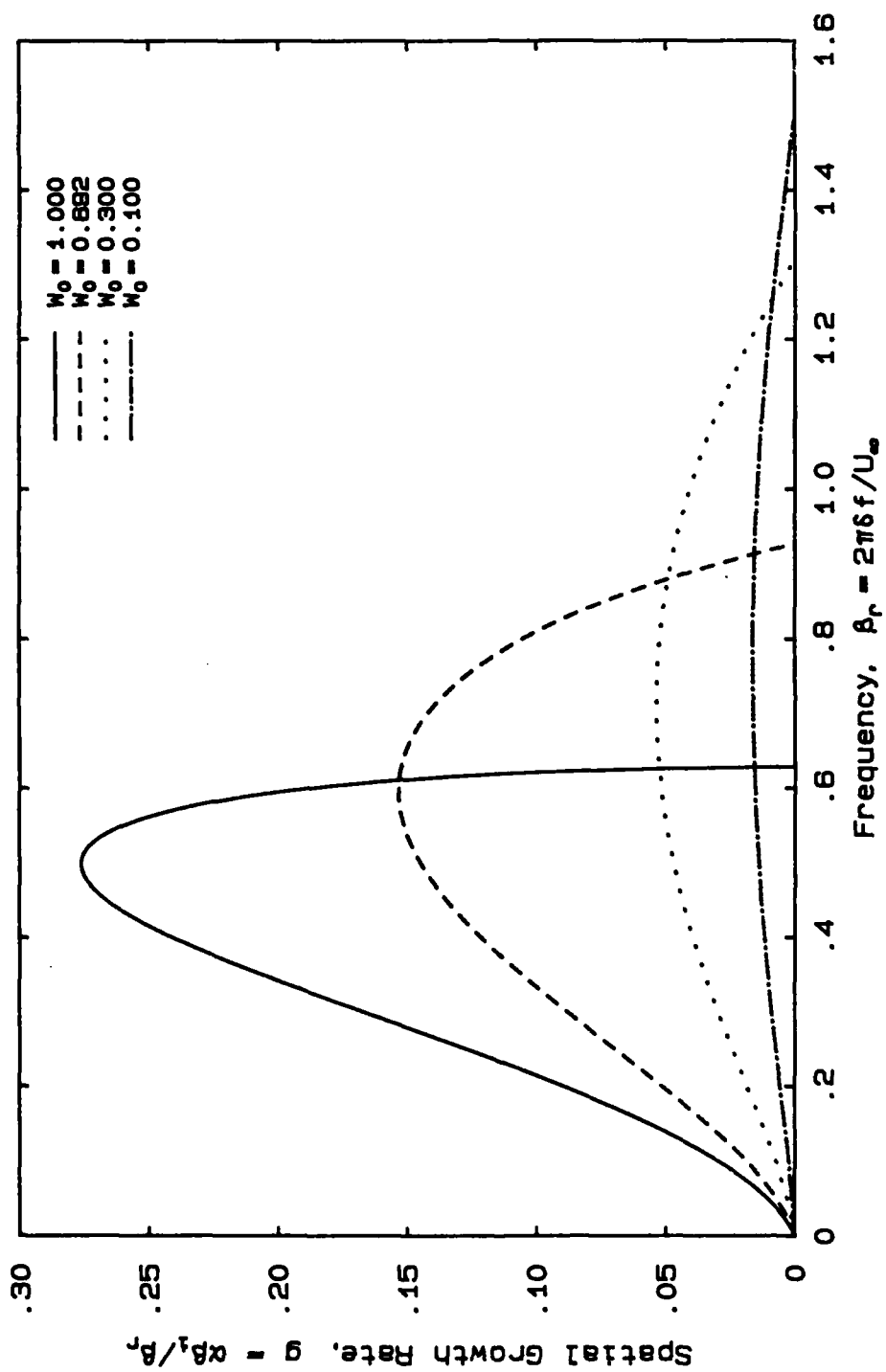


Figure 5.13: Temporal inviscid stability solutions. Gaussian wake profile.

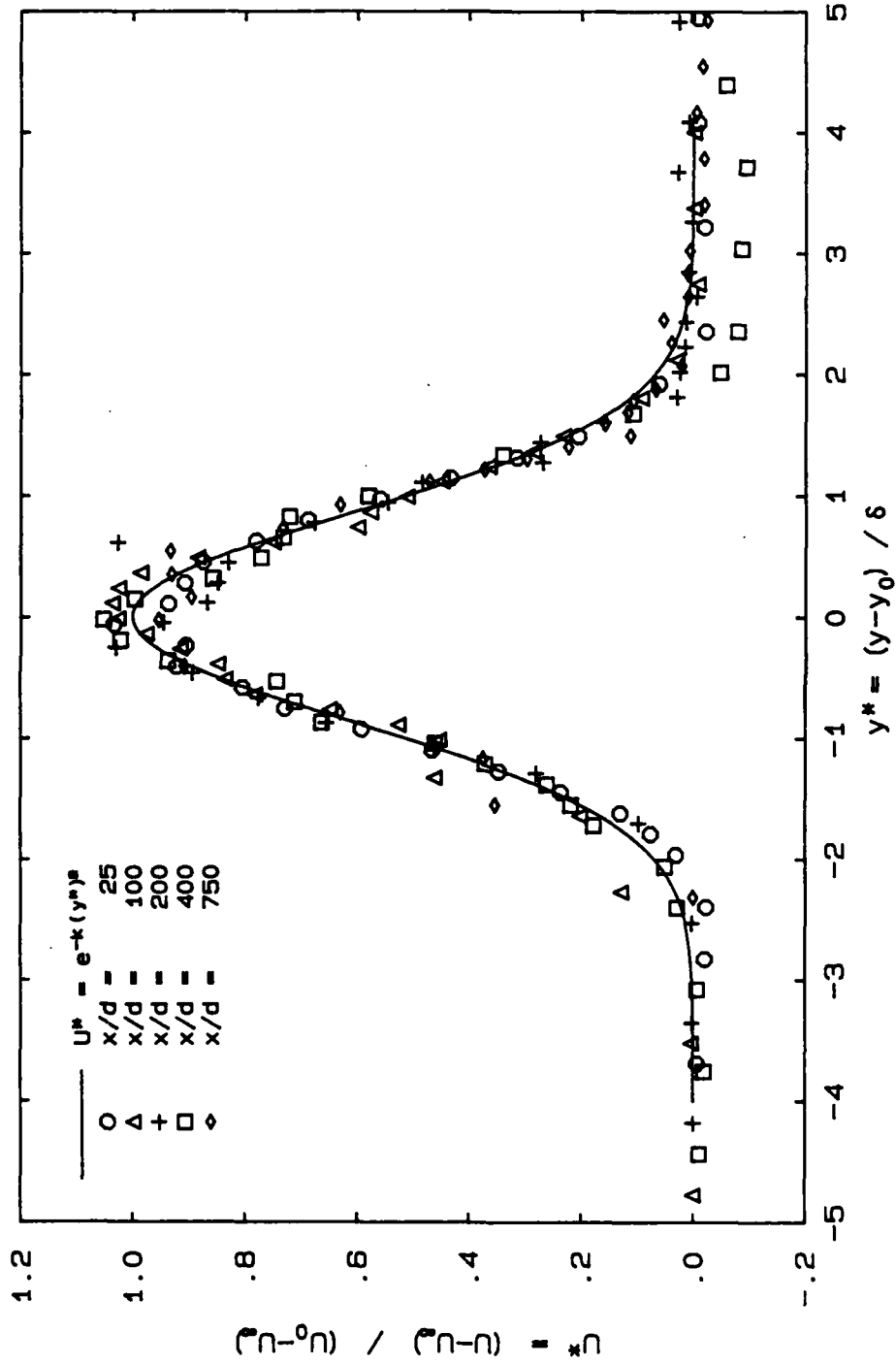


Figure 5.14: Mean velocity profiles; circular cylinder wake at  $Re = 150$ .

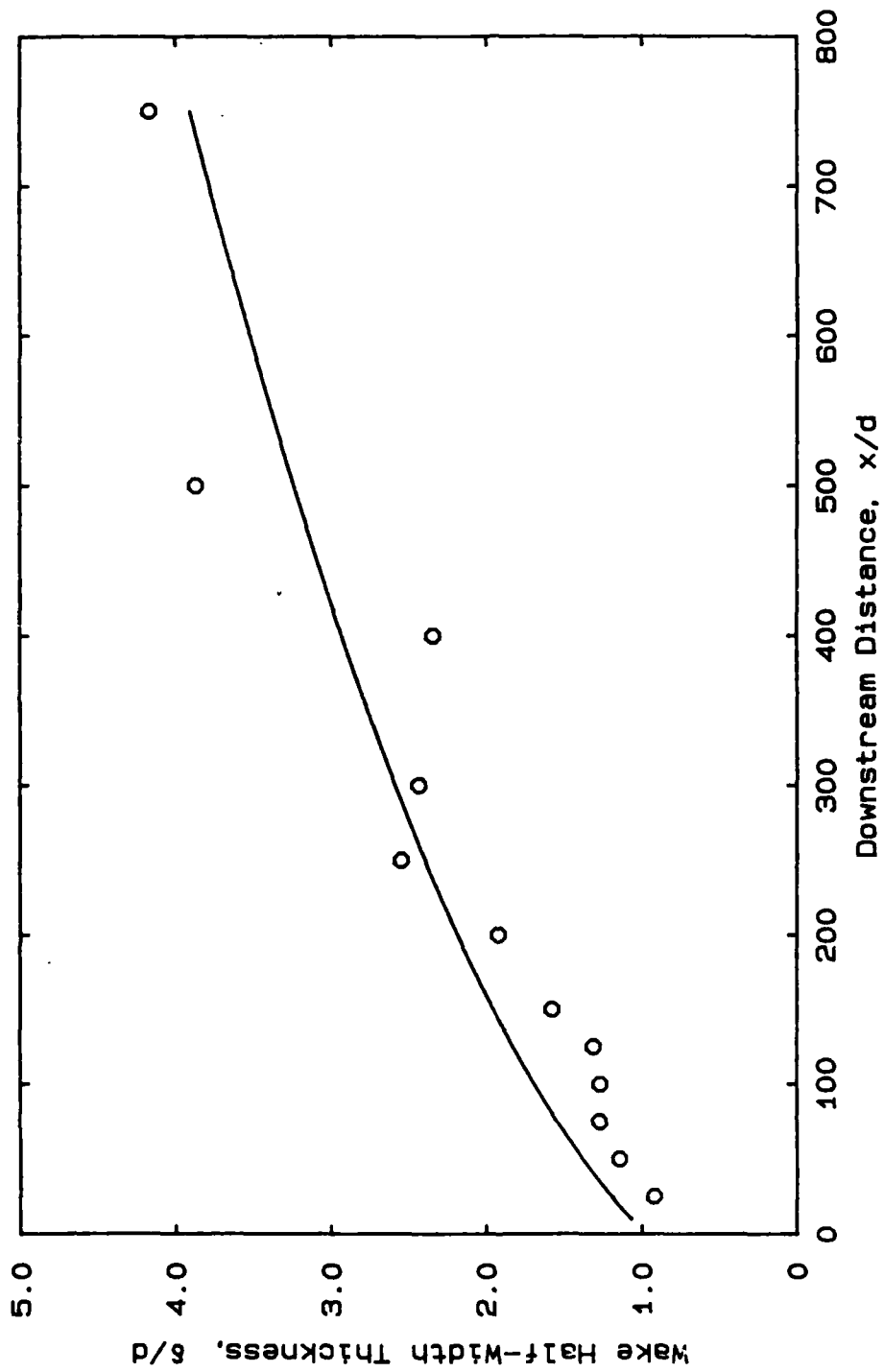


Figure 5.15: Wake half-width thickness vs. downstream distance; circular cylinder wake at  $Re = 150$ .

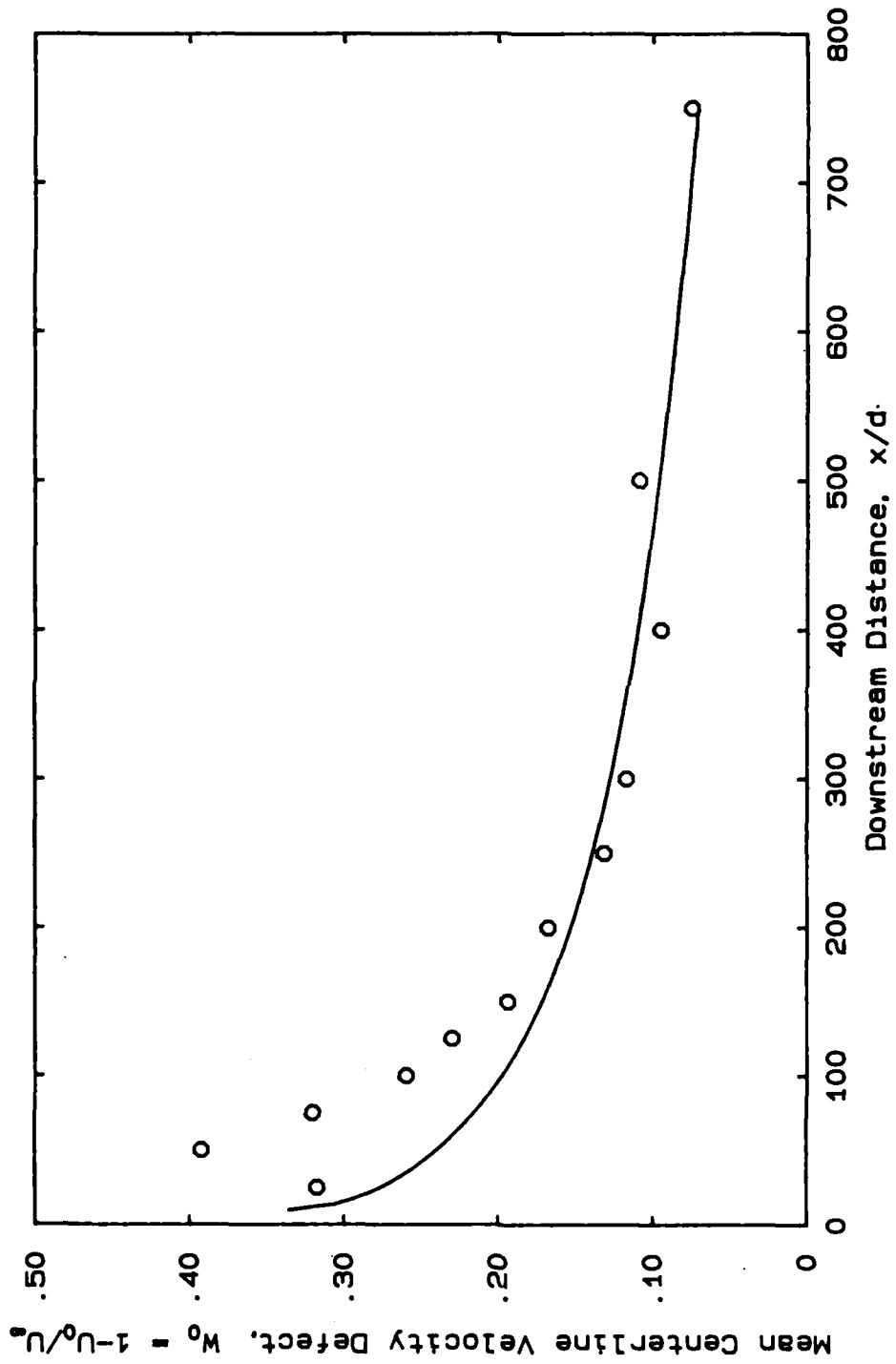


Figure 5.16: Velocity defect vs. downstream distance; circular cylinder wake at  $Re = 150$ .

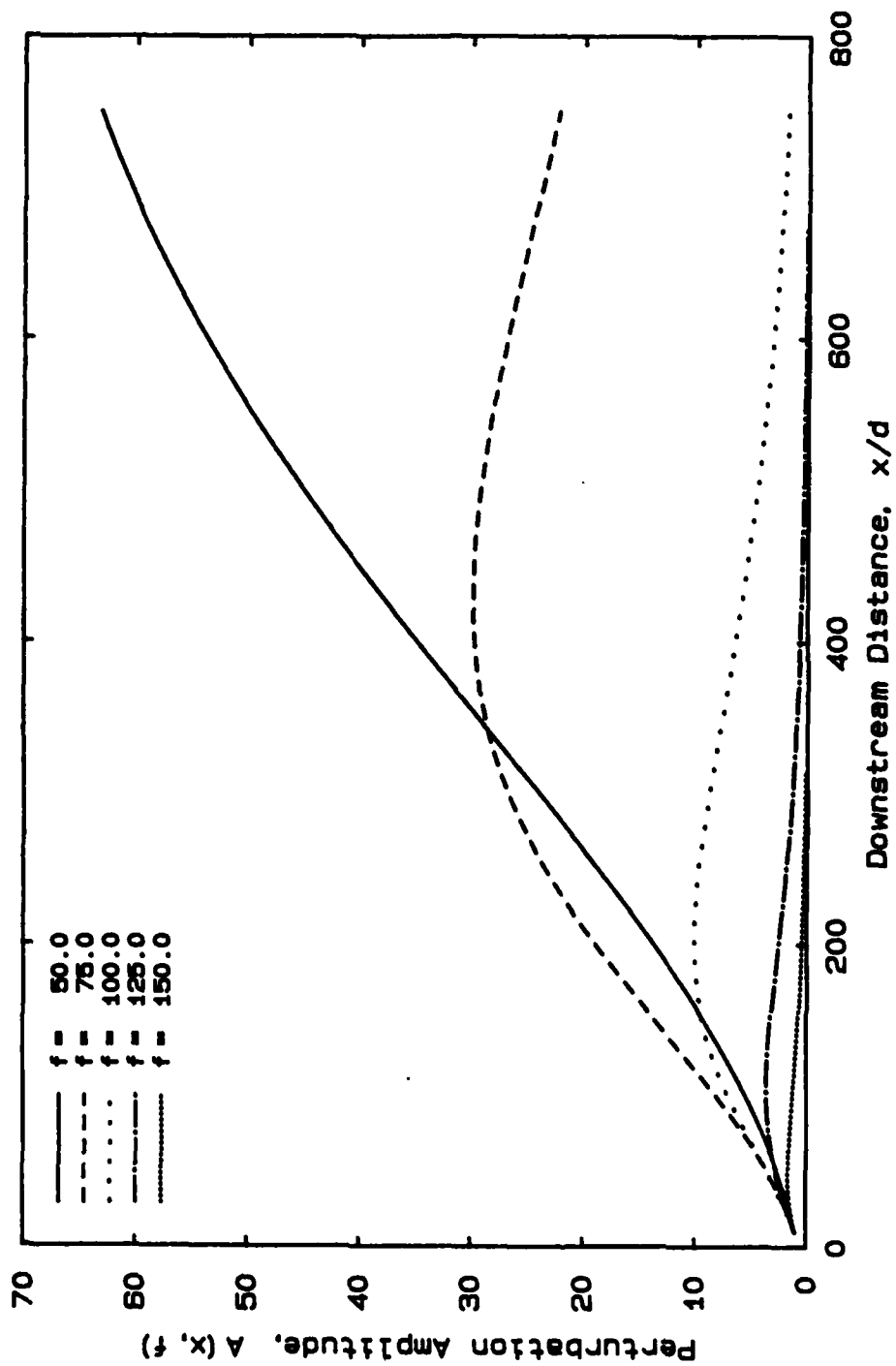


Figure 5.17: Numerical simulation of growth-decay cycles; circular cylinder wake at  $Re = 150$ .

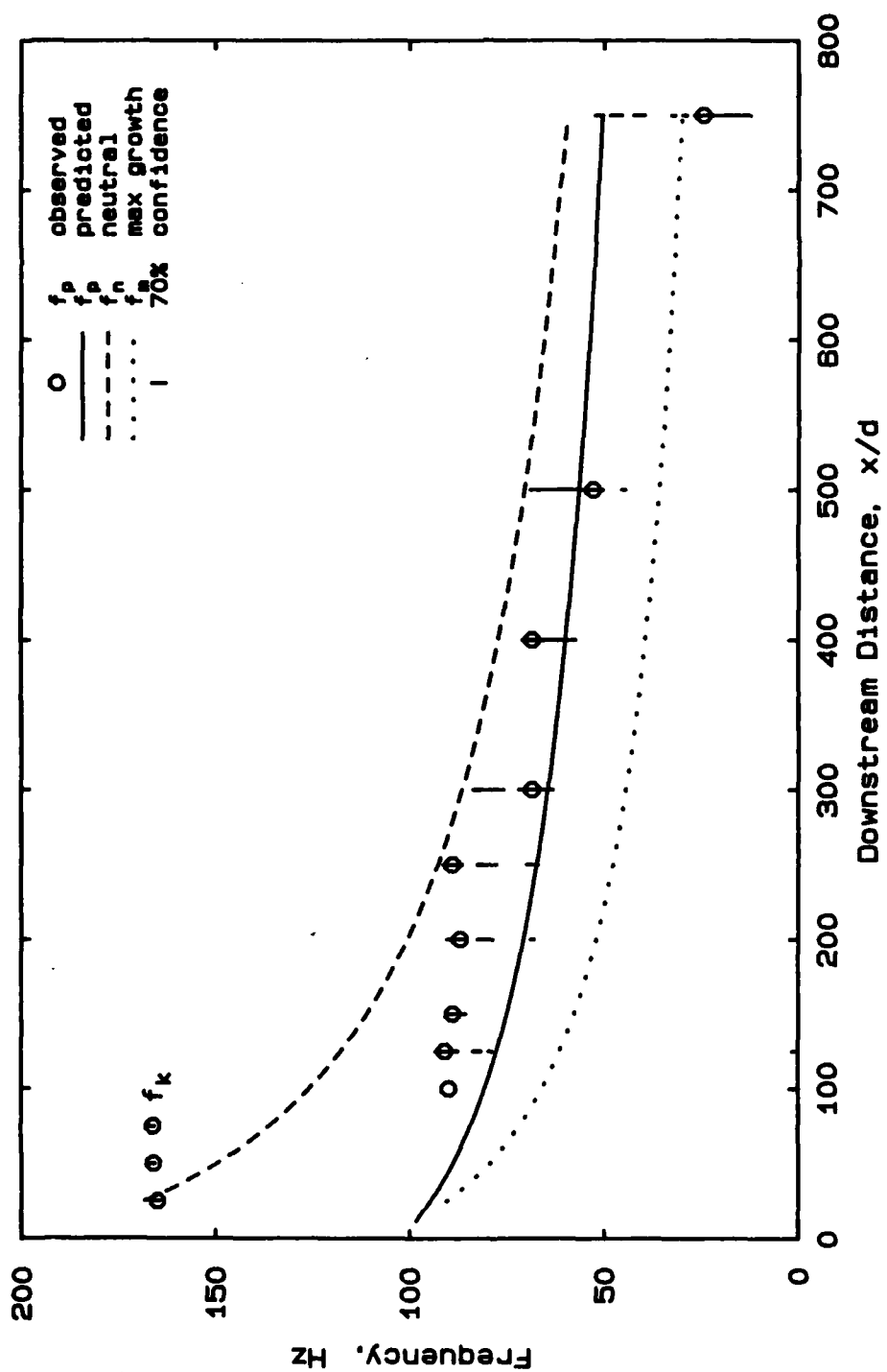


Figure 5.18: Peak frequency vs. downstream distance: circular cylinder wake at  $Re = 150$ .

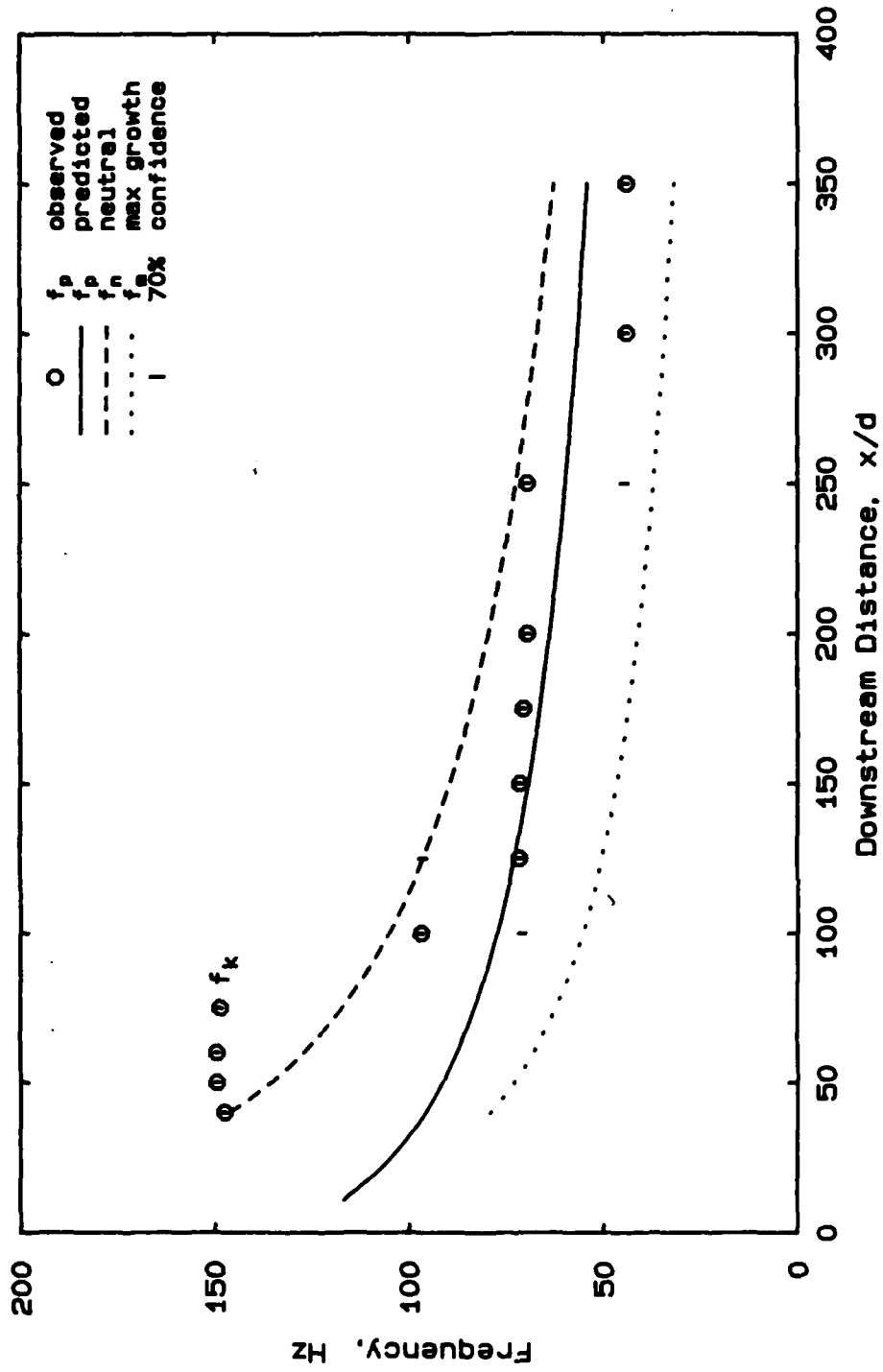


Figure 5.19: Peak frequency vs. downstream distance; circular cylinder wake at  $Re=140$ .



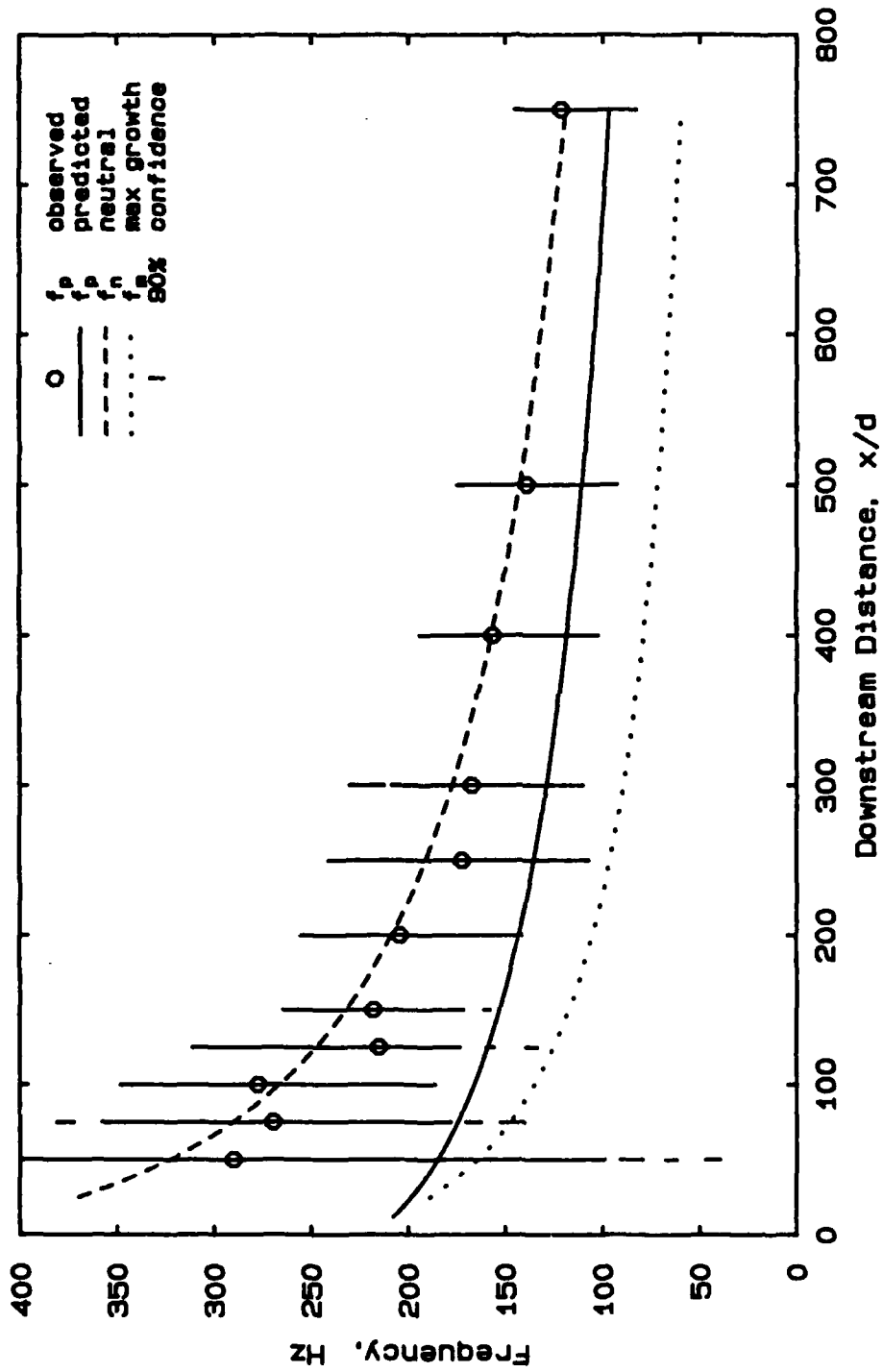


Figure 5.20: Peak frequency vs. downstream distance; circular cylinder wake at  $Re = 500$ .

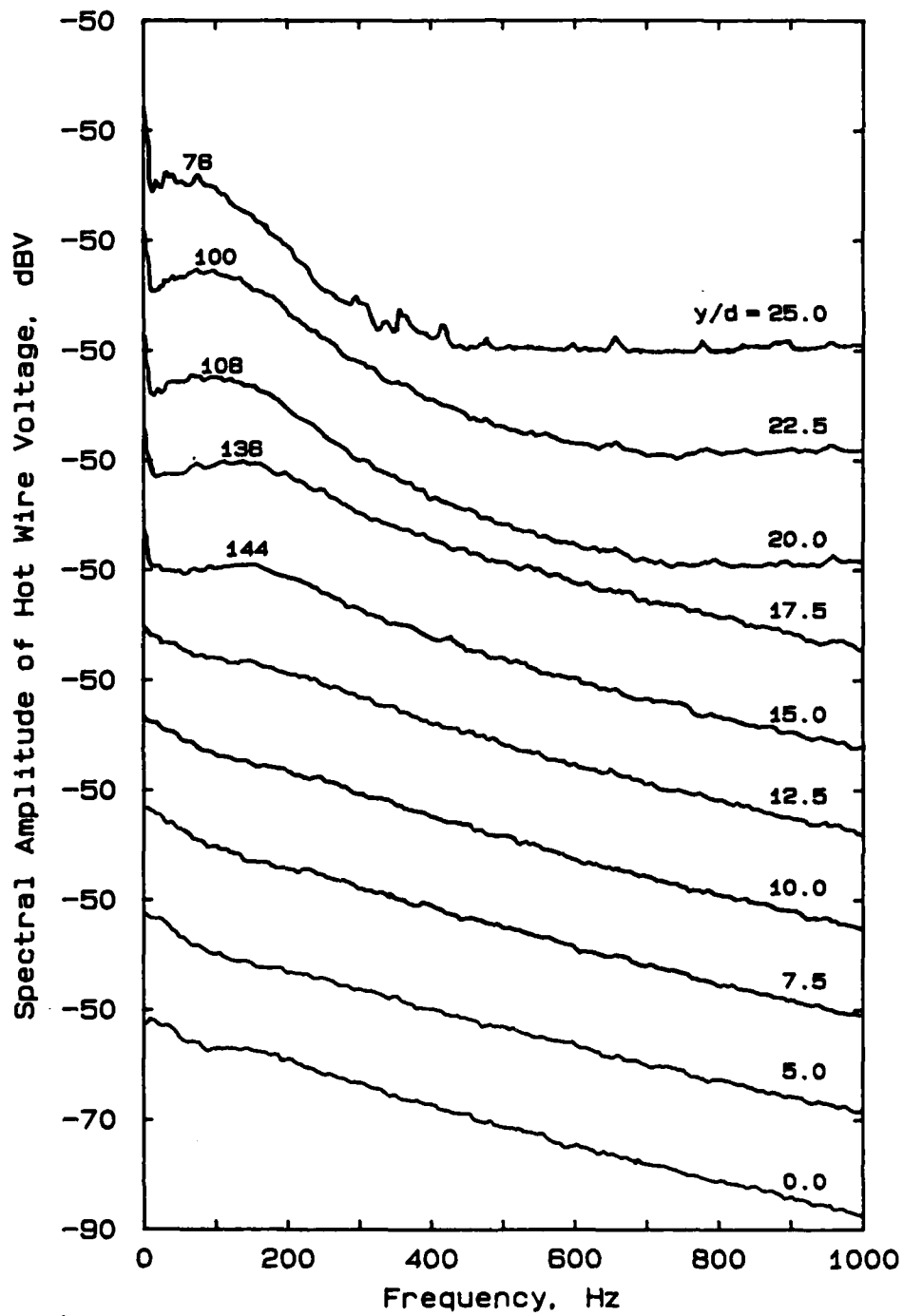


Figure 5.21: Amplitude spectra at several  $y$ -locations; cylinder wake at  $Re = 300$ , and at  $x/d = 750$ .

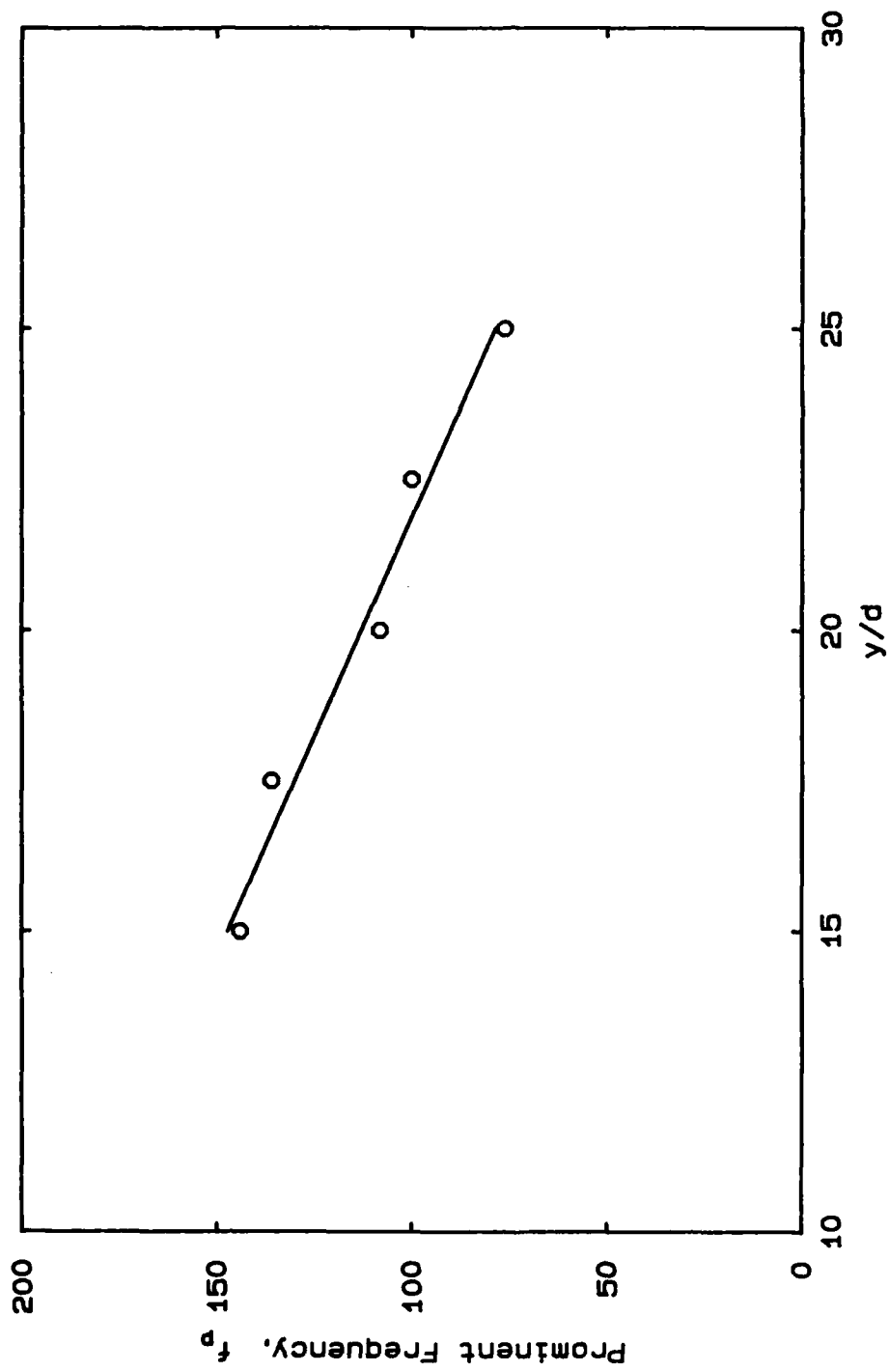


Figure 5.22: Prominent frequency versus  $y$ ; circular cylinder wake at  $Re = 300$ , and at  $x/d = 750$ .

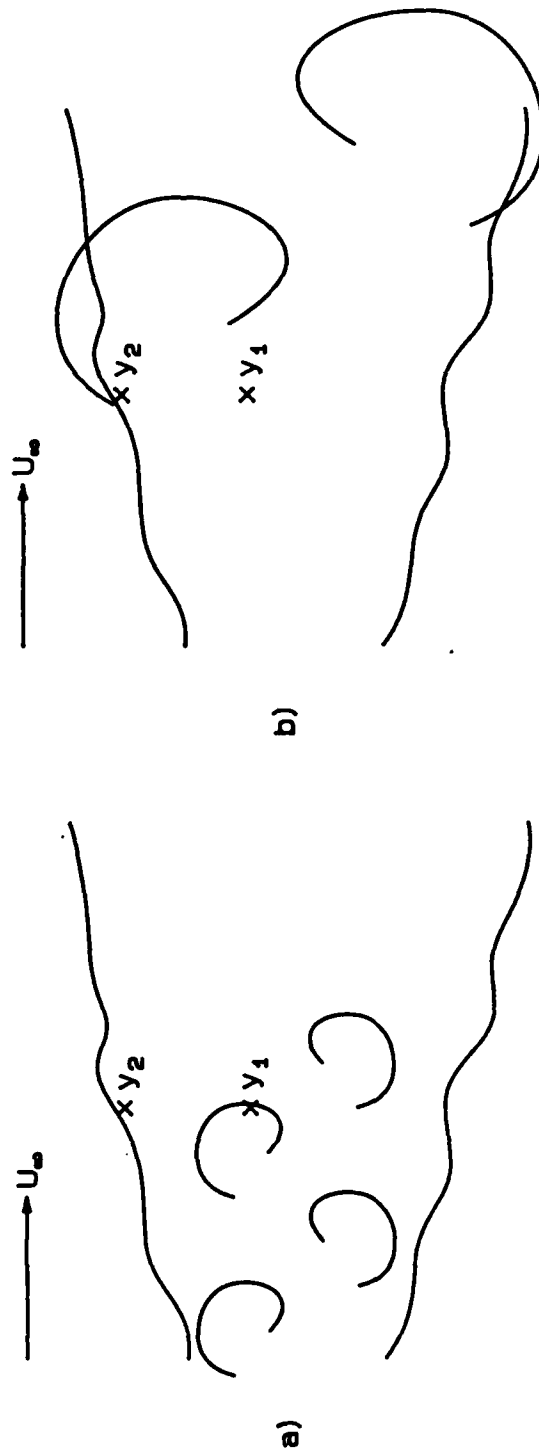


Figure 5.23: Sketch of frequency-sensitivity in the y-direction, probes at  $y_1$  and  $y_2$ : a) high frequency, b) low frequency structure.

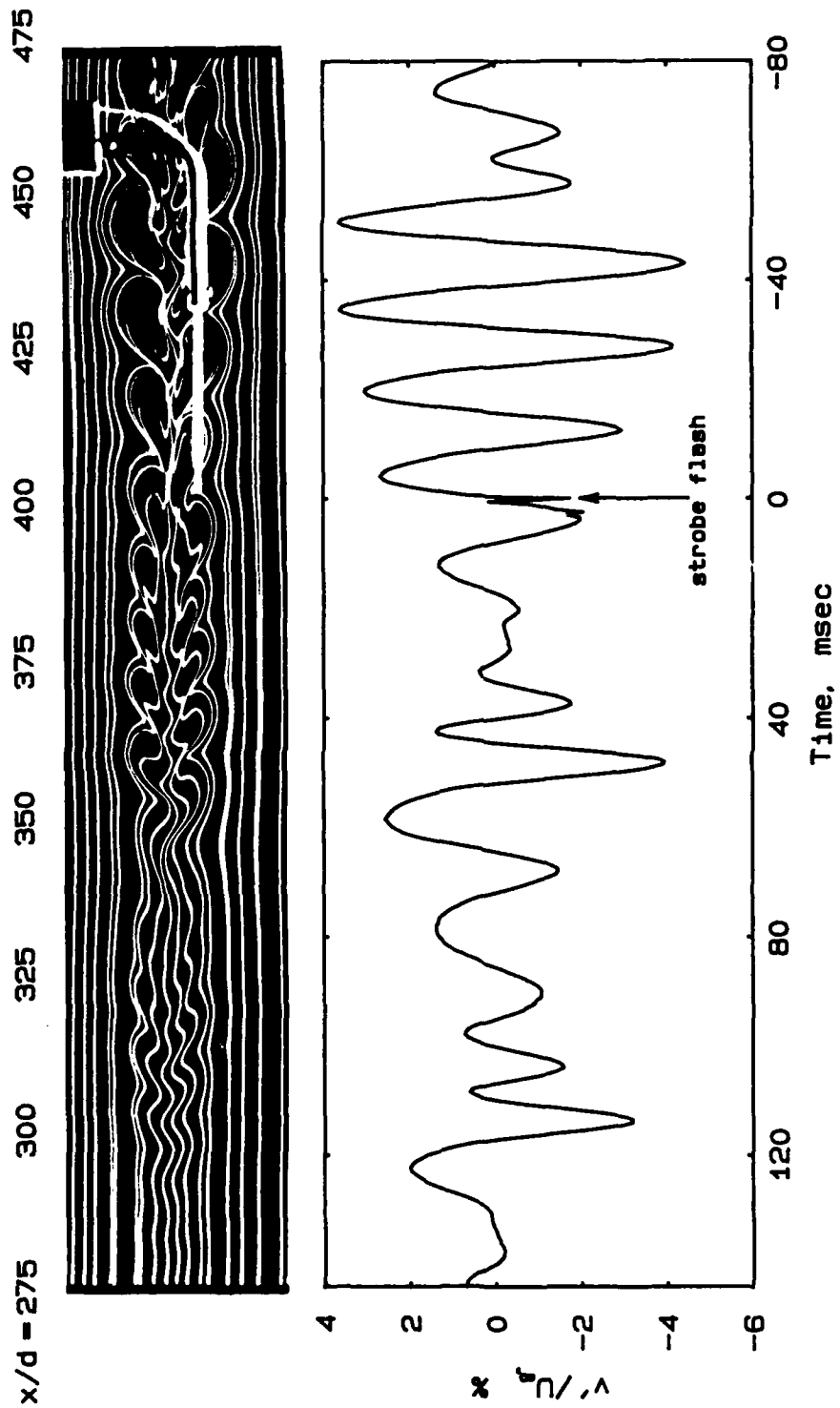


Figure 5.24: Simultaneous smoke-wire and cross-wire records, circular cylinder wake at  $Re = 150$ ; smoke-wire at  $x/d = 275$ , cross-wire at  $x/d = 400, y/d = -4$ .

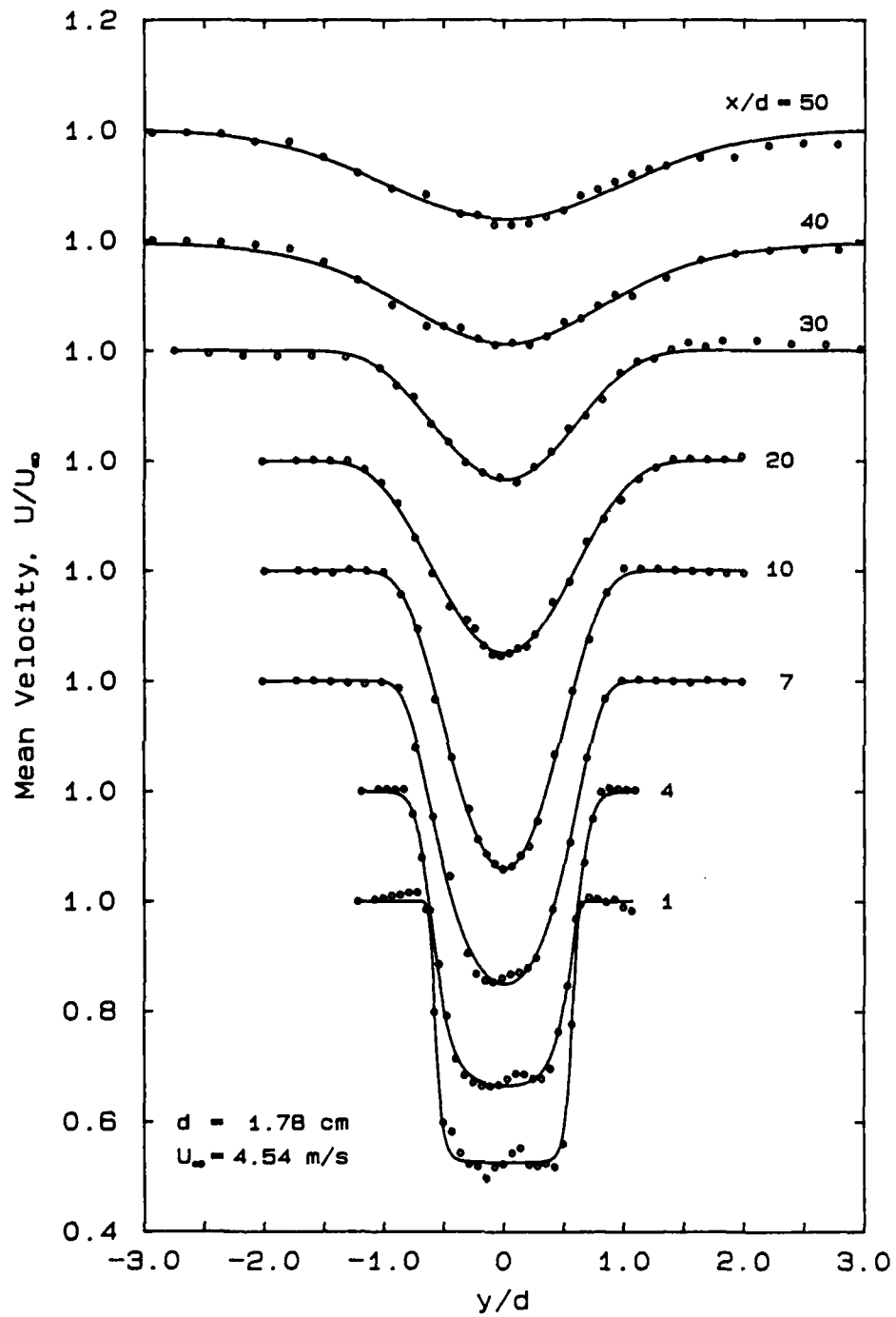


Figure 5.25: Mean velocity profiles for porous flat plate;  $\sigma = 47\%$ ,  $Re = 5000$ .

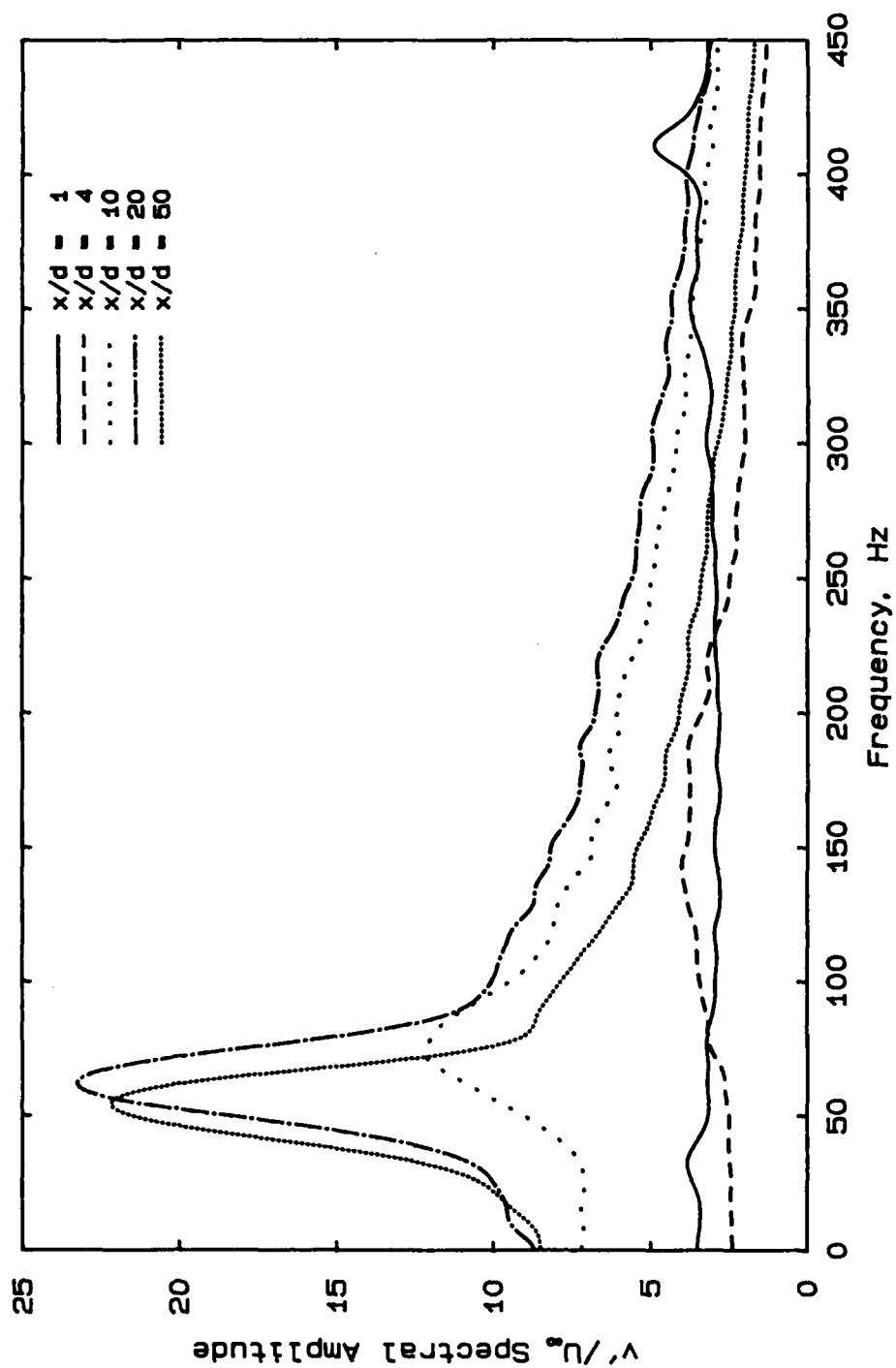


Figure 5.26: Amplitude spectra at several downstream distances;  
porous flat plate wake ( $\sigma = 47\%$ ) at  $Re = 5000$ .

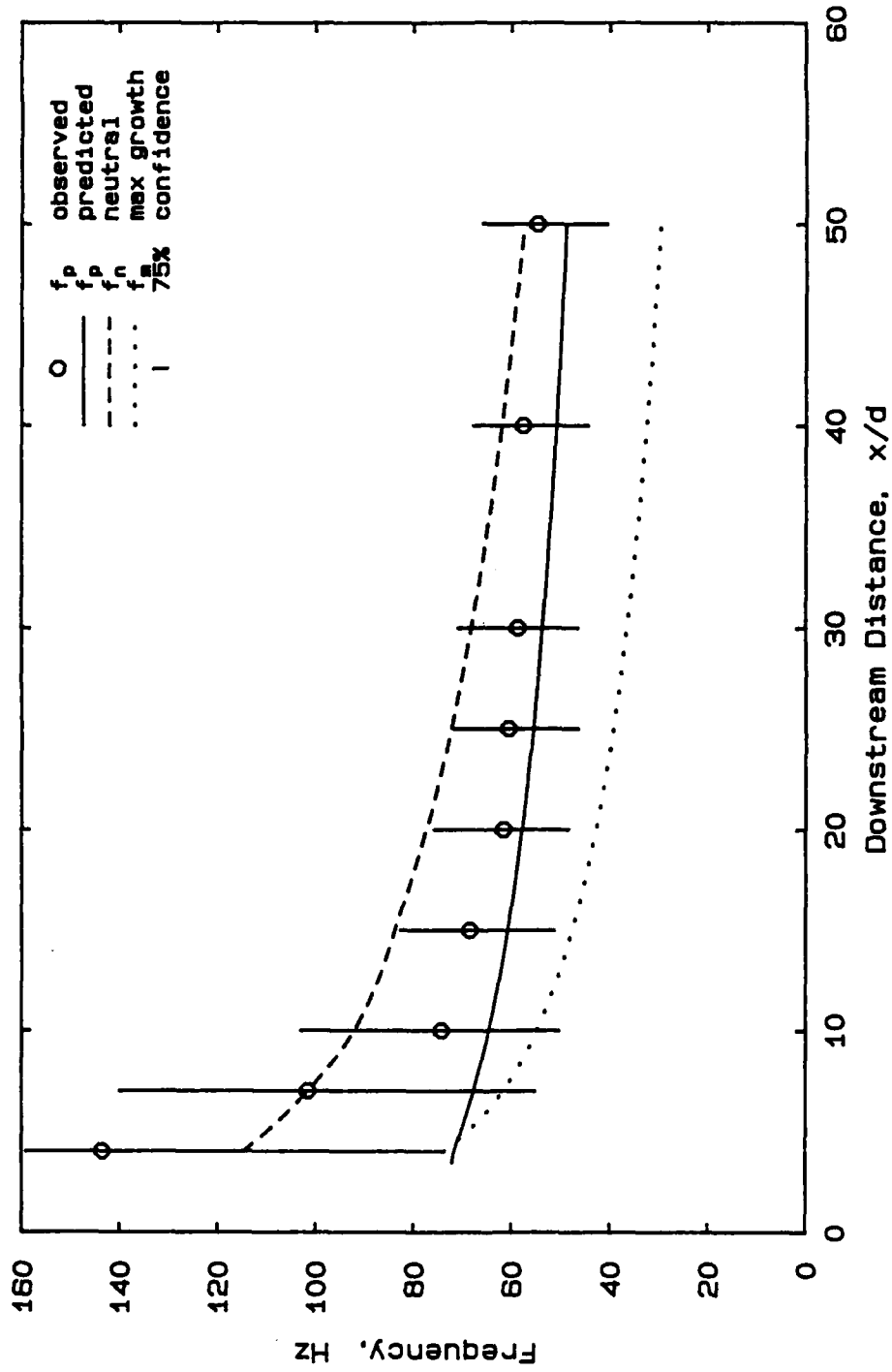


Figure 5.27: Peak frequency vs. downstream distance: porous flat plate wake ( $\sigma = 47\%$ ) at  $Re = 5000$ .



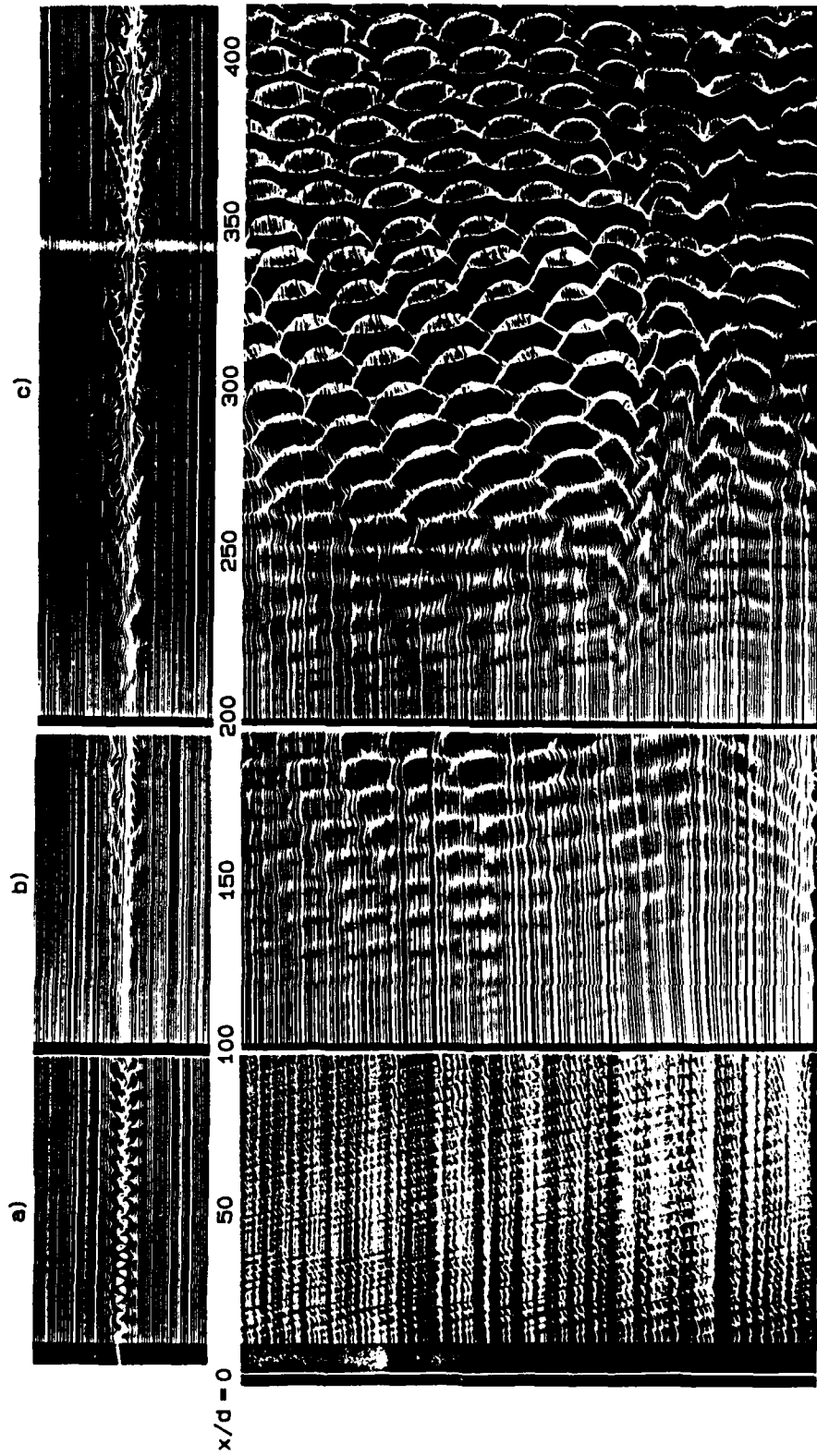


Figure 6.1: Edge and plan views of a circular cylinder wake at  $Re = 140$ ; smoke-wire at  $x/d = a)$  8, b) 100, and c) 200, and at  $y/d = 0$ .

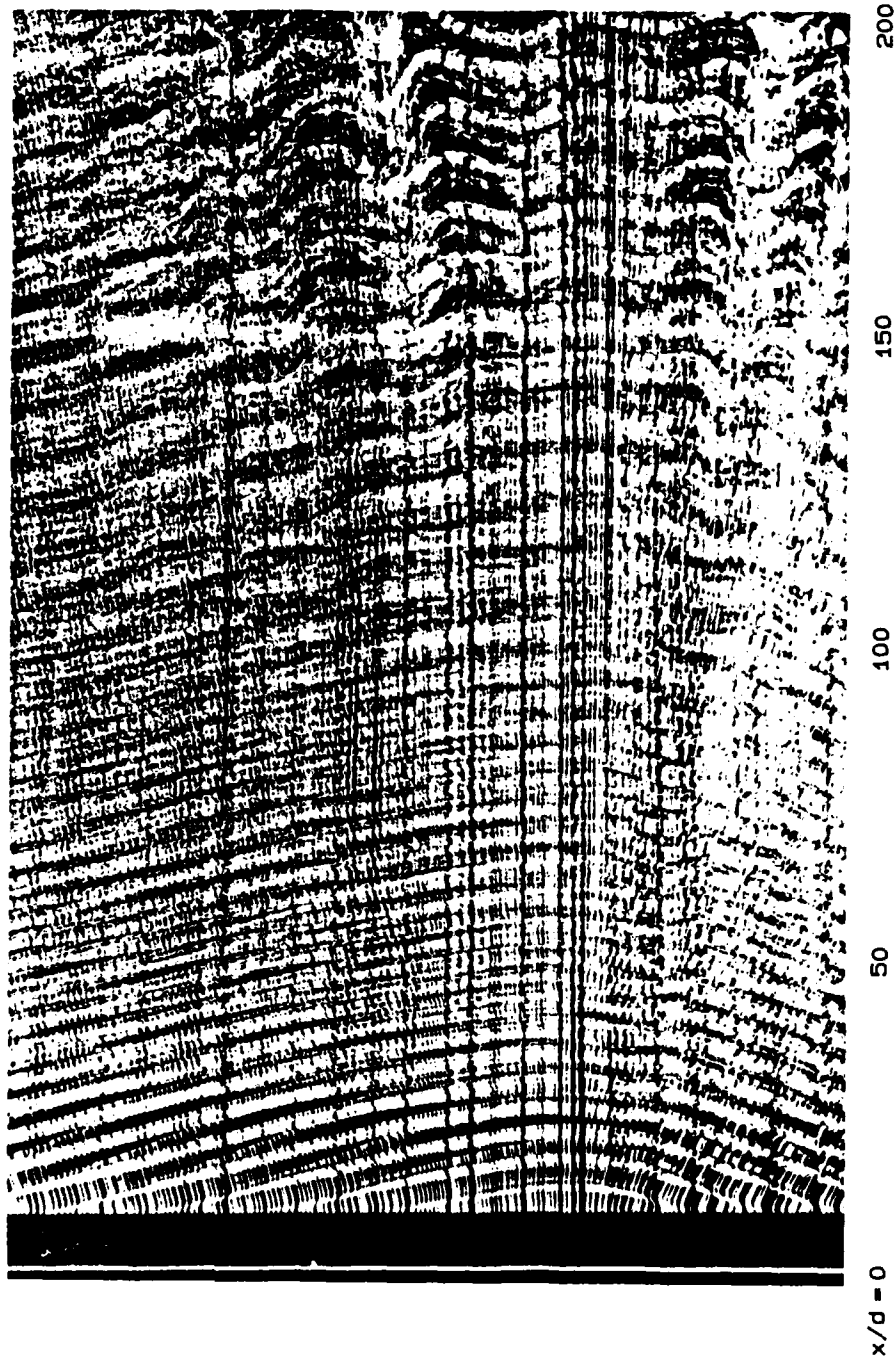


Figure 6.2: Plan view of a circular cylinder wake at  $Re = 155$ ;  
smoke wire at  $x/d = 8$ ,  $y/d = 0$ .

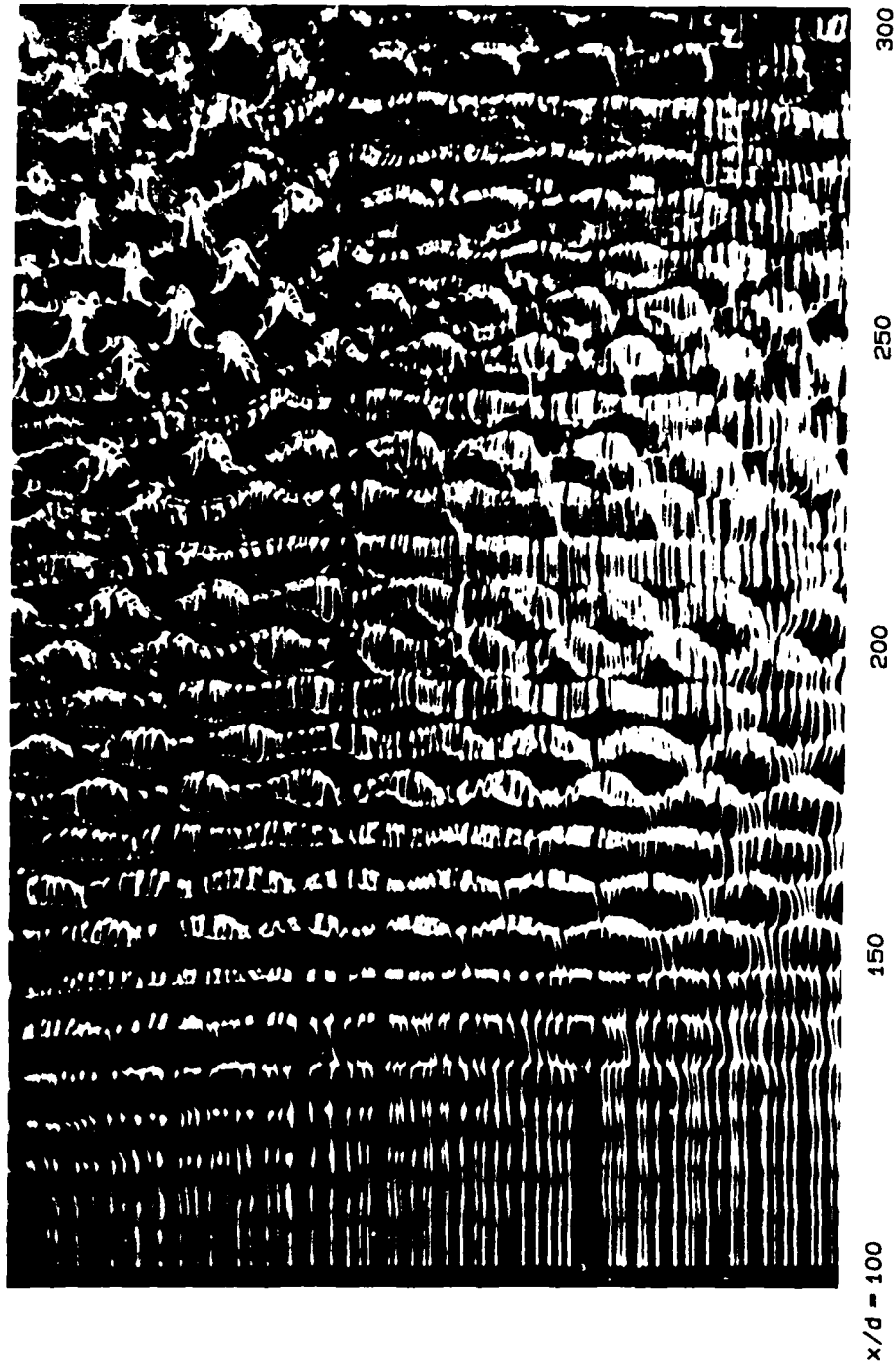


Figure 6.3: Plan view of a circular cylinder wake at  $Re = 150$ ;  
smoke wire at  $x/d = 100$ ,  $y/d = 2$ .

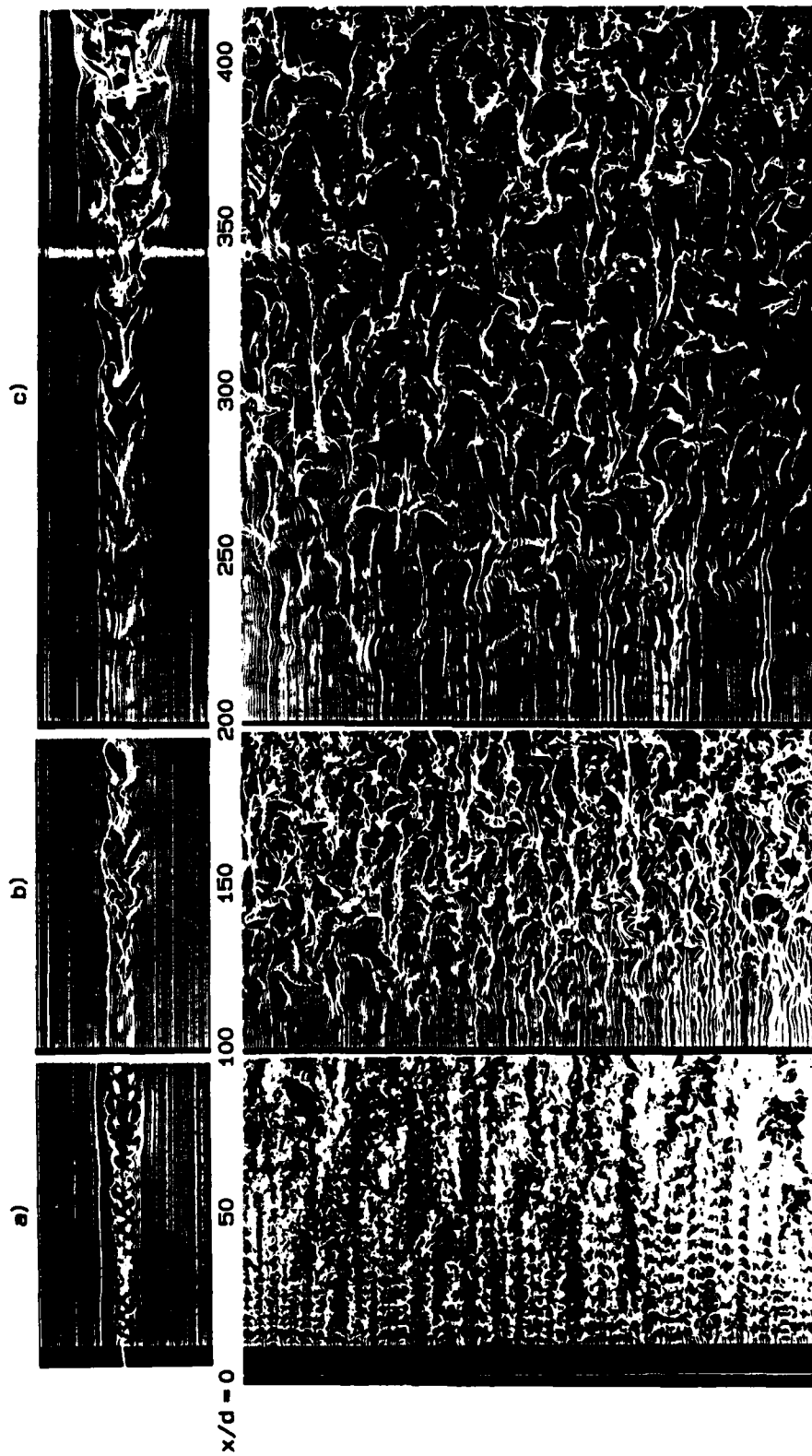


Figure 6.4: Edge and plan views of a circular cylinder wake at  $Re = 190$ ; smoke-wire at  $x/d =$  a) 8, b) 100, and c) 200, and at  $y/d = 0$ .

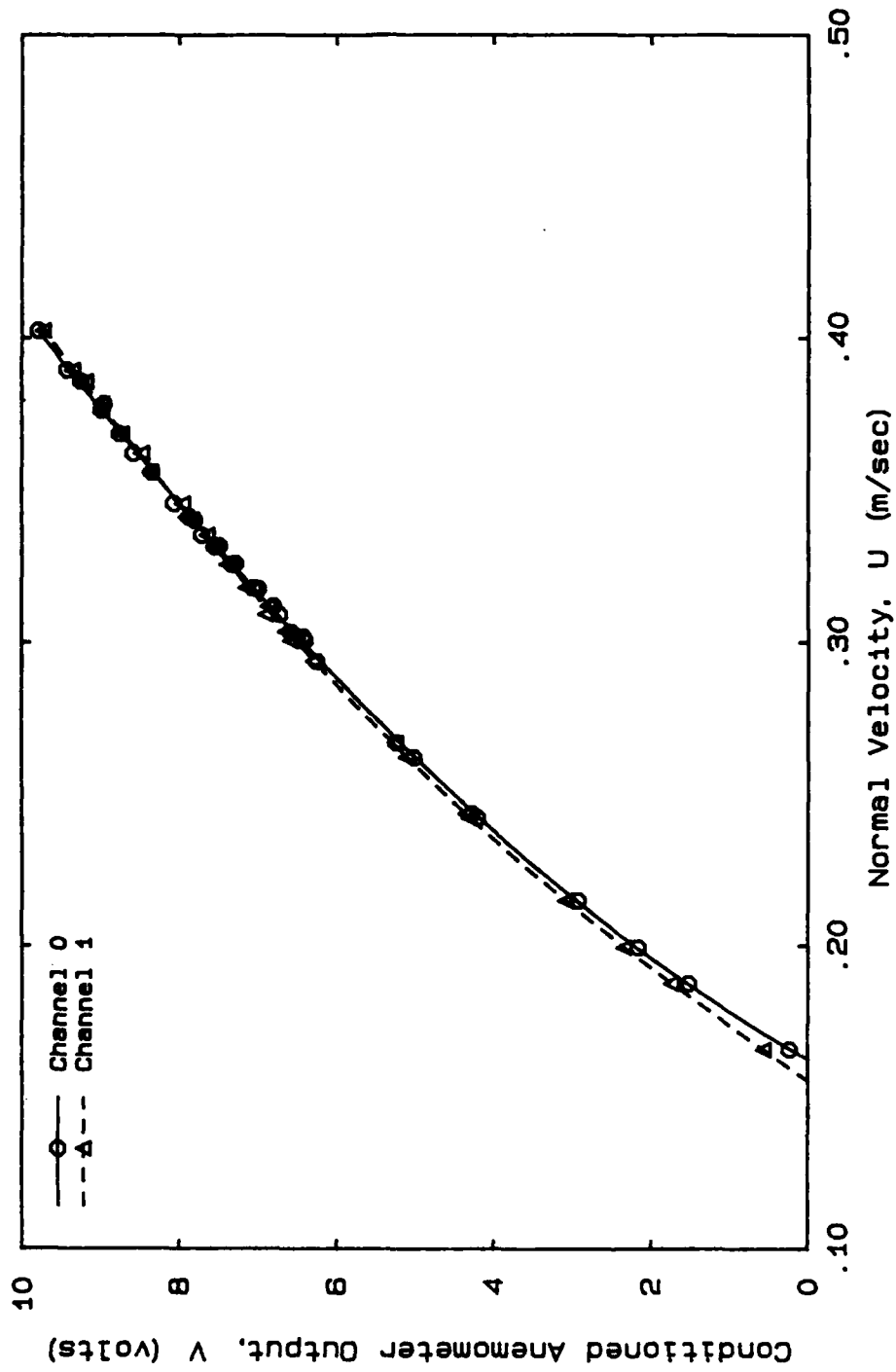
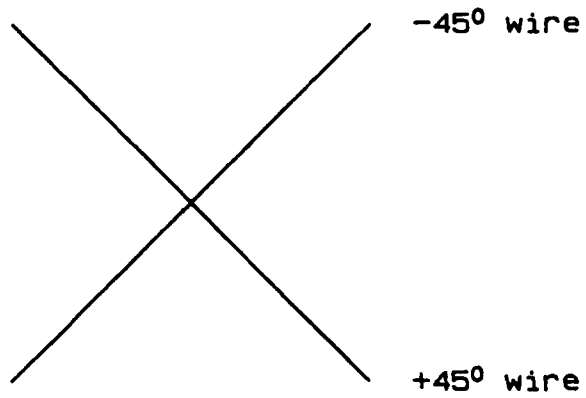


Figure B.1: Cross-wire calibration, polynomial fit to order 4.

Cross-wire:



Velocity Decomposition:

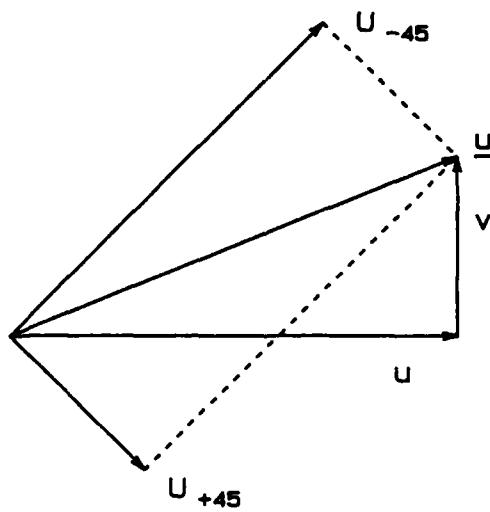


Figure B.2: Cross-wire velocity decomposition.

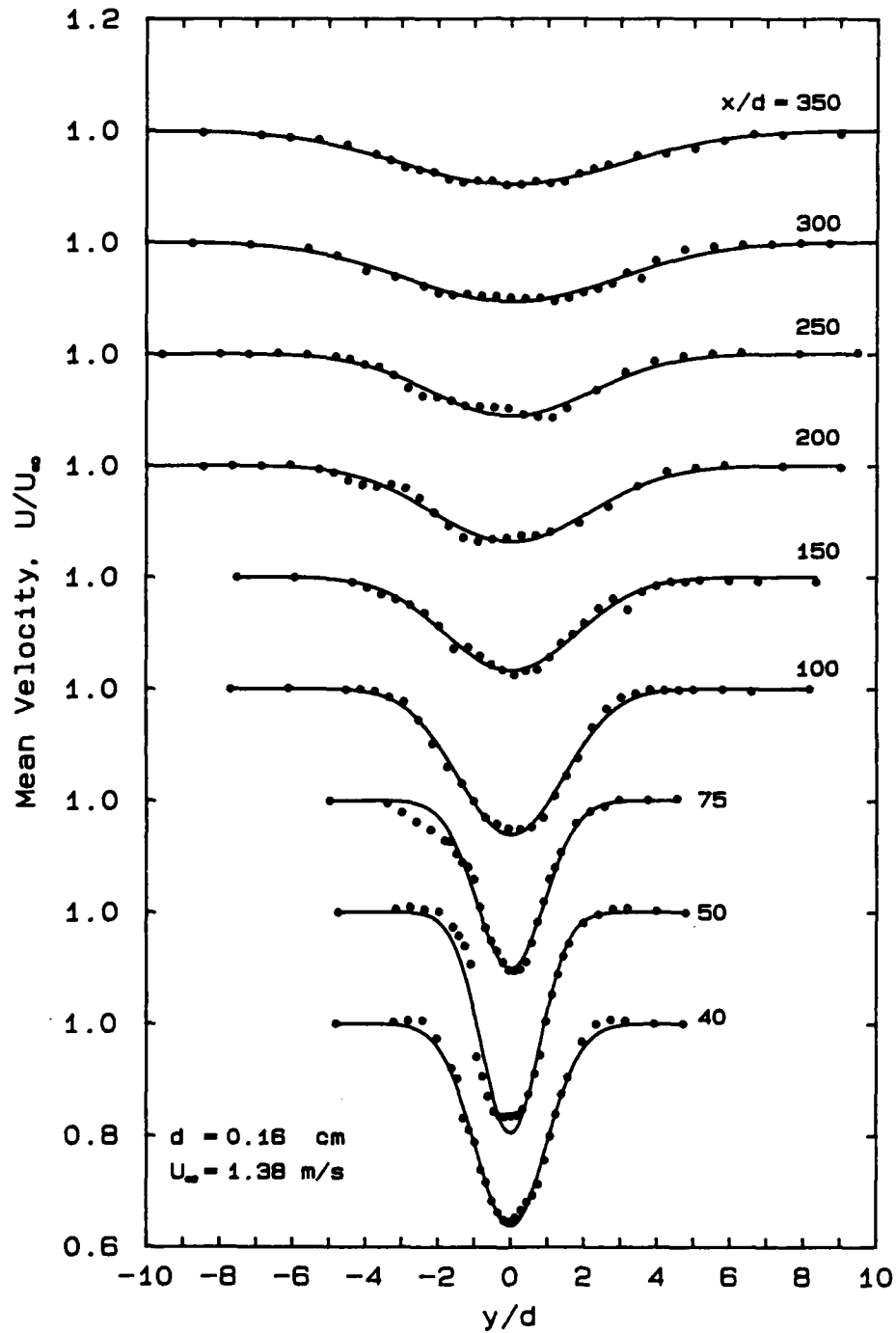


Figure B.3: Mean velocity profiles for circular cylinder wake at  $Re = 140$ .

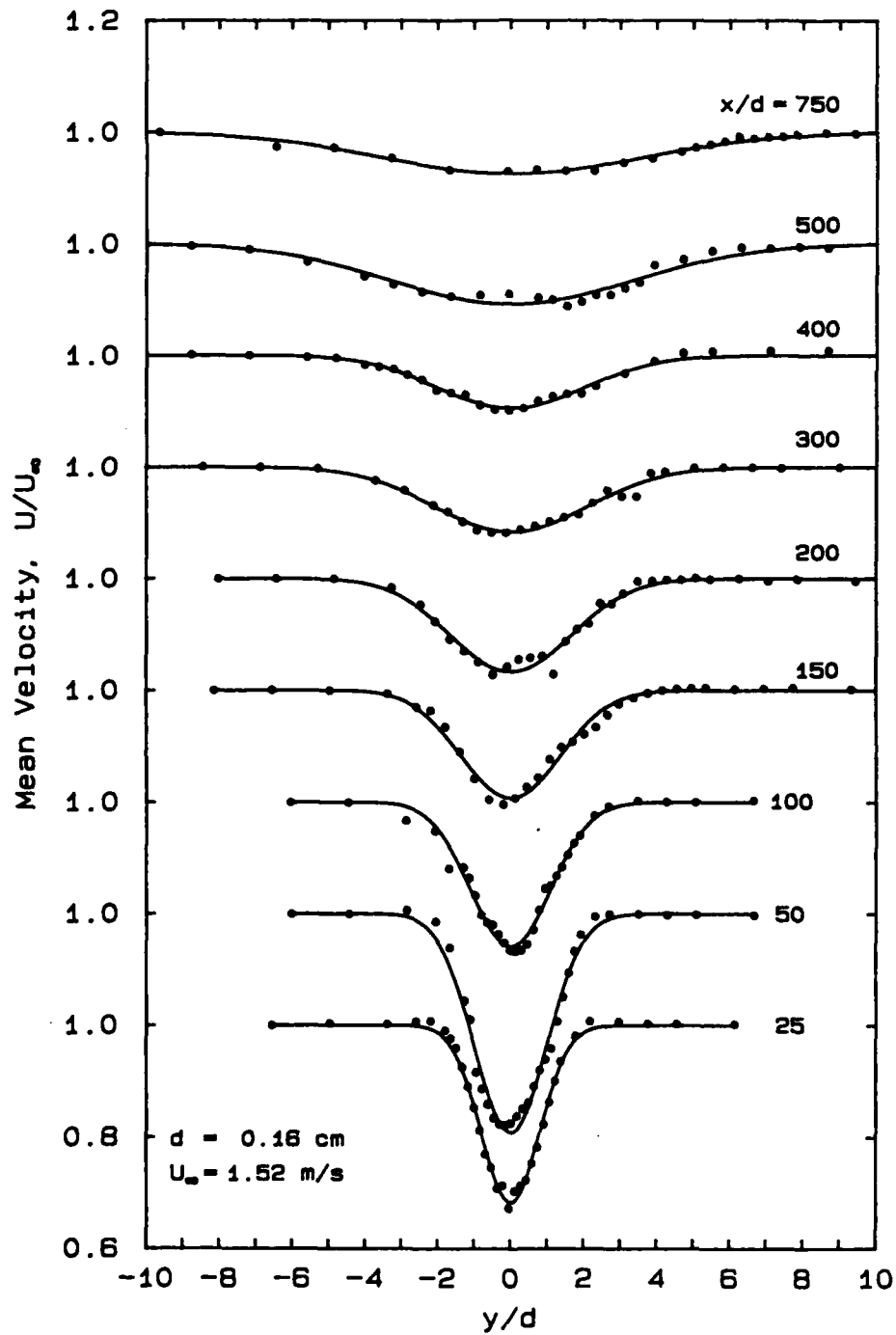


Figure B.4: Mean velocity profiles for circular cylinder wake at  $Re = 150$ .



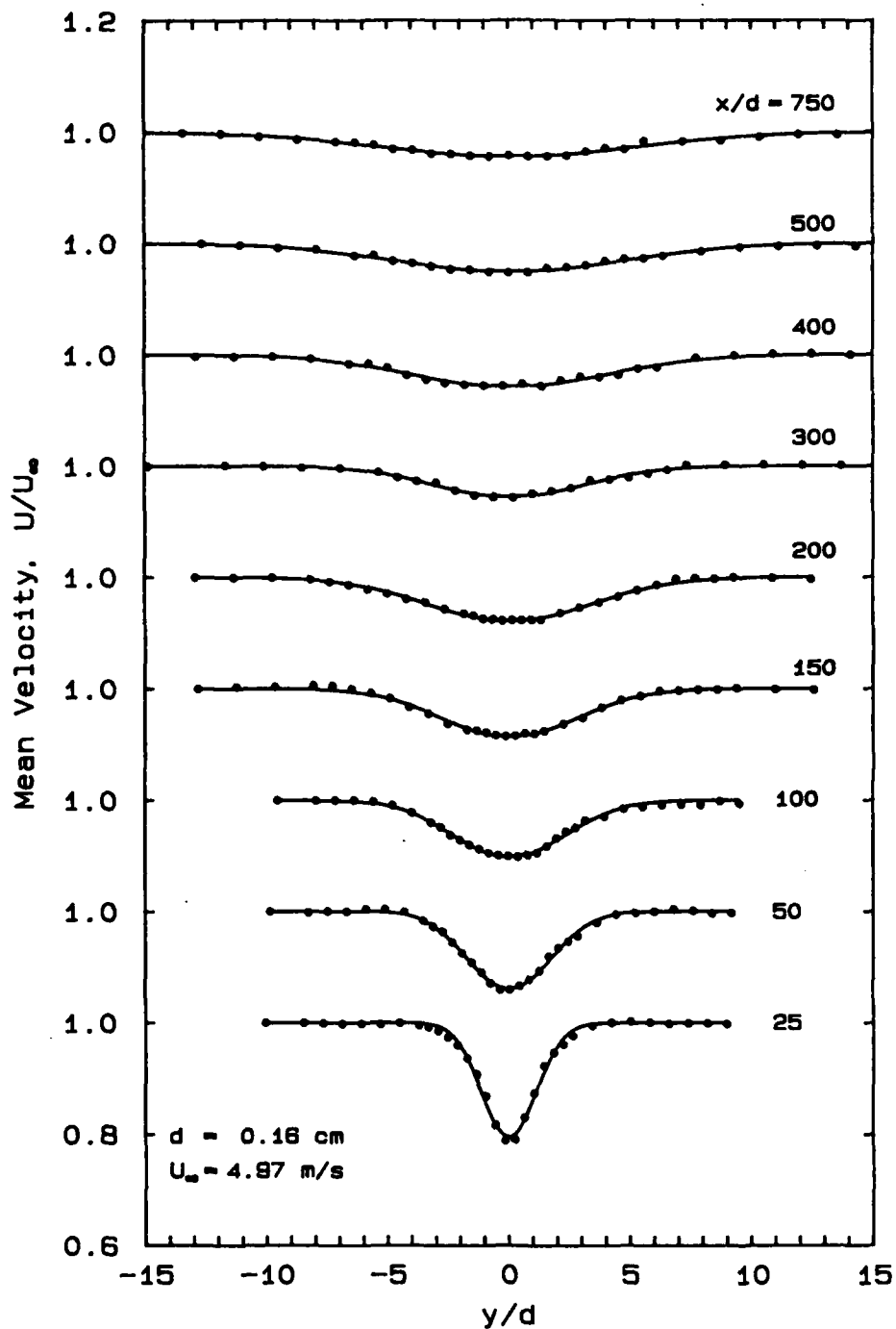


Figure B.5: Mean velocity profiles for circular cylinder wake at  $Re = 500$ .

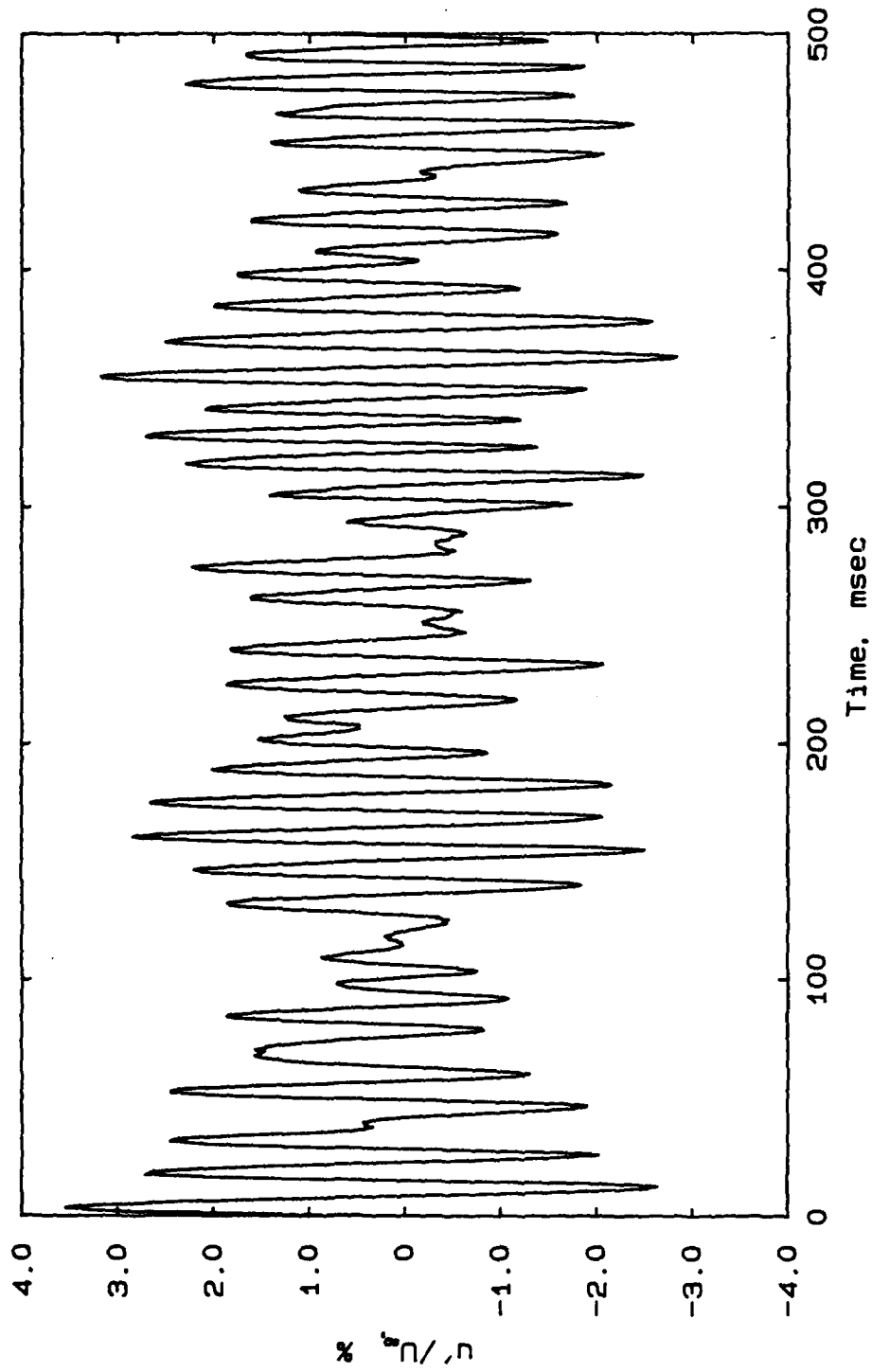


Figure B.6: Time-trace of  $u'/U_\infty$ : circular cylinder wake  
at  $Re = 150$ ,  $x/d = 200$ , and  $y/d = 1.5$ .

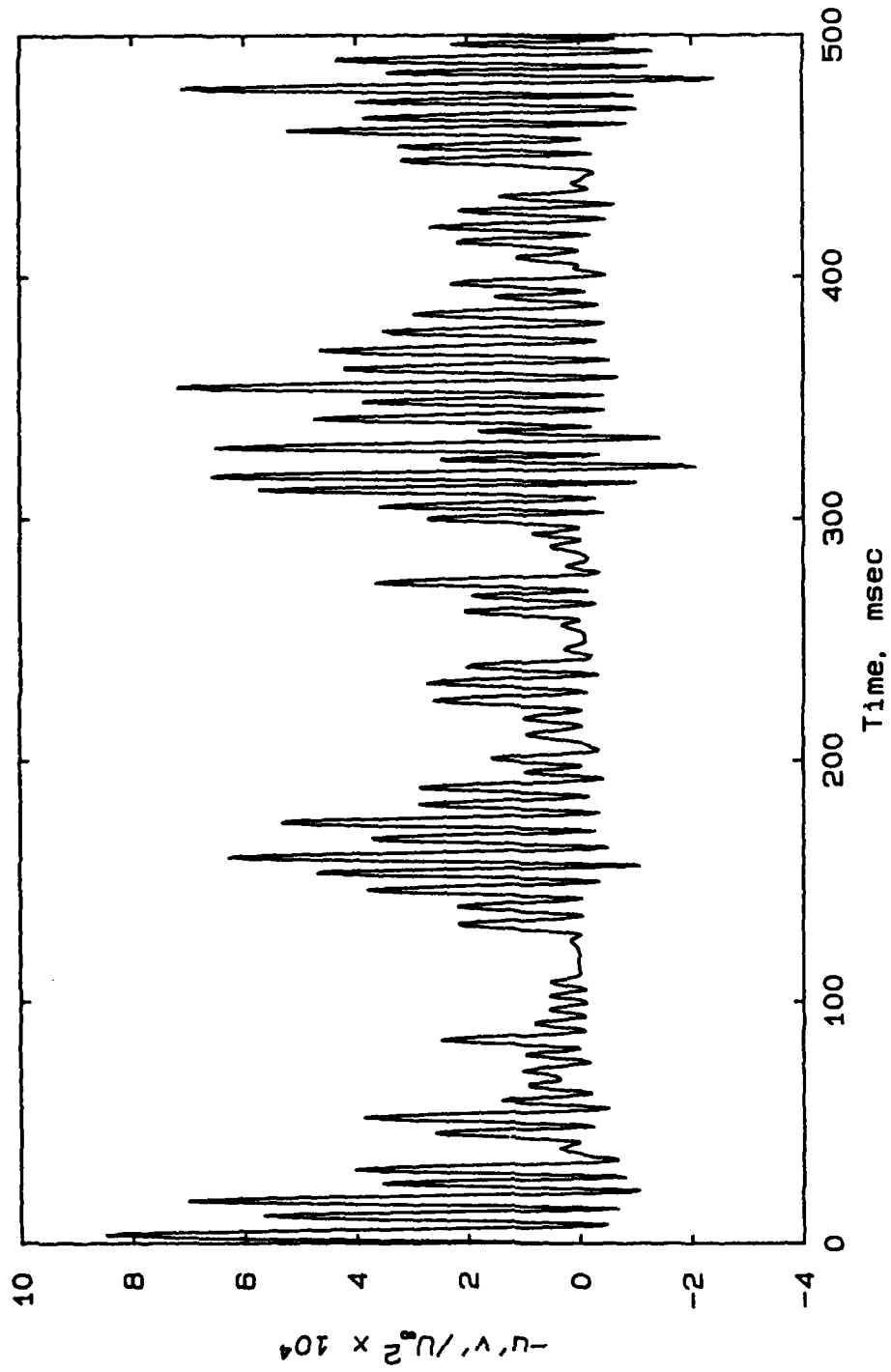


Figure B.7: Time-trace of Reynolds stress,  $-u'v'/U_o^2$ ; circular cylinder wake at  $Re = 150$ ,  $x/d = 200$ , and  $y/d = 1.5$ .

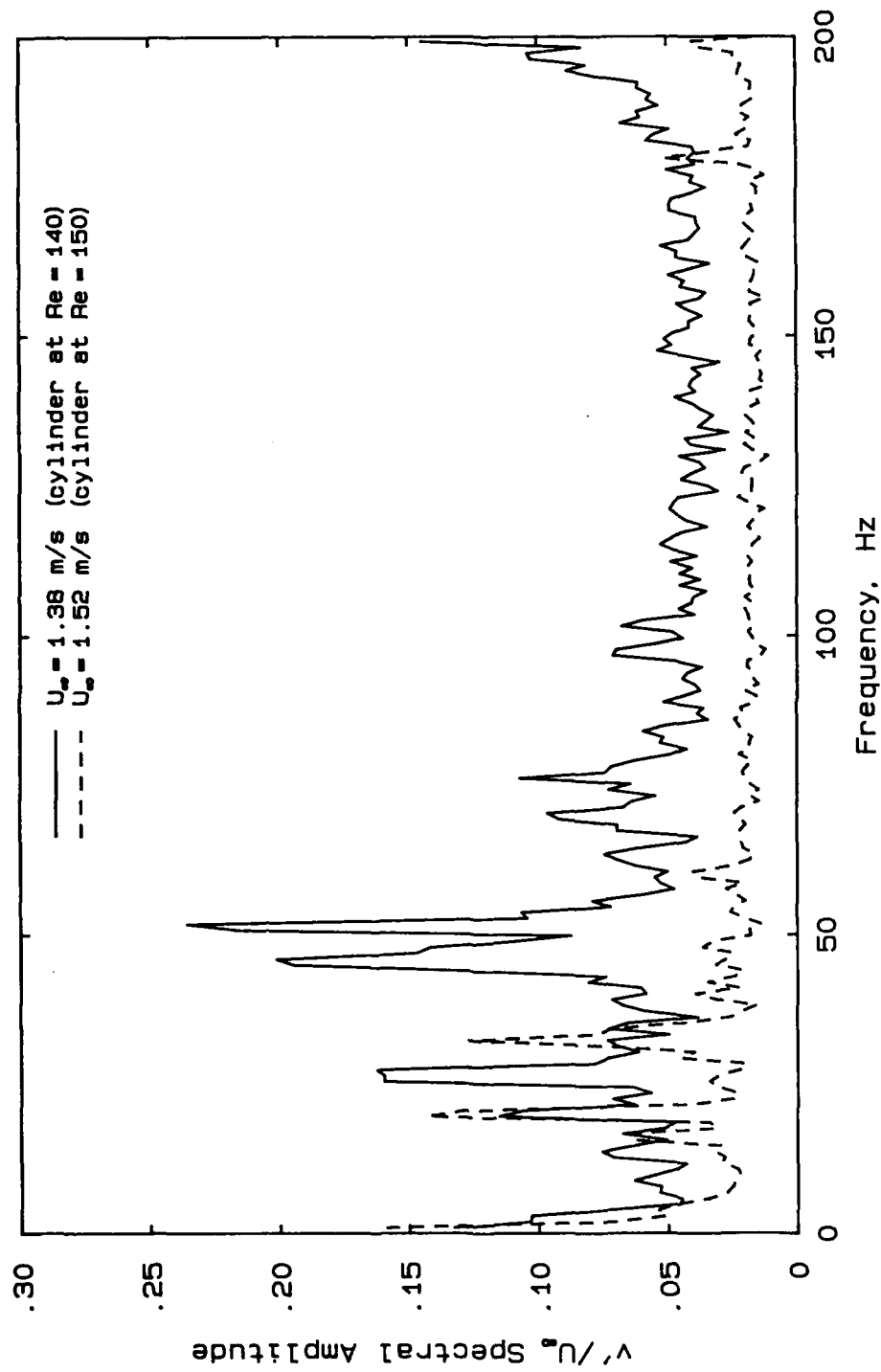


Figure B.8: Freestream spectra at tunnel conditions corresponding to each set of measurements.

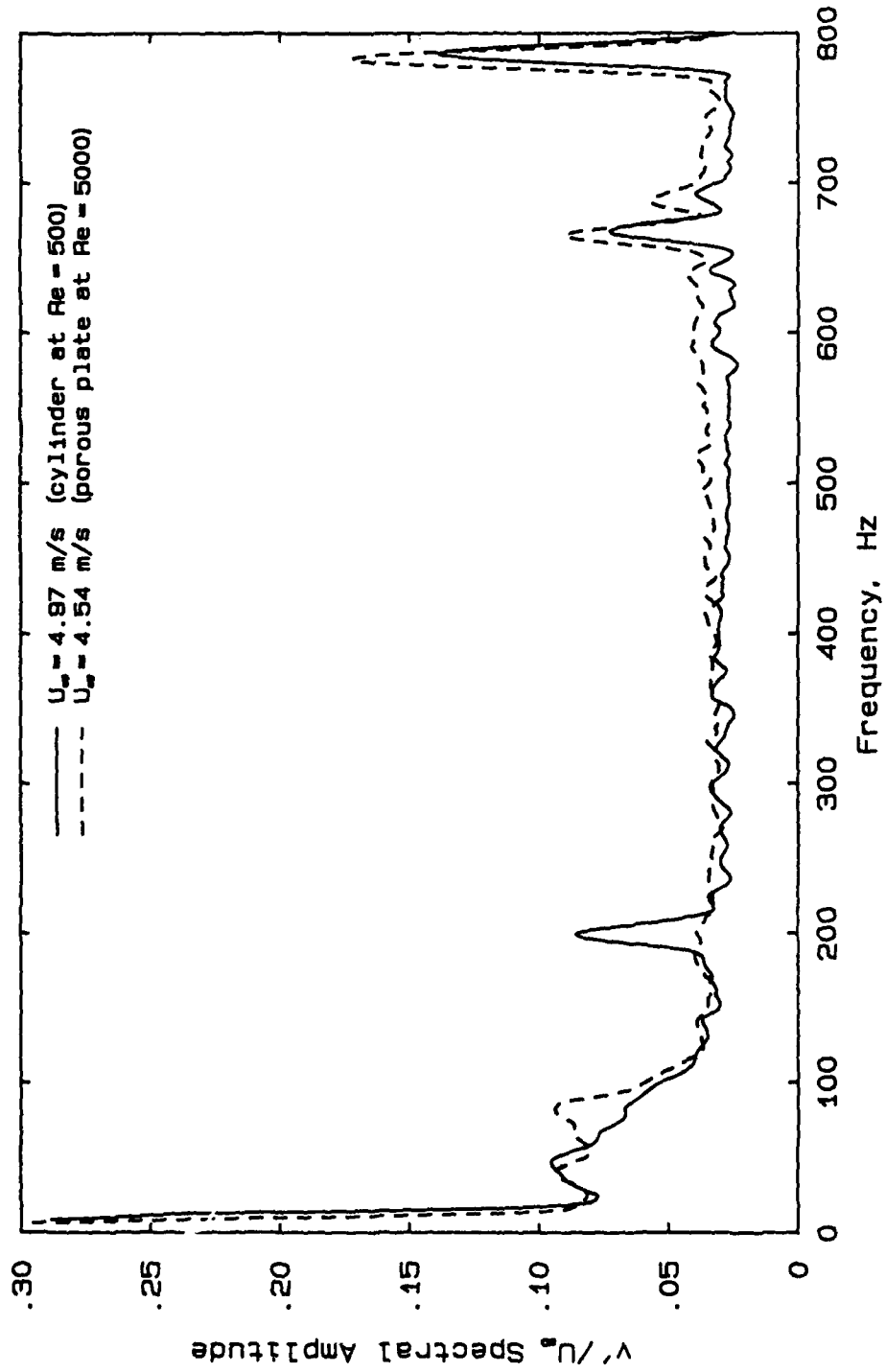


Figure B.9: Freestream spectra at tunnel conditions corresponding to each set of measurements.

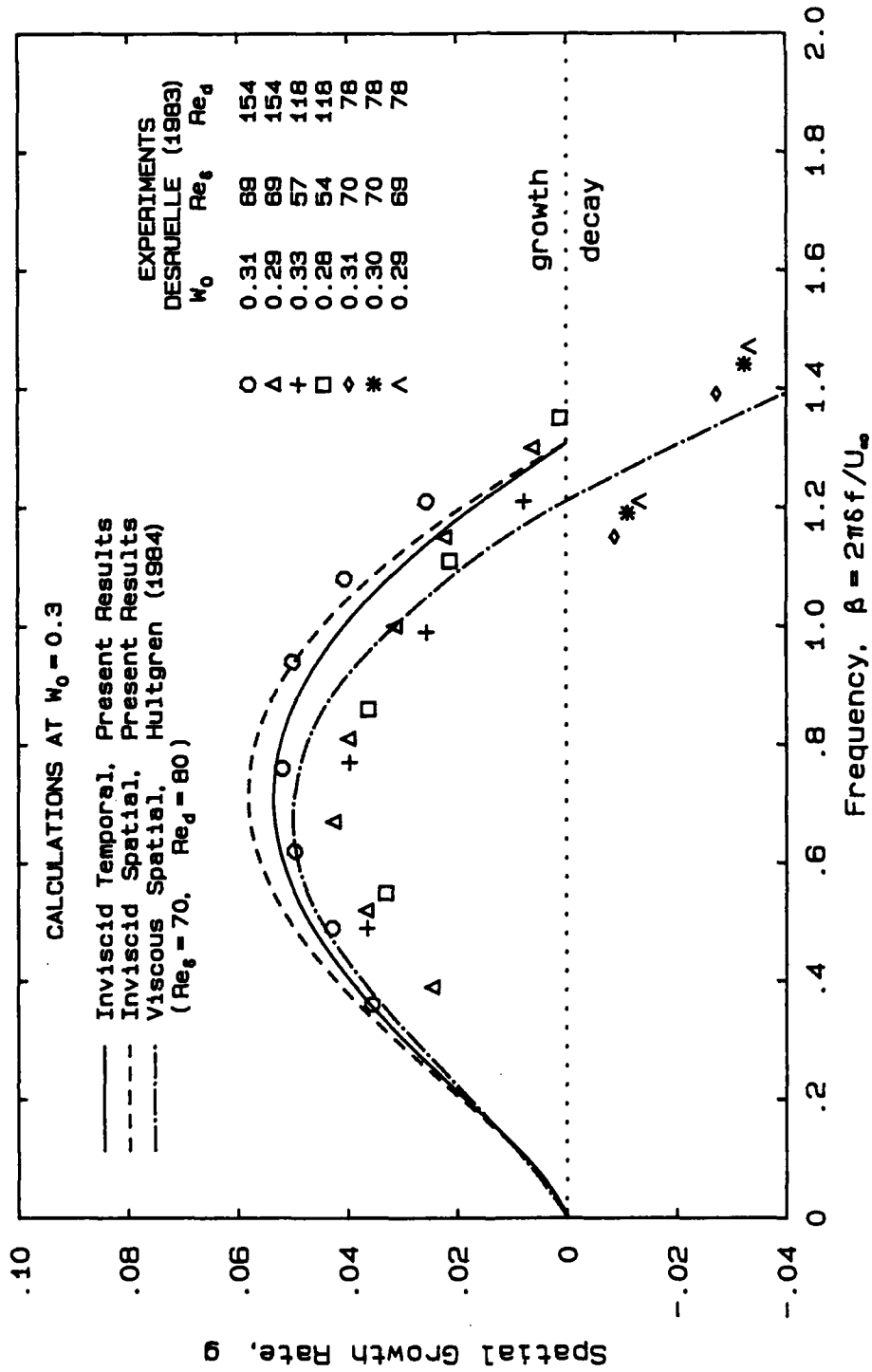


Figure C.1: Comparison of far-wake stability calculations with experiment;  $W_0 \approx 0.3$ .

END

FILMED

9-84

DTIC